AD-A128585

AD A-128 585

TECHNICAL REPORT ARLCB-TR-83008

CRACK GROWTH IN MERCURY EMBRITTLED ALUMINUM ALLOYS UNDER CYCLIC AND STATIC LOADING CONDITIONS

JOSEPH A. KAPP

MARCH 1983

US ARMY ARMAMENT RESEARCH AND DEVELOPMENT COMMAND
LARGE CALIBER WEAPON SYSTEMS LABORATORY
BENÉT WEAPONS LABORATORY
WATERVLIET N.Y. 12189

REPORT DOCUMENTATION PAGE		READ INSTRUCTIONS BEFORE COMPLETING FORM
1. REPORT NUMBER ARLCB-TR-83008	2. GOVT ACCESSION NO.	3. RECIPIENT'S CATALOG NUMBER
4. TITLE (*and Subtitle*) CRACK GROWTH IN MERCURY EMBRITTLED ALUMINUM ALLOYS UNDER CYCLIC AND STATIC LOADING CONDITIONS		5. TYPE OF REPORT & PERIOD COVERED Final 6. PERFORMING ORG. REPORT NUMBER
7. AUTHOR(*s*) Joseph A. Kapp		8. CONTRACT OR GRANT NUMBER(*s*)
9. PERFORMING ORGANIZATION NAME AND ADDRESS US Army Armament Research & Development Command Benet Weapons Laboratory, DRDAR-LCB-TL Watervliet, NY 12189		10. PROGRAM ELEMENT, PROJECT, TASK AREA & WORK UNIT NUMBERS AMCMS No. 61110191A0011 DA Project No. 1L161101A9A PRON No. 1A2231491A1A
11. CONTROLLING OFFICE NAME AND ADDRESS US Army Armament Research & Development Command Large Caliber Weapon Systems Laboratory Dover, NJ 07801		12. REPORT DATE March 1983 13. NUMBER OF PAGES 173
14. MONITORING AGENCY NAME & ADDRESS(*if different from Controlling Office*)		15. SECURITY CLASS. (*of this report*) UNCLASSIFIED 15a. DECLASSIFICATION/DOWNGRADING SCHEDULE

16. DISTRIBUTION STATEMENT (*of this Report*)

Approved for public release; distribution unlimited.

17. DISTRIBUTION STATEMENT (*of the abstract entered in Block 20, if different from Report*)

18. SUPPLEMENTARY NOTES

This was a thesis in partial fulfillment of requirements for degree of Doctor of Philosophy in Materials Engineering at Rensselaer Polytechnic Institute, Troy, New York.

19. KEY WORDS (*Continue on reverse side if necessary and identify by block number*)

Fracture	Liquid Metal Embrittlement
Fatigue	Mercury
Fracture Mechanics	Aluminum
Adsorption	

20. ABSTRACT (*Continue on reverse side if necessary and identify by block number*)

Crack growth rates were measured on three aluminum alloys under cyclic and static loading conditions in laboratory air and in liquid mercury at about +25°C. One alloy, 6061-T651, was tested under both loading conditions at temperatures ranging from -25°C to +45°C. Fracture mechanics techniques were used.

(CONT'D ON REVERSE)

DD FORM 1 JAN 73 **1473** EDITION OF 1 NOV 65 IS OBSOLETE

20. ABSTRACT (CONT'D)

Under cyclic loading conditions, no enhanced crack growth in mercury was measured until a critical stress intensity factor range (ΔK) was exceeded. When ΔK increased above the threshold value, the crack growth rate increased by as much as three orders of magnitude, when compared to the crack growth rate in air. From the appearance of the fracture surface the mechanism of embrittlement was deduced to be reduced cohesion.

Under static loading conditions, crack velocities of centimeters per second were measured in load control. Under displacement control much slower crack velocities were measured in two alloys. The decrease in crack velocity was attributed to crack blunting and large plastic zones. Static crack velocity and cyclic crack growth rate increased with decreasing temperature. This unusual temperature effect was related to the kinetics of adsorption of mercury on aluminum.

TABLE OF CONTENTS

4. RESULTS

LIST OF ILLUSTRATIONS

Page

TABLES

ACKNOWLEDGEMENTS

A work as involved as a Ph.D. cannot be completed without massive assistance to the candidate by many people. I am no exception. First of all I would like to thank my advisor Prof. D. J. Duquette and the members of my doctoral committee, Prof. N. S. Stoloff and Prof. R. H. Doremus all of the Materials Department, Rensselaer Polytechnic Institute and Dr. T. E. Davidson, Chief of Research, Benet Weapons Laboratory, for their guidance, suggestions, and support during the course of this study. Also I wish to acknowledge Dr. M. H. Kamdar of the Materials Engineering Section, Benet Weapons Laboratory for his many suggestions during the course of the work and for the conception of the general topic to be studied.

The assistance of the following members of the Materials Engineering Section, Benet Weapons Laboratory is greatly appreciated: Messrs. D. P. Kendall and J. H. Underwood for their suggestions on fracture mechanics methods, Mrs. T. Brassard for her many suggestions on metallography techniques, Mr. C. Rickard for his assistance in metallography specimen preparation, and photographic reproduction, Mr. W. Legasse for chemical analysis of the aluminum alloys, Mr. H. Alford for conducting the tensile tests, Messrs. M. Fleszar, S. Sopok, and F. Moscinski for preparation of etching solutions and plating solutions, Mr. C. Nolan for plating the specimens, Mr. J. Trant for hydraulic testing machine maintenance, Mr. L. McNamara for his assistance in fractography, Messrs. R. Abbott, W. Yaiser, and especially J. Zalinka for their assistance in conducting the experiments and data acquisition.

I would also like to thank Mr. H. Weglarz and members of the Machine Processes Activity, Benet Weapons Laboratory, for their assistance in the manufacture of the fracture mechanics specimens used in this study.

Also I wish to thank Ellen Fogarty for her diligent preparation of the manuscript, and Mr. I. Goldsberry and Ms. Suellen Diamond for their assistance in preparing the graphical arts. Also, the assistance of Ms. R. Neifeld and Mr. R. Sullivan in the editing and assembly of the report is greatly appreciated.

1. INTRODUCTION

When certain solid metals are placed in an environment of certain liquid metals and loaded in tension, fracture occurs at stress levels substantially below the true fracture stress of the solid metal in an inert environment. In addition to the lower fracture stress, the embrittled solid metal exhibits much less elongation, less reduction in area, and a change in fracture mode. This phenomenon is called liquid metal embrittlement (LME).

Because of the relatively rare occurrence of solid metal/molten metal contact in industry, LME has not been the subject of a great deal of engineering investigation. However, as a scientific question, LME has generated substantial interest. This is shown in the small sampling of literature cited herein.[1-18,23-35] Most of the research performed in LME has dealt with three major areas of study: determining the micromechanism of embrittlement, assessing the degree of embrittlement using various solid metal/liquid metal couples, or classifying those couples which result in LME to give some method of predicting susceptibility.

One testing method which has not been used in a thorough study of LME is fracture mechanics. Fracture mechanics has been used successfully to characterize the fatigue and fracture properties of materials in both inert and aggressive environments.[19,36,38-53,62,64-66] Important contributions of fracture mechanics have been both practical, by determining tolerance to pre-existing cracks, and basic, by gaining insight into rate controlling processes in the sub-critical crack growth range.

References are listed at the end of this report.

In this report, fracture mechanics was used to characterize the behavior of a classic LME couple: aluminum-mercury. The experimental variables studied were alloy, temperature, and loading condition. Three alloys were studied: a low-strength, high-toughness commercially pure alloy; a medium-strength, medium-toughness alloy; and a high-strength, low-toughness alloy. For each alloy at ambient temperatures, three loading conditions were tested, two static conditions and cyclic loading. The two static loadings were conducted under constant load conditions or constant displacement conditions. The cyclic fatigue data was generated under alternating load control at two testing frequencies. Finally, the medium-strength alloy was tested under both static loading conditions at various temperatures, and under cyclic conditions at several temperatures.

The report is organized in the following manner. Presented in Section 2 is a brief two-part literature review. The first part deals with a review of the LME literature; the second part presents a brief outline of fracture mechanics, with the emphasis on fracture mechanics applied to environmentally accelerated fracture. Section 3 is an explanation of the experimental means by which the testing was performed. The apparatus used in the different experiments are described. Special techniques necessary to conduct the tests are explained, and reference is made to Appendix A where the fracture mechanics specimens used are developed and characterized. The manner in which the data was obtained and analyzed is also outlined in this section.

In Section 4, Results, the analyzed data is presented. This is accomplished in two subsections. First, the results for all the alloys at ambient temperature are presented, followed by the results obtained at various temperatures for the medium-strength alloy. Photomicrographs from fractographic examinations are also included in this section.

The Discussion, Section 5, presents an explanation of the observed results. Comparisons are made with previous work to show similarities which have occurred. An attempt is made to correlate the static results with the cyclic loading results. Also presented are arguments to defend the unique quality of the obtained results. Appendix B is referenced to argue that the unusual temperature effect was due to surface adsorption. Finally, some comments are made regarding the micromechanism by which the embrittled crack growth occurs.

Sections 6 and 7 contain conclusions drawn from the research. Included also are some recommendations for future work, both theoretical and experimental. Among these recommendations is a call for future work on the relationship between surface adsorption and fracture phenomena.

2. HISTORICAL REVIEW

2.1 Liquid Metal Embrittlement

Liquid metal embrittlement (LME) occurs when certain normally ductile solid metals are subjected to stress while in intimate contact with certain liquid metals. If embrittlement occurs, the true fracture stress in the liquid metal environment is substantially less than the true fracture stress of the solid metal fractured in an inert environment. Fracture in the liquid metal environment results in much less reduction in area (% RA) and much less elongation (% El). LME has been known to occur for at least 65 years and has been the subject of substantial investigation in the past few decades. This is evidenced by the four review papers,[1-4] a book,[5] and a conference volume[6] on the subject. All these publications give a thorough review of the state of the art at the time of their publication.

It has generally been accepted that two prerequisites must be met before LME occurs: first, the liquid metal must wet the solid metal surface, and second, tensile stresses must be present.[5] Some modification to these basic requirements has been suggested. Kamdar[4] has argued that the tensile stresses must be high enough to cause microscopic plastic flow, since crack initiation is dependent upon plastic deformation, which is unaffected by the liquid metal. This argument has been countered, primarily by Lynch[7-10] who claims, based exclusively on fractographic evidence, that the liquid metal essentially reduces the yield strength on a microscopic scale, thus enhancing crack initiation. No measurement of reduced yield strength has been published to confirm this. Although, recent experiments by Kapp and Kamdar[11] on notched, slow bend samples of a sintered 97%W-2%Ni-1%Fe alloy wetted with liquid mercury indicate that yielding and plastic flow occurs at an applied load of only 60 percent of the load necessary to cause yielding in an unwetted sample. However, these results are very preliminary at this writing. The tensile stress requirement has also been challenged recently by Ashok et al[12] in their work on LME of amorphous metals. In that study, specimens were tested in slow bending. The compression side of the samples was wetted with a liquid metal and embrittlement occurred. Regardless of these recent developments, applied tensile stress is still generally considered a prerequisite for embrittlement.

The requirement of the liquid species wetting the surface of the solid metal has been the subject of some recent work. In the paper by Mostovoy and Breyer,[13] embrittlement of internally leaded high-strength steels occurred well below the melting temperature of the lead. This study has resulted in the appearance of several papers dealing with embrittlement by a solid metal[13-18] rather than a liquid metal. Both forms of embrittlement (solid metal and liquid metal) have been redefined as subtopics in the general area of "Metal Induced Embrittlement" or MIE.[1,3] The subtopics have been called solid metal induced embrittlement (SMIE) and liquid metal induced embrittlement (LMIE). For brevity, since this report deals only with liquid metal embrittlement, the more classic term, LME, will be used. Thus, it is apparent that the embrittling species need not be in the liquid state for embrittlement to occur. Therefore, the second prerequisite for embrittlement, intimate contact between the liquid metal and the solid metal, is not an absolute requirement.

The requirements for LME are relatively simple. If one is to assume that the total phenomenon is as easily understood as the requirements, very little study would be necessary. This is not the case. There is a substantial LME literature, which can be classified into three major areas: metallurgical and other experimental variables, susceptibility to embrittlement, and the micromechanism of embrittlement. Each of these areas is discussed briefly below.

2.1.1 Metallurgical and Experimental Effects

The fracture event, defined as the total separation of a single solid metal into two or more pieces by mechanical means, is preceded by a three-stage process: crack initiation, crack growth of small cracks to a critical size, and unstable crack growth.[19] Each of these stages can occur in either a ductile or brittle fashion. Ductile fracture is accompanied by a great deal of plastic deformation resulting in a fracture surface which, when examined in the electron microscope, is very rough, often containing ridges and dimples.[19] Examining polished and etched cross sections of such specimens reveals dislocation etch pits, slip lines and bands, or twins. Metals which fracture in a brittle manner show evidence of little or no plastic deformation. In the electron microscope, the fracture surface is predominantly flat. The only salient features are shallow ridges, forming "river patterns" if the fracture is transgranular, or the smooth outlines of the grains if the fracture is intergranular. Transverse sections examined using light microscopy show little indication of microscopic plastic deformation and usually reveal only the crack path.

The metallurgical variables which affect the type of fracture process which occurs can be treated in the following manner. Petch[20] has shown that the yield strength, σ_y, of many materials follows the relationship

$$\sigma_y = \sigma_i + k_y d^{-1/2} \qquad (2.1)$$

where σ_i and k_y are material constants, and d is the average grain diameter. Using dislocation theory, Cortrell,[21] has derived an equation for the fracture strength, σ_f as:

$$\sigma_f = \frac{4G'\gamma}{k_y} d^{-1/2} \qquad (2.2)$$

where G' is the shear modulus and γ is the surface energy. For ductile fracture, σ_y must be less than σ_f. Conversely, if σ_f is less than or equal to σ_y, brittle behavior predominates.

By comparing Eqs. (2.1) and (2.2), one observes that ductile behavior is favored by materials with low yield strength. Thus low values of σ_i (resistance to dislocation motion), small k_y values (which are related to slip propagation across grain boundaries), and small grain sizes d all reduce σ_y or increase σ_f. Brittle behavior is preferred in materials with high yield strength, high σ_i and k_y values, large grain sizes, low shear moduli, and low surface energies.

It has been generally accepted that the liquid metal environment lowers the surface energy of the solid metal.[6,7] This decreases the fracture stress and promotes brittle behavior. Recently Lynch[7-10] and Ashok et al[12] have argued that the shear modulus is also reduced by a liquid metal environment. Whichever occurs, the result nonetheless is embrittlement of the solid metal.

Some materials which are embrittled by liquid metals, primarily BCC and HCP materials, have temperature-sensitive resistance to microscopic plastic deformation (σ_i in Eq. (2.1)). Over relatively small temperature ranges, σ_i increases with decreasing temperatures. Often the temperature ranges necessary to change σ_i occur where the surface energy, γ, and shear modulus, G', are essentially constant. This allows for a temperature transition from ductile to brittle behavior to occur. When such materials are tested in embrittling liquid metals, the ductile-brittle transition temperature is altered.[1,2] Therefore, temperature is an important variable in LME even in materials that do not exhibit the temperature transition described above (FCC materials principally).

It has been shown that the degree of embrittlement is greatest at temperatures very close to the melting point of the liquid metal.[1-5] Testing at successively higher temperatures results in less brittle behavior until at a sufficiently high temperature the liquid metal has no embrittling effect.

Another important variable in changing the property σ_i in Eq. (2.1) is strain rate; σ_i increases with increasing strain rate. This is explained by the fact that it takes time for microscopic plasticity to occur and accommodate loads with plastic flow. In recent experiments with an aluminum alloy wetted with mercury, the strain rate variable was addressed.[22] Testing was performed at strain rates ranging from $5 \times 10^{-5} \mathrm{sec}^{-1}$ to $0.5 \mathrm{sec}^{-1}$, at temperatures from -50°F to 600°F. In all cases, embrittlement commenced at the melting point of mercury (~ -40°F), but recovery occurred at different temperatures. At low strain rates recovery occurs at a lower temperature than at high strain rates. The same behavior has also been reported for several other LME couples.[1]

The strain rate dependence suggests that liquid metals may affect σ_i in Eq. (2.1). This conclusion is drawn primarily from discounting the normally presented explanation for temperature recovery: desorption of the liquid species from the fracture process zone at the crack tip.[5] Desorption predicts no strain rate effect on recovery, only a temperature effect.

Static fatigue tests have also been conducted to study the effects of liquid metals.[23,24] These tests are performed when specimens are wetted with the liquid metal and loaded to a stress which is less than the stress necessary to cause fracture under monotonic loading. The load is held constant until fracture occurs. A plot of applied stress versus time to fracture is generated. Such delayed fracture behavior has been observed in systems such as aluminum-copper,[23] and copper-beryllium[24] alloys in mercury environments. Also, Iwata et al[25] have shown that some steels plated with solid cadmium exhibit static fatigue failure.

The exact cause of the static fatigue behavior is not yet fully understood. It has been suggested in all the studies referenced above that diffusion of the embrittling species, especially along grain boundaries, causes delayed fracture. This argument is given further credence by the unpublished work of Lynn and Warke reported by Stoloff.[3] In that study, static fatigue of 4140 steel plated with zinc, cadmium, lead, and tin was measured at various temperatures. Activation energies were calculated from time to fracture experiments and also by crack length measurements on the fracture surface, assuming embrittling atoms travel by random walk diffusion. Both of these analyses result in nearly the same activation energy computation implying that diffusion is the event which limits the rate of embrittlement.

Another important experimental variable which has been studied in LME is cyclic loading, although it has received less attention than monotonic loading. These studies showed that significant changes in fatigue properties occurred when testing was performed in liquid metal environments. In some cases, embrittlement occurred only at high stress levels, leaving the endurance limit unchanged, such as in the cases of mercury coated copper and lead coated brass.[26] In other instances, embrittlement occurred at all stress levels with a significant decrease in endurance limit. Examples of the latter are 4340 steel coated with mercury and 7075-T6 aluminum coated with either mercury or gallium.[5]

Regan and Stoloff[27] have argued that the observed S-N effects in liquid metals can be attributed to accelerated crack growth, with no effect on crack initiation. By observing that cyclically loaded, annealed copper-aluminum samples wetted with mercury can support very nearly the ultimate tensile strength in mercury, the following has been deduced. The plastic strain which accumulates from cyclic loading is large enough to cause a stress concentration, that raises the stress locally to the maximum stress occurring under monotonic loading. This results in crack initiation, followed by very rapid crack growth from the liquid metal, causing lower fatigue lives.

The same argument does not apply to cold rolled copper alloys. Under monotonic loading, these alloys show no embrittlement because of compressive residual stress at the surface from the rolling. Under cyclic loading in mercury, embrittlement occurs. In this case, it has been argued that the strengthening that occurs from cold rolling suppresses crack nucleation at the surface under monotonic loading. Under cyclic loading, multiple slip causes intrusion-extrusion topography which leads to surface crack initiation and embrittlement. In either of the two cases mentioned above, the crack growth portion of the fracture process is more strongly affected by the liquid metal than the crack initiation portion.

2.1.2 Susceptibility to Embrittlement

Many approaches have been taken to determine the susceptibility to LME. The first was suggested by Chaevskii[28] relating the enthalpy of mixing (ΔH_m) of elemental solid metal/liquid metal interaction. The second, developed by Kamdar[4] correlates electronegativity with embrittlement. Third, Kelley and Stoloff[29] have developed a model which relates the degree of embrittlement to the solid-liquid bond energy. Recently, Old[30] developed an experimental method in which the degree of embrittlement is related to the solid-liquid surface energy γ_{SL}, and the solid-vapor surface energy γ_{SV}, measured in wetting studies.

In the first model,[28] it was suggested that embrittlement should be related to the enthalpy of mixing (ΔH_m) for the solid-liquid couple considered. A high positive ΔH_m would indicate that the couple should not be expected to bond. If an interface was formed in such couples, the energy of the interface would be high and no embrittlement would be expected. A high negative ΔH_m would indicate bonding, forming intermetallic compounds. In this case, again no embrittlement would be predicted. Only where ΔH_m is small and positive is embrittlement expected. Some success has been claimed using this technique to predict the occurrence of embrittlement. However, often the degree of embrittlement is not predicted accurately.

Kamdar's model[4] shows that there is a relationship between Pauling's electronegativity and the degree of embrittlement. The empirical relationship is best demonstrated with an example. Cadmium is embrittled by indium or gallium, but not by thallium or mercury; furthermore, indium is more aggressive than gallium. Pauling's electronegativitiy of cadmium is 1.7, for indium it is 1.7, for gallium 1.6, and for thallium and mercury 1.8 and 1.9 respectively. Maximum embrittlement occurs when the electronegativity of the solid and liquid species is equal. The greater the difference in electronegativity, the less the embrittlement.

This method also has limited application. In the case of aluminum (electronegativity = 1.5), for example, embrittlement occurs from liquid mercury (electronegativity = 1.9), but not from thallium (electronegativity = 1.8). Also, the small numerical differences in electronegativities make the method relatively insensitive. Nonetheless, this discovery has led Kamdar to develop his "inert carrier"[4] concept which is a valuable experimental tool. With small additions of severely embrittling liquid metals to less aggressive or even non-embrittling (inert) liquid metals, embrittlement can be studied.

The method developed by Kelley and Stoloff[29] is a powerful theoretical technique based on a loss of bond strength due to the presence of the liquid metal. Using this model, the variables of temperature, strain rate, grain size and mutual solubilities can be considered.

The technique goes as follows. First, a solubility parameter, δ, for each element considered is calculated using the equation

$$\delta = \left(\frac{\Delta E_1}{V_1}\right)^{1/2} \qquad (2.3)$$

where ΔE_1 is the sublimation energy and V_1 is the molar volume. Solubility of the liquid in the solid would result in liquid atoms entering the lattice of the solid. This would not affect the surface energy at the crack tip. Solubility of the solid in the liquid could result in dissolution of the solid metal crack tip causing blunting of the crack. Using Eq. (2.3) the mutual solubility of two elements is estimated as the difference in the δ values. Furthermore, the percent difference in δ values is calculated to facilitate comparison.

Second, the bond interaction energy (IE) is calculated. This is accomplished by finding the energy of the sp bond (ΔE_{bond}) of the solid metal and liquid metal involved. Then the energy required (ΔE_{req}) to raise the electrons in the ground state to the bonded state is determined. The interaction energy (IE) is given as

$$IE = \Delta E_{bond} - \Delta E_{req} \qquad (2.4)$$

The value of IE is then compared with the atomization energy of the solid metal, giving an estimate of the percent reduction in free surface energy. Great care is taken in using Eq. (2.4) to get the proper number of moles of liquid and solid metal which interact. Also, the proper number of sp bonds enters into the calculation.

Once the above calculations are made, a plot is generated which compares the relative change in δ values (Eq. (2.3)), with the change in free surface energy. If the algebraic sum of the two percentage changes calculated above exceeds 100, embrittlement is predicted. Conversely, if the sum is less than 100, embrittlement is not predicted. The method is very successful with few exceptions.

The method advocated by Old[30] is an experimental technique. In a moderate vacuum, a drop of molten metal is placed on a clean solid metal surface. The angle that the liquid metal bead forms with the solid metal, the surface energy of the solid-liquid interface (γ_{SL}), and the solid-vapor interface (γ_{SV}) are measured. Comparing the ratios of γ_{SV}/γ_{SL} for several couples, an interesting correlation develops. For known embrittlement couples, the ratio has a value of less than 0.5. For couples that do not embrittle, a ratio value greater than 0.5 is measured. Unfortunately, for some systems the ratio is very close to 0.5. In the case of solid zinc, the ratios measured are 0.48 for lead and 0.50 for cadmium. Lead does embrittle zinc and cadmium does not. It is difficult to argue that the technique is sufficiently accurate to predict embrittlement based on such small differences. Furthermore, there is little justification for the critical value of 0.5.

To summarize the various models of susceptibility, one finds that predicting embrittlement is very difficult. All the models predict susceptibility to some extent, but none of them will predict all the known embrittlement couples, nor will they determine the proper degree of embrittlement. Also, they all eventually rely on some empirical criterion for the embrittlement prediction. This is a tribute to the complexity of the phenomenon.

2.1.3 Mechanisms of Embrittlement

LME is a multi-step process. First, there must be surface interaction between the liquid metal and solid metal, then the embrittling liquid must be transported to the fracture process zone (crack tip). Finally, an interaction of the solid and liquid must occur at the crack tip, causing crack growth at lower stress levels than in inert environments. This scenario presupposes that embrittlement only occurs during the crack growth portion of the total fracture event, as shown in the previous sections.

Although embrittlement must occur by the three-step process described, few authors have stated it, except by implication. Most of the models discussed in the literature have dealt with the final step, the micromechanism of solid metal/liquid metal interaction at the crack tip.[7-10,12,31-34] Recently,[33] some thought has also been given to the transport of the liquid metal to the crack.

No single work has been presented describing how the liquid-solid interaction on virgin solid metal occurs; although it has generally been presumed to occur by adsorption, and is recognized as a prerequisite for embrittlement.

Three attempts have been made to explain the transport of the liquid metal. Westwood and Kamdar[32] have concluded that the transport occurs by surface diffusion of the liquid metal over the newly created fracture surfaces. This conclusion is based on crack growth experiments performed on single crystals of zinc wetted with mercury. An activation energy of about 2 kcal/Mole was observed. Such a value of activation energy is of the correct order of magnitude for surface diffusion.

The other two studies[5,33] have dealt with the same transport mechanism, fluid flow. Rostoker et al[5] present a simple fluid mechanics calculation showing that the liquid metal can approach the crack tip no closer than where the crack is open 10^{-3} cm. To force the liquid to fill the crack completely, pressures on the order of 10^5 atmospheres would be necessary. Thus, it follows that the transport of the liquid metal to the crack tip must be a two-step process. Fluid flows to the vicinity of the crack, followed by surface diffusion. Gordon's work[35] was similar in approach, since it involved first a simple fluid mechanics calculation. Although it seems impossible for a liquid metal to totally fill a crack, it was shown that the liquid could approach the crack much closer than in the previous analysis. The closer proximity to the crack tip combined with the high surface tension in the meniscus led Gordon to conclude that final transport to the crack tip could be accomplished by either of two mechanisms: surface diffusion or vapor transport. The latter case was limited to molten metals with relatively high vapor pressures such as mercury.

It was suggested that crack growth rate measurements be made to determine by which mechanism this final transport indeed occurs. Since surface diffusion would have an activation energy of about 2 kcal/Mole while vapor transport would have an activation of about 20 kcal/Mole, the detection would be clear.

The actual micromechanism of embrittlement at the crack tip has received most attention in the literature. The first mechanism proposed was reduced cohesion.[31,32] Developed independently and simultaneously by Stoloff and Johnston[31] and Westwood and Kamdar,[32] the model states that adsorption of a liquid metal atom at the crack tip effectively reduces the cohesive strength of the crack tip bond, resulting in crack growth at lower stresses. Robertson[33] proposed that very rapid dissolution of the solid metal into the liquid metal at the crack tip causes the subcritical crack growth. A grain boundary penetration model was proposed by Krishtal.[34] This model assumes that embrittlement occurs in a two-step process. Diffusion of liquid metal along grain boundaries causes a reduction in the grain boundary surface energy or strain concentrations cause dislocation emission and crack initiation. The most recent addition to the mechanism literature is the series of papers by Lynch[7-10] supported by the work of Ashok et al.[12] This model is similar to the reduced cohesion concept[31,32] in that embrittlement is attributed to adsorption of liquid metal atoms at the crack tip. The difference is that rather than reducing the cohesive strength of the crack tip bonds, the stress required to emit dislocations is reduced. The crack grows by localized enhanced plastic deformation. Each of these mechanisms will be discussed below.

The earliest mechanism, reduced cohesion, states that adsorption of liquid metal atoms at the crack tip must occur first. The adatoms react with the bonded atoms which form the crack tip. Assuming that the cohesive strength of these bonds determines the stress at which the crack grows, the authors of this mechanism state that the presence of the adatom reduces the strength of the crack tip bond. The arguments are developed using the potential energy of the two crack tip atoms at their equilibrium positions. The adatom effectively lessens the potential energy and increases the interatomic spacing at the crack tip. The lower potential energy requires that less stress is necessary to separate the atoms permanently, causing crack growth.

The second mechanism, proposed by Roberston,[33] deals with very rapid dissolution of the solid metal at the crack tip by the liquid metal. This model states that the crack tip is constantly and rapidly dissolved by the liquid metal. The dissolved metal must be quickly carried away from the crack tip for the reaction to proceed. Many criticisms have been lodged against this mechanism, particularly with respect to the predicted and actual effects of temperature and it has not been accepted to any large degree.

The grain boundary penetration model[34] was proposed at about the same time as the rapid dissolution model. The mechanism proposes that liquid metal atoms adsorbed at the solid metal surface diffuse along grain boundaries, facilitated by applied stress. Once a sufficient concentration of embrittling atoms is present along the grain boundaries, the surface energy of the grain boundary is reduced sufficiently to cause embrittlement. This model seems to explain the static fatigue behavior observed in some LME couples, but it does not predict any transgranular, often cleavage type, fracture that has been observed.

Most recently, Lynch[7-10] proposed enhanced plastic deformation. Based largely on fractographic and crack tip profile studies, Lynch claims that liquid metal atoms adsorbed at the crack tip do not facilitate decohesion; rather, they enhance dislocation emission from the crack tip. Using high resolution electron microscopy, very small and shallow dimples were observed. Polished and etched transverse sections revealed slip lines that intersect the crack tip. These findings are contrary to the other proposed mechanisms, in particular the reduced cohesion mechanism, which predicts totally brittle fracture with no evidence of plastic deformation. The enhanced plasticity model states that adsorbed liquid metal atoms at the crack tip locally change the properties at the crack tip bond. The potential energy is decreased, as in the reduced cohesion model, but, important to this mechanism, the shear modulus also is reduced. Since the shear stress necessary to produce dislocations is proportional to the modulus, it is possible that dislocation emission is enhanced due to the presence of the liquid metal adsorbed at the crack tip.

This explanation of LME (also applicable to other types of embrittlement) has been the subject of much controversy in the recent literature. In an attempt to study the mechanism from a totally different viewpoint, Ashok et al[12] have studied LME in amorphous metals. These metals fracture by a shearing process in inert environments. It was thought that if reduced cohesion is the mechanism of LME, no evidence of shearing should be present when fractured in liquid metal environments. The results of these experiments showed clearly that fracture still indeed occurred by a shearing process, further strengthening the position of Lynch.

This brief outline of the phenomenon of LME can be summarized in the following manner. LME is a relatively rare occurrence that has been the subject of substantial research. Embrittlement occurs as the result of a multi-step process to which many variables contribute. Much work has been done, but because of the complex nature of the embrittlement, significantly more work must be accomplished before an all-encompassing theory for LME can be developed.

2.2 Fracture Mechanics Applied to Environmental Sensitive Fracture Phenomena

Fracture mechanics test methods enable the detailed study of the mechanics of crack growth, from which certain empirical laws have been developed. The experimental results presented herein were obtained using such tests and are discussed in comparison to the previously observed empirical laws. To do this, the pertinent fracture mechanics parameters must first be introduced.

Modern fracture mechanics began when Irwin[38] expanded upon the classic work on brittle fracture by Griffith.[37] Griffith considered the onset of crack growth a thermodynamic phenomenon which must obey the first law of thermodynamics. When a crack of length a grows an amount Δa, two things occur. First, two increments of crack surface are created, increasing the surface energy of the cracked body. Second, the ability of the body to store energy elastically, is decreased due to the increased compliance of the cracked body. If the crack growth obeys the first law of thermodynamics, the amount of energy released as elastically stored energy should equal the amount of the surface energy increase. This criterion applies to very brittle materials, but for materials which fail in a ductile manner with no cracks present, the Griffith criterion underestimates the loads which are required to cause a macroscopically brittle appearing fracture of ductile materials containing cracks. Irwin and Kies[36] found that the critical factor that governed the onset of brittle appearing fracture in ductile materials, is the rate at which the elastic strain energy is released when crack the grows. For engineering purposes it matters not whether this released energy goes into creating surfaces, or is dissipated by some other means. Thus, the first parameter of fracture mechanics is the strain energy release state (G), defined as

$$G = \frac{\partial U}{\partial a} \tag{2.5}$$

where U is the elastic strain energy, and a is the crack length.

Irwin[38] also found that there is a single parameter which governs the state of stress at the tip of an infinitely sharp crack in a continuum. The stresses in the vicinity of a crack tip, using the coordinates defined in Figure 2.1 are easily obtained from a Westergaard stress function[39]

$$\begin{aligned} \sigma_x &= \frac{K}{\sqrt{2\pi r}} \cos\frac{\theta}{2}\left(1 - \sin\frac{\theta}{2}\sin\frac{3\theta}{2}\right) \\ \sigma_y &= \frac{K}{\sqrt{2\pi r}} \cos\frac{\theta}{2}\left(1 + \sin\frac{\theta}{2}\sin\frac{3\theta}{2}\right) \\ \sigma_{xy} &= \frac{K}{\sqrt{2\pi r}} \sin\frac{\theta}{2}\cos\frac{\theta}{2}\cos\frac{3\theta}{2} \end{aligned} \tag{2.6}$$

No matter what loading is applied to the idealized crack, the stresses in the vicinity of the crack tip are of the form of Eq. (2.6). Since some cracks are more severe than others, the degree of severity of the crack must be governed by the value of the parameter K, the stress intensity factor. Thus, the second fracture mechanics parameter K is introduced.

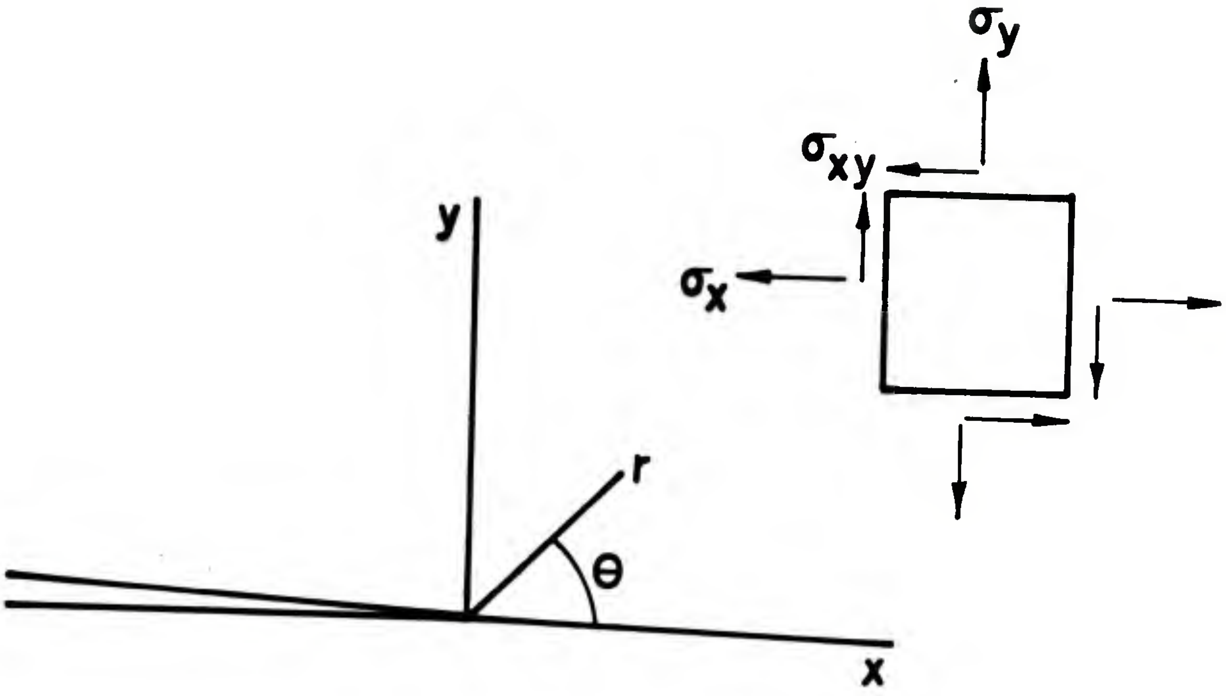

Figure 2.1. Stresses near a crack tip.

It is further shown by Irwin[38] that K and G are related as

$$K^2 = GE' \tag{2.7}$$

where E' is the elastic modulus E for plane-stress conditions, and E' is $E/(1-\nu^2)$, where ν is Poisson's ratio, for plane-strain conditions. Since K is a function of load, crack length, and specimen geometry, and material independent, the parameter is analogous to a stress parameter, more convenient to use than G. Therefore, the stress intensity factor is more often used to characterize cracks.

The use of fracture mechanics requires a pre-existing crack and is useful in measuring only the crack propagation stage of the fracture event. In aggressive environments, cracks can grow under either cyclic or static loading. We will define cyclic loading as cyclic fatigue and static loading as static fatigue. Since static fatigue crack growth tests are conducted with either fixed load or fixed displacement, we will use the terms displacement controlled static fatigue and load control static fatigue to differentiate between these two loading conditions. Useful empirical relationships have been developed relating K to the rate of crack growth under all three of these loading conditions.[41-47]

Using fracture mechanics samples, it can be shown that K is a function of three general variables (see Appendix A). These three parameters are specimen geometry, applied load, and crack length. Once a convenient specimen design is chosen, there are then just two parameters which determine K. Cyclic fatigue tests are normally conducted under constant alternating load conditions. This means that crack growth causes an increase in the K range (ΔK), and is shown in Figure 2.2a. Static fatigue tests can be conducted under two different controlling conditions, fixed load or fixed displacement. Figures 2.2b and 2.2c show the response of K to these conditions. For reasons to be explained below, a load control static fatigue test is conducted as follows. The load is slowly increased to a level at which the crack begins to grow, then is held constant. Subsequent crack growth results in K increasing with time. In a displacement control static fatigue test, the load is applied very quickly causing a corresponding increase in K to a high level. With constant displacement, crack growth necessitates a relaxation of the load, causing K to decrease with time, Figure 2.2c.

Of these three tests, the displacement control static fatigue test is the most difficult to control. If the initial K impulse is not fast enough, it is quite possible that crack growth will occur while K increases. This can lead to redundancy if a load control static fatigue test is subsequently performed. The importance of the static fatigue tests is that with both load and displacement control, the cases of increasing and decreasing K can be investigated separately. The results from these tests can be then related to the cyclic fatigue results, where K is constantly increasing and decreasing. Also, it is possible to actually arrest an embrittled crack in a displacement control static fatigue test. This same sample can then be tested under load control static fatigue conditions, minimizing the total number of specimens required to fully characterize the crack growth behavior.

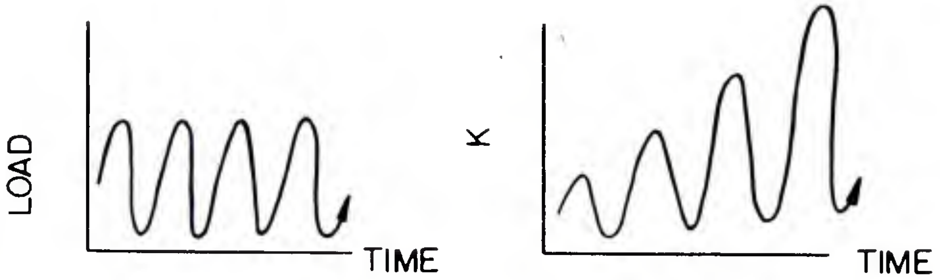

FIG. 2.2a CYCLIC FATIGUE

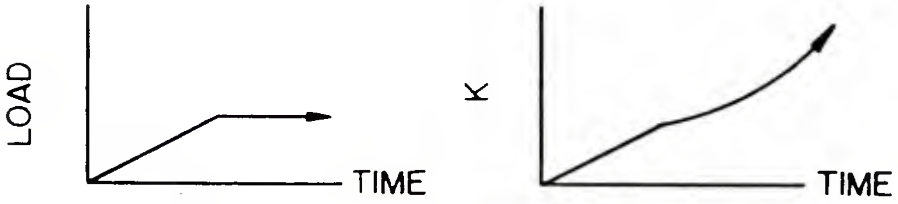

FIG. 2.2b LOAD CONTROL STATIC FATIGUE

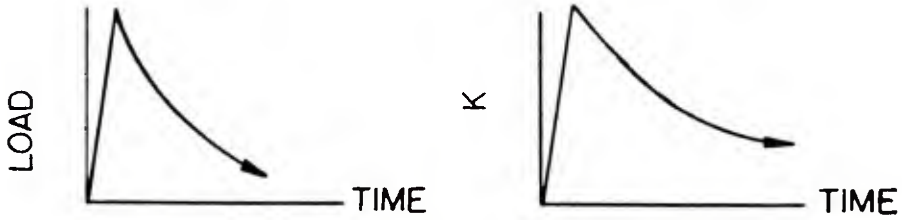

FIG. 2.2c DISPLACEMENT CONTROL STATIC FATIGUE

Figure 2.2. K responses to loading conditions.

Crack growth under all three external loading conditions has been studied in both inert and aggressive environments. The crack growth rate for cyclic fatigue tests is da/dN, which is that increment of crack growth which occurs per cycle of applied K. This crack growth rate has been found to follow a power law relationship with the range of applied K (ΔK) during testing[40]

$$\frac{da}{dN} = A\,\Delta K^m \tag{2.8}$$

This relationship holds only over a range of ΔK in inert environments known as the steady state fatigue crack growth rate region. At low values of ΔK, da/dN does not follow Eq. (2.8) and at some very low value of ΔK there appears to be no crack growth at all. At high values of ΔK, the maximum K applied approaches the fracture toughness (K_{Ic}) of the material, and the crack grows in an unstable manner and deviates from Eq. (2.8).

Several types of crack growth behavior under cyclic fatigue conditions in aggressive environments have been observed.[47] As shown in Figure 2.3a, a log-log plot of da/dN vs. ΔK is a straight line in an inert environment. In aggressive environments, such as aluminum alloys in water, the relationship marked aggressive in Figure 2.3a is observed. There is still a linear relationship with the same slope as in the inert environment, but the entire curve is shifted up or to the left. Regardless of applied ΔK, there is a constant increase in crack growth rate in the aggressive environment, when compared to the behavior in the inert environment. Figure 2.3b shows the type of behavior observed when high strength steels are cycled in hydrogen gas. The behavior in the environment is exactly the same as inert environments at

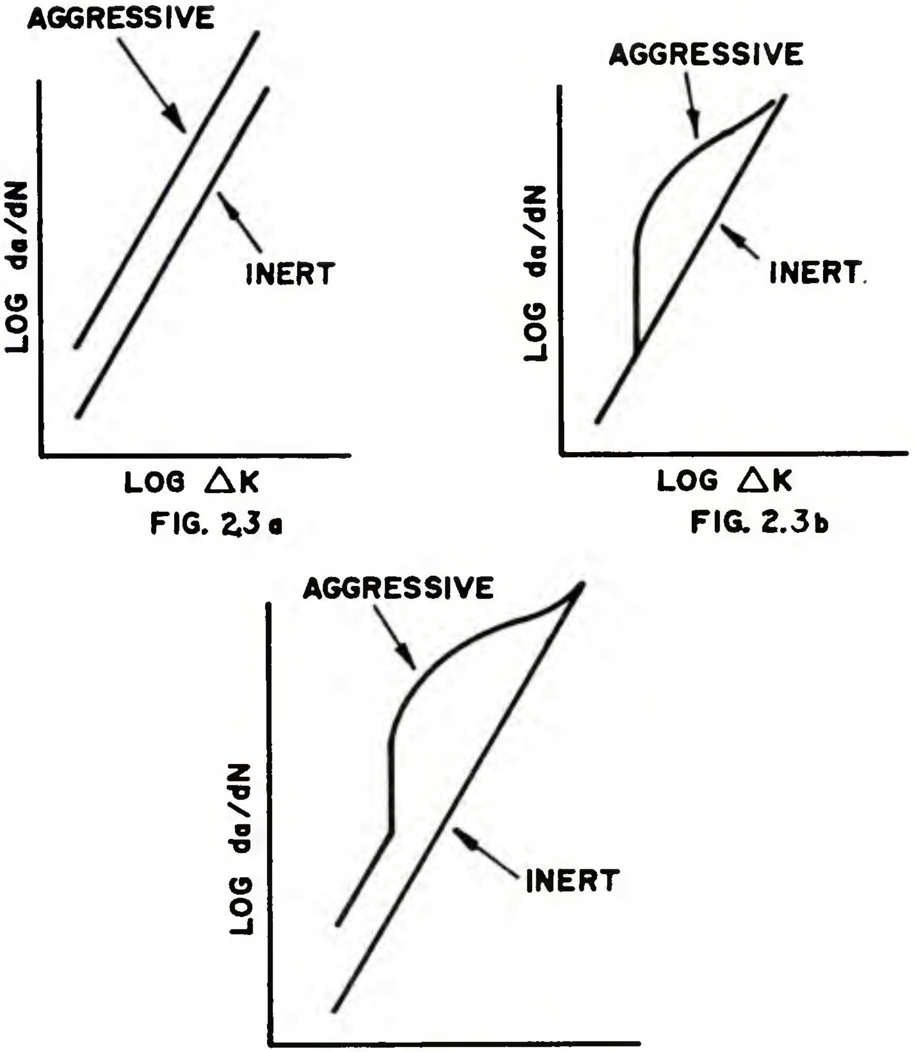

FIG. 2.3 a

FIG. 2.3 b

FIG. 2.3 c

Figure 2.3. Previously observed crack growth behavior conditions under cyclic fatigue.[47]

low ΔK levels. When the maximum K that occurs during cycling exceeds the apparent threshold stress intensity factor (K_{ISCC}), below which cracks apparently do not grow under static fatigue conditions, accelerated crack growth occurs. The crack growth rate increases rapidly with increasing ΔK, then levels off, and increases slowly with increasing ΔK. This type of behavior can be explained very well in certain cases, by the superposition of the crack growth which occurs under the static fatigue conditions, onto the crack growth response under cyclic fatigue conditions in inert environments.[45] The maximum crack growth rate in this type of behavior is a function of testing frequency, waveform, K ratio (K_{min}/K_{max}), and temperature. The third type of crack growth behavior is shown in Figure 2.3c. This behavior is basically a combination of the previous two and an example is high strength steel and water.

Crack growth in load control static fatigue,[42,43] and displacement control static fatigue[44,45] has been studied in many aggressive environments. The results of these studies show that there is basically only one type of relationship between the crack growth rate, now measured as crack velocity (da/dt) and K. This type of crack growth kinetics is shown in Figure 2.4. Below a certain value of K, called K_{ISCC}, there is apparently no crack growth, or at least crack growth which is very slow. Once K increases above K_{ISCC}, the crack growth rate increases very quickly. The crack growth rate then takes on a value that remains constant (a steady state velocity, or plateau). When the fracture toughness is reached, the crack grows in an unstable manner. The curve shown in Figure 2.4 is generally considered a material property. Exactly the same curve is obtained if it is measured using either static fatigue

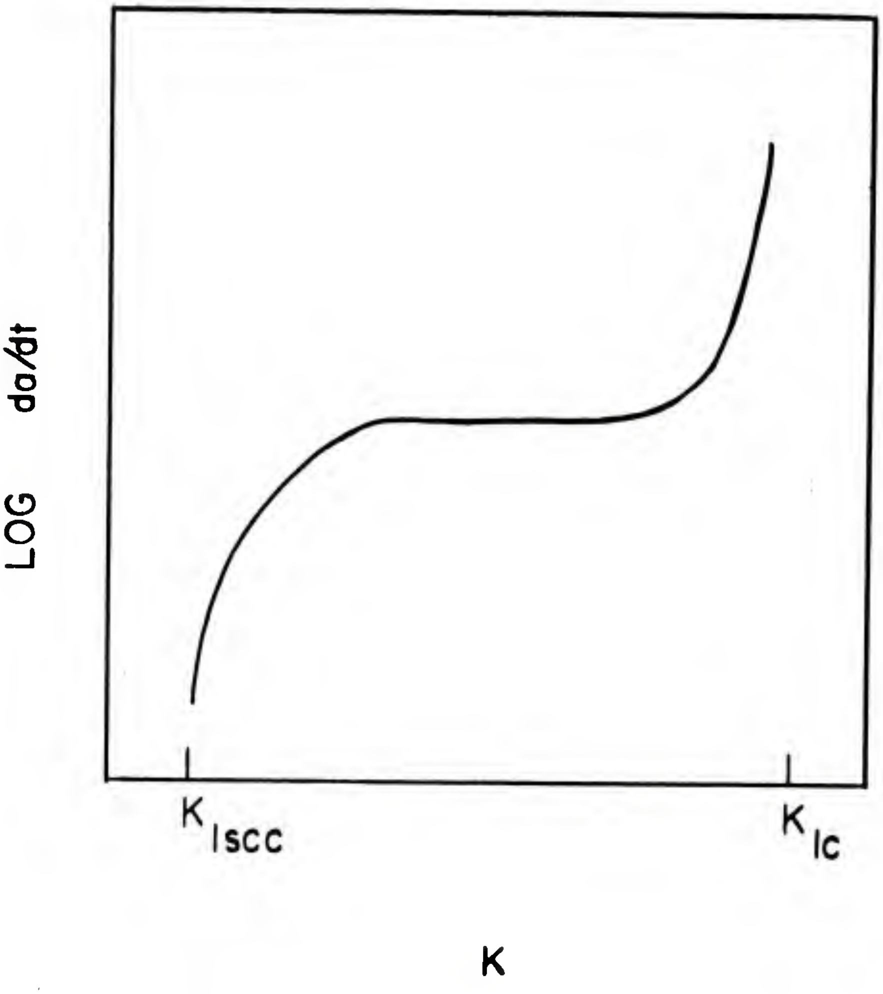

Figure 2.4. Previously observed crack growth behavior in static fatigue.[42-45]

loading condition. Since K_{ISCC} is an apparent threshold of crack growth, this value of K has engineering design significance. Most of the testing reported in the open literature, therefore, has been performed to determine this value of K.

Speidel[48] has shown a more complex type of crack growth response under static fatigue conditions. These measurements show two steady state regions of crack growth rate that are as much as several orders of magnitude offset. The results reported in reference 48 are for two aluminum alloys tested in an aqueous solution of KI. The two plateaus of steady state behavior are attributed to two different rate controlling processes. Also reported by Speidel are the only static fatigue measurements using fracture mechanics in LME. Displacement controlled tests were performed on 7075-T6 aluminum in liquid mercury. The results indicated that the crack growth response in LME follows Figure 2.4.

The static fatigue steady state region of crack velocity has been studied at various temperatures in some aggressive environments. These studies have resulted in important contributions to the formulation of the mechanism of embrittled crack growth.[43-47] It is assumed that the steady state crack velocity is a kinetically controlled process. Testing at different temperatures enables the measurement of the activation energy of crack growth. The value of activation energy can be used to infer what rate controlling process is governing crack growth in the environment.

The use of fracture mechanics has resulted in many contributions in the area of environmentally sensitive fracture phenomena. It is a technology which has enabled us to study the kinetics of crack growth under several loading conditions. This has led to not only an engineering predictive capability regarding damage tolerance, but also to a deeper understanding of fracture mechanisms. Also the special stress analysis techniques used at the crack tip have made theoretical contributions to the understanding of micromechanisms. Two papers by Rice[49] and Rice and Thompson[50] provide insight to the mechanisms of crack growth in both inert and aggressive environments. Since these papers deal directly with the results to be presented, they will be discussed thoroughly in a later section.

3. EXPERIMENTAL PROCEDURE

For this report the experimental variables of loading condition and temperature were studied using fracture mechanics techniques. All three types of loading were studied: cyclic fatigue, including frequency effects, load control static fatigue, and displacement control static fatigue. Furthermore, all tests were performed at several temperatures. Three different materials were tested in a single liquid metal.

3.1 Apparatus

Two specimens were used, a long double cantilevered beam specimen (LDCB), and a short double cantilevered beam specimen (SDCB), see Figure 3.1. There is a relationship between the applied load P, the crack mouth opening displacement under load CMOD, and the crack length a. The equations relating these parameters are given in Appendix A. The reasons for two different samples and the side grooves are also outlined in Appendix A.

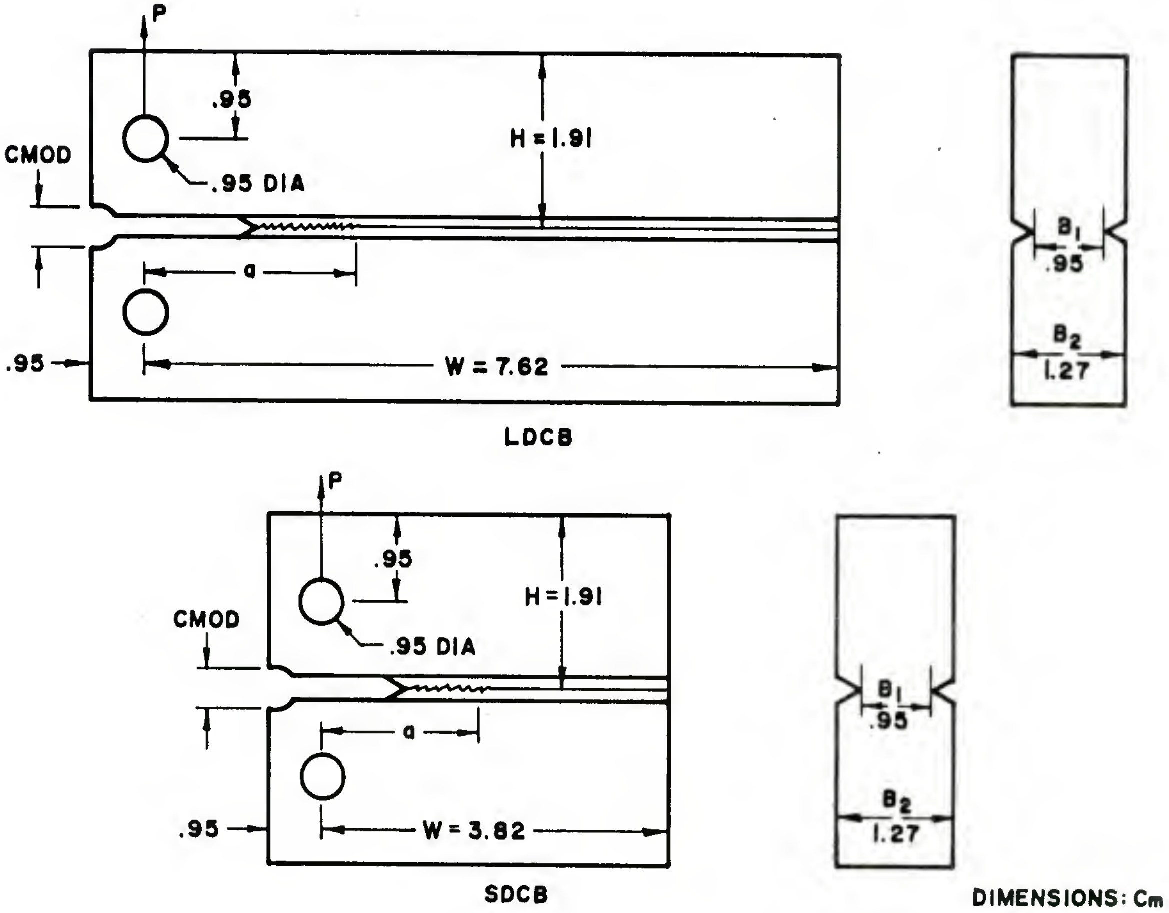

Figure 3.1. The specimens used.

Two testing machines were used to load the samples. The machines are shown schematically in Figure 3.2. The servo controlled hydraulic machine, Figure 3.2a, was used for both static fatigue test conditions and cyclic fatigue at low frequency. The rotating mass machine, Figure 3.2b, was used in the high frequency cyclic fatigue tests.

The servo controlled hydraulic machine operates as follows. A large, dual acting piston is connected to a moderate pressure hydraulic pump. The flow of the hydraulic fluid is controlled by a servo valve. The position of the piston, the pressure acting on the piston, and thus the load transmitted to the specimen, are controlled by the flow through the servo valve. The servo valve is controlled electronically by a servo controller. The servo controller directs the flow of hydraulic fluid by sensing either of two transducers: a load cell or a displacement gage. In load control, the servo controller senses the load P transmitted to the specimen from the load cell. Depending on whether the test was a cyclic or a static fatigue test, the dual acting piston was controlled accordingly. The type of test was determined by adjusting the function generator. For a displacement controlled static fatigue test, the piston was controlled by sensing the output of the displacement gage.

For the high frequency cyclic fatigue tests, the rotating mass machine shown in Figure 3.2 was used. The assembly of this machine results in the specimen being an in-line member of a spring mass-system. A mass placed on an adjustable rotor is connected to an electric motor which spins the rotor at a constant angular velocity of 30 Hz. The centripetal force generated is transmitted through loading rods to the specimen. This results in a

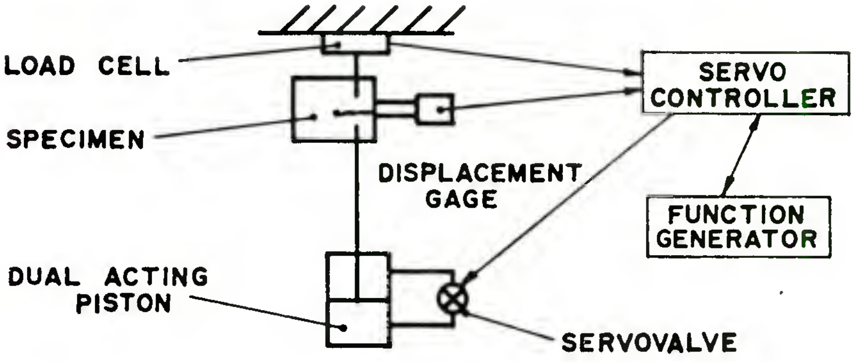

FIG. 3.2a SERVO CONTROLLED HYDRAULIC MACHINE

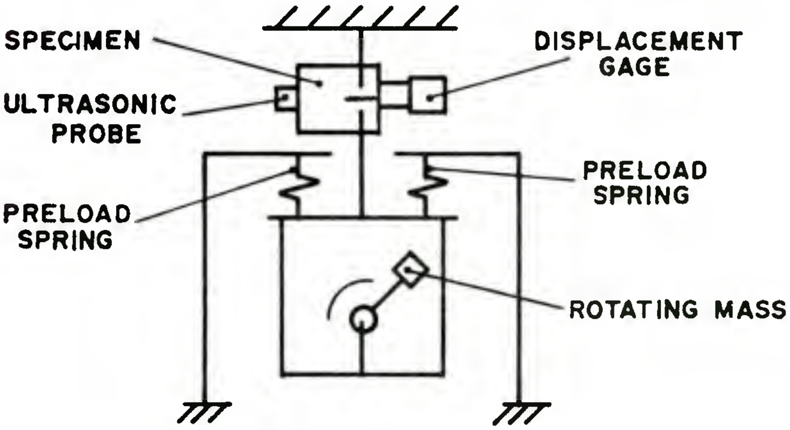

FIG. 3.2b ROTATING MASS MACHINE

Figure 3.2. Testing apparatus schematics.

sinusoidal, completely reversed, loading cycle. The load ratio (P_{min}/P_{max}) is adjusted by compressing or extending two symmetrically located stiff springs. This allows for tension-tension, or compression-compression loading cycles.

To use the relationships developed in Appendix A to infer crack growth, it was necessary to determine the CMOD and applied P simultaneously. The load and displacement were both measured on a dual channel X-Y plotter in the static fatigue tests. Signals from the load cell and the displacement gage were fed into the two Y channels of the recorder. The X axis was placed on a time sweep mode for the duration of the test.

For the cyclic fatigue tests, only the displacement range needed to be measured during a single cycle to infer the crack length, since the load range was held constant. To do this, the signal from the displacement gage was read into a high frequency strip chart recorder. The feed rate of the strip chart was varied manually to measure different rates of crack growth. Also shown in Figure 3.2b is an ultrasonic probe attached to a crack growth specimen. This probe was used to measure small amounts of crack growth, at slow crack growth rates.

Testing was also conducted at several temperatures using a commercially obtained temperature environmental chamber. The chamber was attached to the servo controlled hydraulic machine for the cyclic and static fatigue tests. The chamber controlled the temperature by the use of forced convection. For temperatures above ambient, the air inside the chamber was forced over resistive heating coils. When temperatures below ambient were required, liquid nitrogen was expanded into the chamber through a solenoid valve. The heating coils or solenoid valve were controlled by a temperature sensing device which constantly monitored the temperature inside the chamber. The gas temperature was controlled to within ±2°C.

A dummy specimen was outfitted with a thermocouple and placed in the environmental chamber. This was done to measure the actual response of the specimen to the conditions inside the chamber. The results showed that a specimen placed in a preheated or precooled chamber achieved the desired temperature in about five minutes. If both the specimen and the chamber were at ambient temperatures when the experiment began, the specimen obtained the required temperature in about ten minutes. Based on these findings, the specimens actually tested at other than ambient conditions, were soaked in the chamber for no less than 15 minutes before testing. The results of the dummy specimen experiments showed that once the testing temperature was obtained, the specimen temperature varied by no more than ±1°C.

3.2 Data Acquisition and Reduction

As stated, the usefulness of fracture mechanics is to study the subcritical crack growth stage of the fracture process. Under cyclic fatigue conditions in inert environments, this has normally been accomplished by polishing the sides of the sample. Crack growth is then determined optically, using a calibrated microscope.[40] The result is an actual measurement of crack growth at a given number of cycles. When plotted, these data were easily differentiated graphically.

In aggressive environments, the crack can seldom be measured optically. Other methods of measuring crack growth have been developed to alleviate this problem. Two of these techniques were used in this study. To measure small increments of crack growth, at slow growth rates, the end-on ultrasonic method was used. Developed by Underwood et al,[51] the method involved placing an ultrasonic probe on the back surface of the specimen. The probe was positioned such that it laid directly in the plane of the advancing crack. Small increments of crack growth (0.05 mm) were reliably and accurately measured with this technique. Because this was a manual method, it was only applied to measure relatively slow crack growth rates.

Fast crack growth rates resulted when testing took place in the liquid metal environment. This necessitated the use of another method for measuring fast crack growth. The method applied in this case is commonly known as the "compliance method", but more correctly should be called the CMOD method. The technique, developed by Yoder and Crooker[52] for cyclic fatigue testing, has been used for quite some time in static fatigue testing.[41-43] The CMOD technique involves the simultaneous measurement of the load, P, and the CMOD. Using these measurements, the crack length was calculated using the equations developed in Appendix A.

Once the crack length was calculated it was necessary to find the crack growth rate, and the value of K, or ΔK at which the crack growth rate occurred. Several numerical techniques were suggested to do this.[53] The most accurate and reliable method was found to be graphical differentiation.[53] All of the results reported here were obtained in this manner. Plots of the crack length vs. either the number of cycles N, or time t, were made. A french curve was then used to fit the data. Using a straight edge, slopes were taken at various locations along the curve. This yielded accurate measurements for fatigue crack growth rate da/dN, or crack velocity da/dt, depending on the type of test that was being analyzed. The value of the crack length at which the slopes were generated, coupled with the loading conditions for that test, and K values were calculated using the equations developed in Appendix A, which corresponded to the previously measured crack growth rate.

Several tests were conducted on all the materials using the following sequence. First, cyclic fatigue tests were conducted at two testing frequencies (30 Hz and 5 Hz) in laboratory air at ambient temperatures (25°C). The loading levels used initially were chosen to result in crack growth rates on the order of about 10^{-9} m/cycle. These loads were determined based on the results of previous testing of the same materials.[54] Following the initial tests, cyclic fatigue tests were conducted at both frequencies at ambient temperatures in the liquid metal environment. The same load levels used to generate the air results were also used in these tests. This enabled the study of any threshold phenomena which may have occurred. After these tests were performed, the static fatigue tests were conducted. The static fatigue samples were precracked in the liquid metal environment at load levels which produced embrittlement in the cyclic fatigue tests. Once an embrittled crack was produced, precracking was stopped and the static fatigue test conducted. After all the materials were tested at ambient temperatures, one of the materials was tested at various temperatures, first in static fatigue and then in cyclic fatigue at 5 Hz. The static fatigue specimens were precracked at room temperature in the liquid metal environment as described above. The cyclic fatigue samples were tested completely at the temperature at which the data was taken.

To facilitate cracking, all specimens were first subjected to a compressive preload as outlined by Underwood and Kapp.[55] The magnitude of the static compressive load was twice the magnitude of the load range ΔP used in the precracking. This accelerated crack initiation, often by as much as an order of magnitude of cycles. The compressive preload produced tensile residual stresses at the notch tip which increased the load ratio P_{min}/P_{max}. Since this preloading procedure affected the actual testing conditions at the resulting crack tip initially, crack growth rate determinations were not made until the crack had grown at least several notch radii, or about 1-2 mm (notch radius = 0.25 mm).

The load ratio R was held constant for all the cyclic fatigue tests and precracking of the static fatigue specimens. For convenience R was chosen as 0.1. Also, all cyclic fatigue testing was conducted using sinewave loading. This is the only waveform available with the rotating mass machine.

3.3 Materials and Specimen Preparation

3.3.1 Physical and Mechanical Properties

One of the classic LME couples is solid aluminum embrittled by liquid mercury.[5] Fracture mechanics methods are easily applied to aluminum alloys. Three alloys were chosen to study the effects of yield strength (σ_{ys}) and fracture toughness (K_{Ic}) on embrittlement. Both of these properties have been shown to have strong effects on embrittlement by liquid mercury.[3] Furthermore, Speidel's cursory results[48] were obtained using this LME couple, which gives us a basis for comparing our results.

The three aluminum alloys chosen were: commercially pure aluminum 1100-0, Mg-Si aluminum alloy 6061-T651, and the Zn-aluminum alloy 7075-T651. The measured chemical composition of each alloy is given in Table 3.1, and compared to the nominal chemistry.[56] Commercial alloys were chosen basically for convenience and economy.

The alloys were obtained in rolled sheet form. Figure 3.3 shows a schematic of the material in the as received condition. Also shown in Figure 3.3 are the definitions of directions and planes which are useful in describing specimen and microstructural orientations.

For the crack growth studies it was decided to orient the specimens so the cracks would grow along the L direction in the LS plane. To accomplish this, specimens were obtained from the rolled sheets as shown in Figure 3.4. Also shown is the orientation of the tensile specimens that were used to measure the room temperature mechanical properties of the alloys. The tensile specimens used were standard button type, 9 mm test section diameter specimens. The tensile properties were obtained in accordance with ASTM Standard E-8, "Standard Method for Tension Testing of Metallic Materials".[57] The results of these tests are summarized for the three alloys in Table 3.2. Also presented in the table are the values of the elastic modulus E, for each alloy. These values were obtained from the stress-strain curves developed in the tensile property measurement tests, in accordance with the ASTM Standard E-11, "Test Method for Young's Modulus at Room Temperature".[57]

TABLE 3.1 CHEMICAL COMPOSITION OF ALLOYS TESTED

Element (wt %)

Alloy	Si	Fe	Cu	Mn	Mg	Cr	Zn	Ti	Al
1100-0									
Required*	1.0 Si+Fe		0.20	0.05	-	-	0.10	-	99.0
Measured	0.92	0.31	-	-	-	-	-	-	98.77
6061-T651									
Required*	0.4-0.8	0.7	0.15-0.40	0.15	0.8-1.2	0.04-0.35	0.25	0.15	Rem.
Measured	0.70	-	0.25	-	0.93	0.14	-	-	Bal.
7075-T651									
Required*	0.50	0.7	1.2-2.0	0.30	2.1-2.9	0.18-0.4	5.1-6.1	0.20	Rem.
Measured	-	-	1.40	-	2.26	0.24	5.91	-	Bal.

*If no range is given, the wt % given in the required column is the maximum allowed wt %.

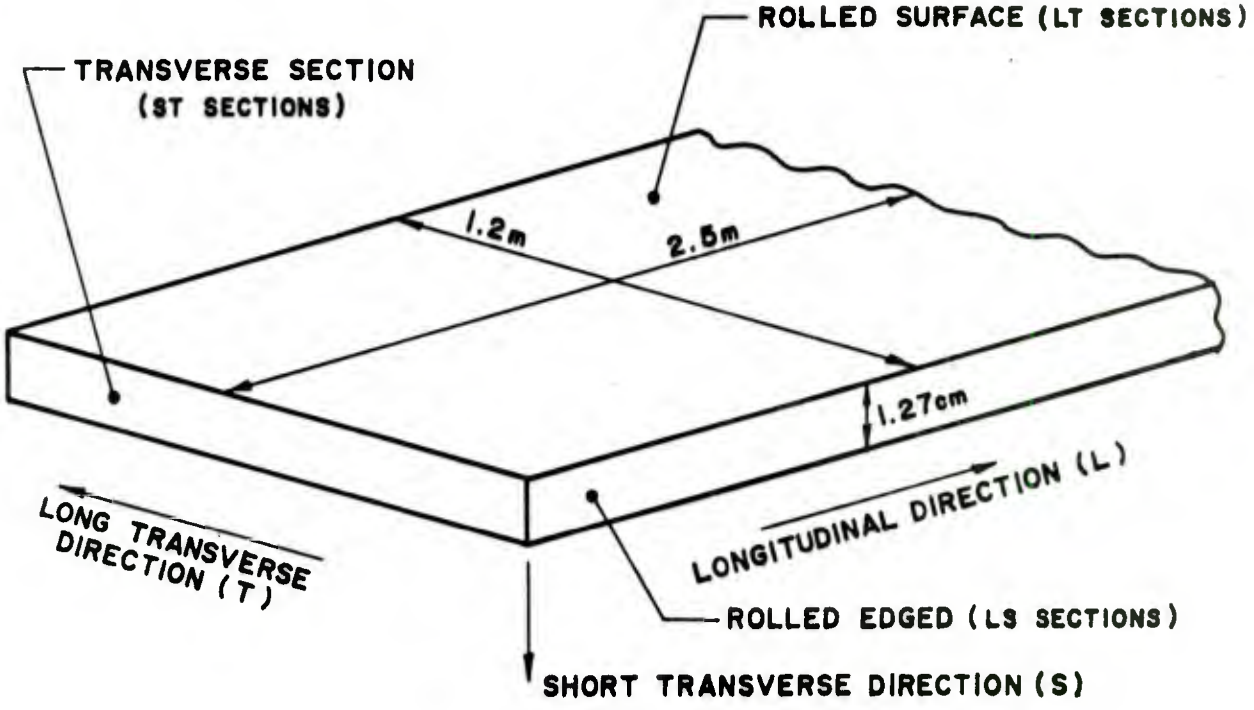

Figure 3.3. Material orientation in the as received condition.

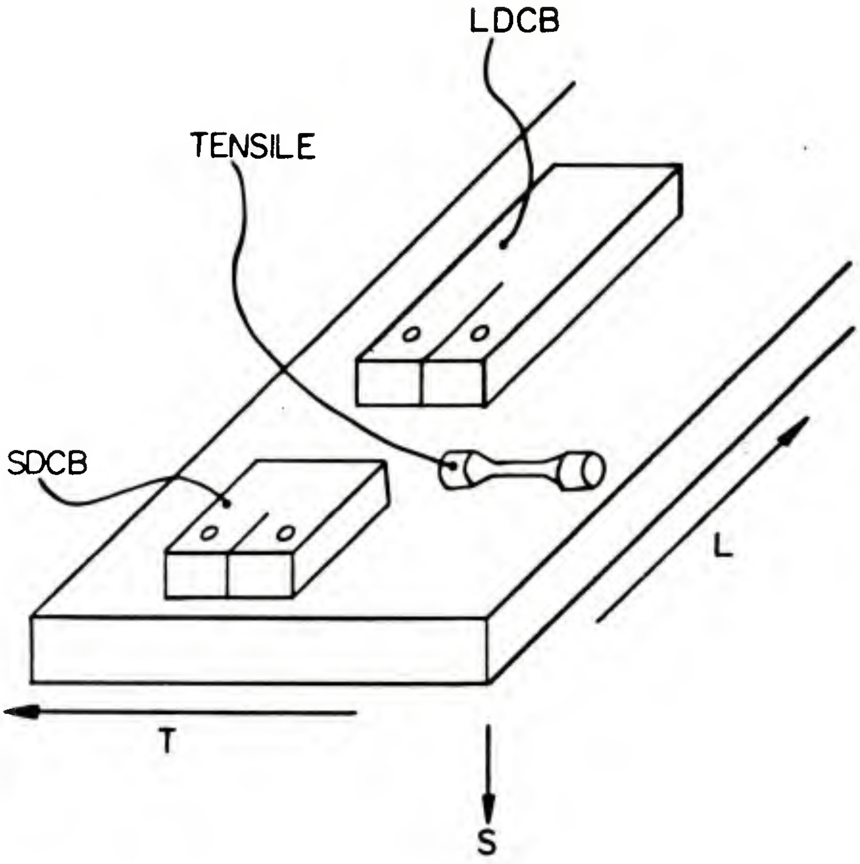

Figure 3.4. Specimen orientations.

TABLE 3.2. ROOM TEMPERATURE MECHANICAL PROPERTIES OF THE ALLOYS TESTED

Alloy	0.1% σ_{ys} MPa	σ_{uts} MPa	% RA	% Total Elongation	K_{Ic} (MPa$\sqrt{m}$)	E(GPa)
1100-0						
Measured	27.7	71.6	90.6	52.8	45.5	68.9
Nominal	34.5	89.6	-	35-40	-	68.9
6061-T651						
Measured	282.0	312.3	35.7	14.3	31.5	68.0
Nominal	275.8	310.2	-	12-17	-	68.9
7075-T651						
Measured	517.1	590.3	18.2	12.8	30.5	70.5
Nominal	503.3	572.2	-	11	-	71.7

The fracture toughness properties reported in Table 3.2 were obtained using SDCB specimens. The procedure was in accordance with the ASTM Sandard E-399, "Test Method for Plane Strain Fracture Toughness of Metallic Materials". Although the SDCB specimen is not a standard fracture toughness specimen, the method outlined in E-399 was applied to obtain a valid measurement of fracture toughness. The toughness of the 1100-0 alloy was measured using the J_{Ic} method, ASTM E-813, "Test Method for J_{Ic}, a Measure of Toughness". The different technique was necessary because of the size requirement of ASTM E-399. Since the 1100-0 alloy has such low strength, SDCB samples machined from the rolled sheets were not thick enough to meet the requirement of plane-strain conditions at the crack tip. Therefore, the toughness value reported in Table 3.2 for the 1100-0 alloy is not really a K_{Ic} value. It has been shown that the value of K which corresponds to J_{Ic} is somewhat less than K_{Ic}.[58]

3.3.2 Heat Treatment and Microstructure

As stated, the major metallurgical factor that was tested in this report was yield strength, or toughness (fracture strength). This parameter was changed by using three alloys of different strengths. The three alloys were described chemically and mechanically above. In this section, the microstructure and the heat treatment used to produce the microstructure are discussed. Table 3.3 gives the heat treatment procedures for each alloy.

TABLE 3.3. HEAT TREATMENT OF THE ALLOYS TESTED

Alloy	Anneal Temp (°C)	Anneal Time (hrs)	Heat Treatments Solution Temp (°C)	Precipitation Treatment Temp (°C)	Precipitation Treatment Time (hrs)
1100-0	340	8	-	-	-
6061-T651	-	-	520	175	6-10
7075-T651	-	-	870	120	24-28

The three aluminum alloys tested were designated as 1100-0, 6061-T651, and 7075-T651. The four digit number signifies that the alloy is a wrought alloy. Casting alloys have different designations. The first of the four digits signifies the general class of alloys, based on chemical composition. The 1XXX series is 99 percent by weight aluminum, the 6XXX series consists of aluminum-silicon-magnesium alloys, and the 7XXX series consists of aluminum-zinc alloys. The final three digits are assigned to each particular alloy in the general series of alloys. The numbers that follow the four digit numbers indicate the heat treatment of the alloy (-0, -T651).

Two of the alloys are heat treatable (6061 and 7075), while the 1100 alloy is not. The strength of heat treatable alloys can be either increased or decreased with heat treatment. The strength of the non-heat-treatable alloys can only be decreased by heat treatment; such alloys can only be hardened by mechanically working. The lowest yield strength aluminum alloys are the 1XXX series in the annealed condition (designation -0). The anneal for the 1XXX alloy tested was accomplished by heating it to a temperature at which recrystallization occurred, and holding it for a sufficient time to allow for total recrystallization. This effectively removed any remaining hardening effects from the manufacturing process. The temperature and hold times used for the 1100 alloy anneal are shown in Table 3.3.

The two heat-treatable alloys tested have the temper designation -T651. This temper results when the alloys are heat treated by solution treating, followed by a mechanical stress relief, then aged at the same temperature and time that would result in peak hardness if no stress relief operation had been performed.[59] The mechanical stress relief is applied primarily for practical reasons. After solution treating, macroscopic residual stresses often occur which can distort the processed material. By mechanically stretching the material to produce a permanent set, the residual stresses are removed. For the materials studied here, the magnitude of the permanent set from stretching was 1.5 percent to 3 percent. Such a stress relief allowed for easier further processing of the heat treated plates, but reduced the maximum strength attained by aging.

The actual heat treatments for each alloy studied are shown in Table 3.3. Both of the heat treatable alloys, 6061-T651 and 7075-T651, were purchased in the heat treated condition. The 1100 alloy was obtained in an "as fabricated" condition.

The microstructures of the three alloys tested are shown in Figures 3.5, 3.6, and 3.7. To fully characterize the microstructure of wrought aluminum alloys, the microstructure was examined and reported in the three mutually perpendicular directions defined in Figure 3.3. Three observations are necessary to envision the total three-dimensional microstructure.

For each micrograph, a small piece of material was cut from the plate and placed in a metallographic mount. Each sample was then polished on emery paper using successively finer grit from 240, 320, 400, to 600 papers. Polishing continued until all of the scratches from the previous operation were removed. This initial polishing was performed in a stream of tap water. Secondary polishing was accomplished using a high speed polishing wheel covered with a wool broadcloth impregnated with diamond particles of successively finer size, first with nine micrometer nominal size, then three micrometer, then one micrometer. A light oil was used as a lubricant. Polishing continued for three to five minutes, as required to remove the scratches from the previous operation. Scratch removal during secondary polishing was determined by examining each specimen with an optical microscope. Final polishing was accomplished by covering a polishing wheel with billiard cloth impregnated with a very fine (.01 micrometer nominal size) magnesium oxide powder.

To reveal the microstructure, all polished samples were etched with Keller's reagent (1 part HF, 1.5 parts HCl, 2.5 parts HNO_3, and 95 parts H_2O). Because the different alloys responded differently to the polishing procedure and the etchant, different etching times were required for the specimens from different alloys. For 1100-0 and 6061-T651 about two to three minutes of etching time was necessary, while the 7075-T651 required less than one minute to reveal the grain structure. The etchant was applied by swabbing the specimens.

Since all of these alloys were commercial alloys, not all of the alloying elements were dissolved in the metal matrix. The insoluble particles appeared in all the micrographs as black nodules. The particles were of different composition for each alloy. Figures 3.5a through c show the microstructure of the 1100-0 alloy. The black nodules are insoluble particles of $FeAl_2$.[60] These particles were not affected in size or density by heat treatment. Also, there is no evidence of cold work remaining in this alloy. Recrystallization is evident by the relatively large grain size, approximately 0.1 mm x 0.6 mm in the ST plane, 0.3 mm x 0.3 mm in the LT plane, and 0.3 mm x 0.6 mm in the LS plane.

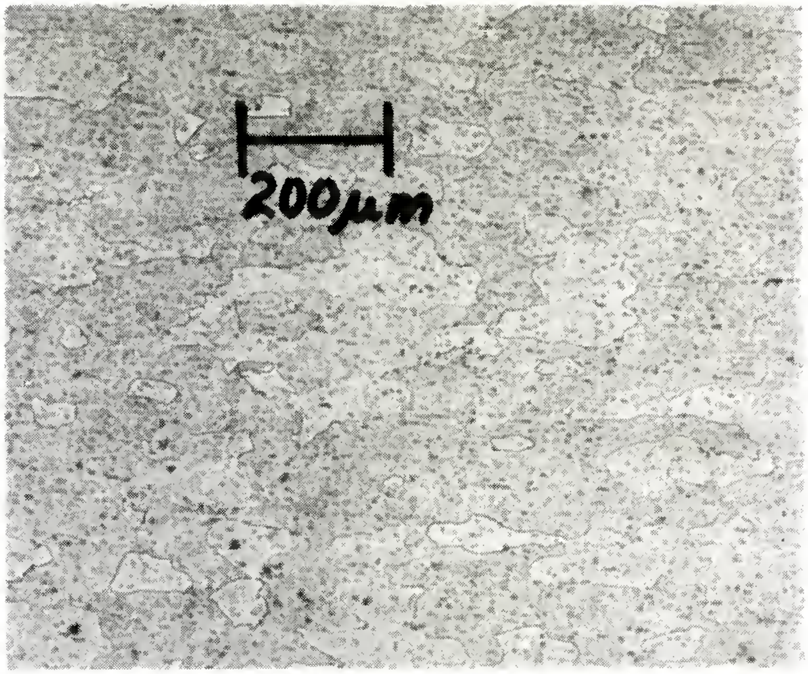

Figure 3.5a. 1100-ST Keller's reagent (100X).

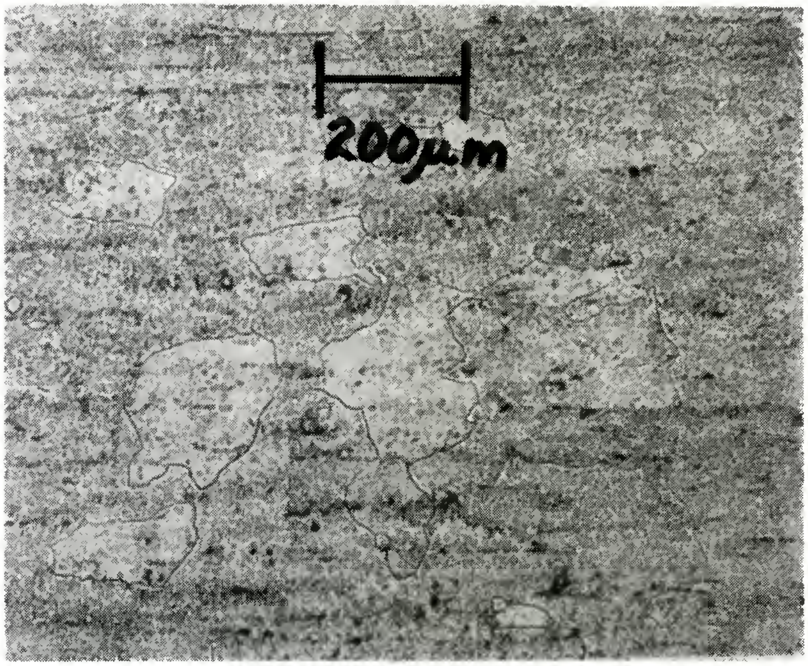

Figure 3.5b. 1100-LT Keller's reagent (100X).

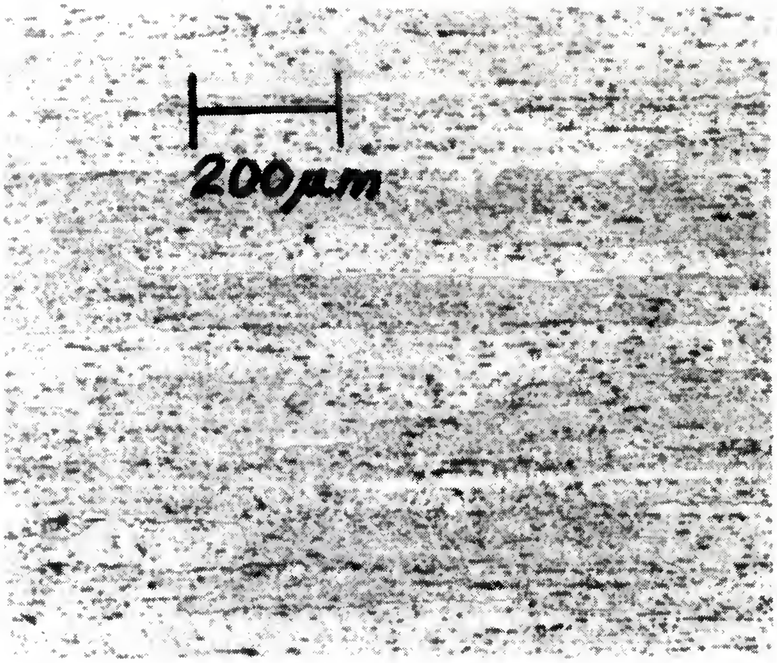

Figure 3.5c. 1100-LS Keller's reagent (100X).

In the 6061 alloy, Figures 3.6a through c, the precipitates are Mg_2Si.[60] As shown in the micrographs, these particles are essentially uniform in size. However, on the LT plane, Figure 3.6b, there is some evidence of the particles joining into what appear to be larger particles. In all the micrographs, the insoluble particles are banded along the working direction. The grains, similar to the 1100-0 alloys are not equiaxed. The grain size is about 0.1 mm x 0.8 mm in both the ST and LS planes. In the LT plane, the grains are about 0.3 mm x 0.3 mm in size. The size and distribution of the grains, being similar to the annealed 1100-0 alloy suggest that the 6061-T651 alloy was recrystallized prior to the solution heat treatment and aging.

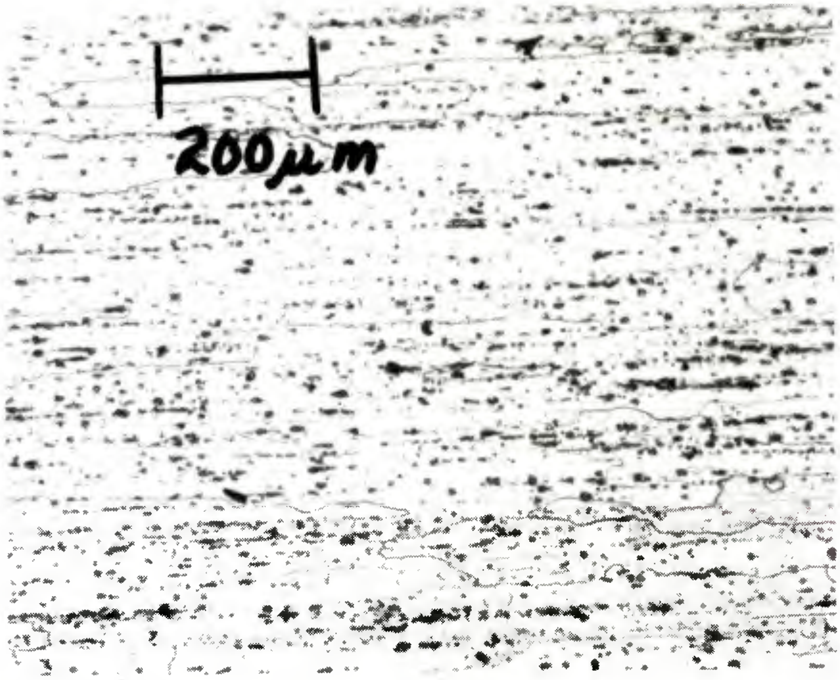

Figure 3.6a. 6061-ST Keller's reagent (100X).

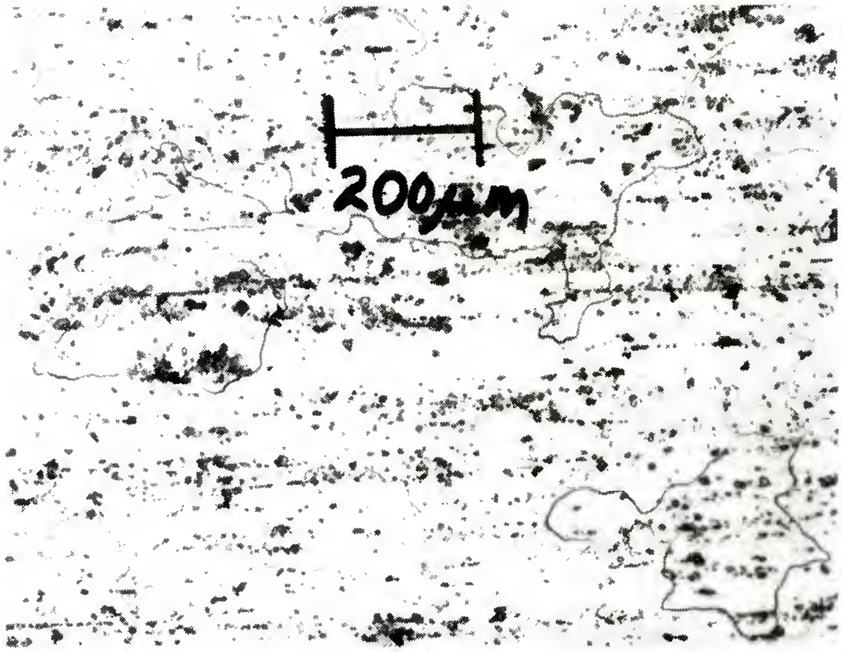

Figure 3.6b. 6061-LT Keller's reagent (100X).

Figure 3.6c. 6061-LS Keller's reagent (100X).

The microstructure of the 7075-T651 alloy is shown in Figures 3.7a through c. In this alloy the precipitates are $MgZn_2$,[60] and are not observed as insoluble particles. Unlike the other two alloys discussed, there seem to be two different and distinct types of insoluble particles present in the micrographs of this alloy. The larger particles are of lower density than those particles which appeared in the two previously discussed alloys. These particles seem to be banded in the working direction. The composition of the larger particles is of the type $(Fe,Mn)Al_6$.[60] The second, smaller insoluble particles are more difficult to perceive, but are best seen in Figures 3.7a and 3.7c. These particles have a chemical composition of $Cr_2Mg_3Al_{18}$.[60]

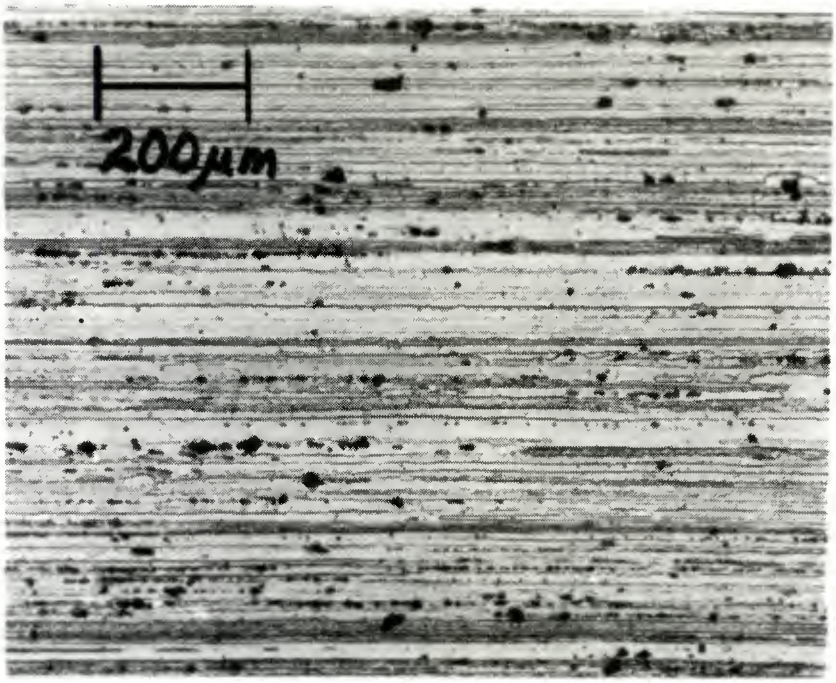

Figure 3.7a. 7075-ST Keller's reagent (100X).

Figure 3.7b. 7075-LT Keller's reagent (100X).

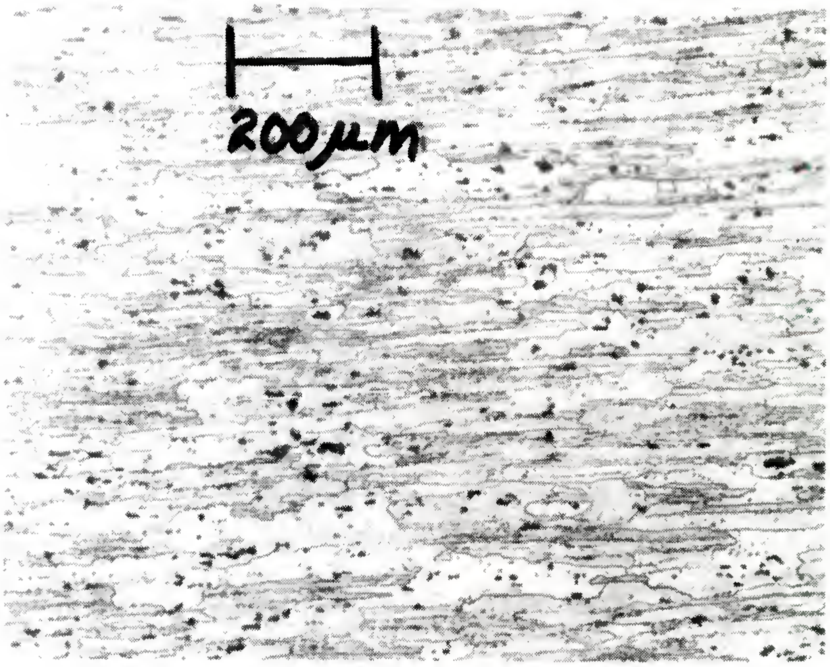

Figure 3.7c. 7075-LS Keller's reagent (100X).

The grain sizes of this alloy are approximately 0.05 mm x 0.8 mm in the ST plane, 0.3 mm x 1 mm in the LT plane, and 0.05 x 1 mm in the LS plane. The lack of an equiaxed structure in any plane suggests that this alloy was not annealed after working to final dimensions.

3.3.3 Plating Method for Wetting with Mercury and Fracture Surface Preservation Techniques

In previous studies on liquid mercury embrittlement of aluminum it has been shown that for embrittlement to occur, the liquid metal must be in intimate contact with the solid metal.[6] This is normally accomplished by cleaning the aluminum surface with a strong caustic or acid. The cleaned surface is coated with liquid mercury. This results in good wetting and embrittlement if the specimen is broken immediately after wetting. If the specimen is broken some time after the wetting procedure, embrittlement does not occur because aluminum surfaces de-wett. For this study it was necessary to fatigue precrack the samples in the environment to produce embrittlement, a process which in the 1100-0 and 6061-T651 alloys often required several hours. Therefore, this wetting procedure is inadequate.

To alleviate the wetting problem, it was decided to deposit a thin layer of copper on the surface of the aluminum alloy.[11] Embrittlement took place when the copper coating was broken by fatigue precracking. Copper was chosen because it can be easily electrodeposited on aluminum, easily wet with mercury, and remains wet almost indefinitely. This technique had the added advantage of being almost universally applicable, since copper can be electroplated on many materials. Also, since we measured only crack growth, not crack initiation, the plating method did not affect the results reported. If crack initiation had been studied, this wetting procedure may have been inadequate.

The SDCB and LDCB specimens used in the crack growth studies were first thoroughly cleaned by sand blasting, washed in water, then rinsed in alcohol.

The samples were then plated with copper by immersion in an electrolyte which had a composition of: 247g CuS per liter of water, and 60 g H_2SO_4 per liter of water. The operating conditions were: temperature of about 25°C and plating current of about 160 amperes/m^2. Plating time was about 30 minutes. These conditions resulted in a copper coating of about .025 mm per side.

After the specimens were broken, the fracture surfaces were prepared for examination in the SEM. Samples broken in air were cleaned in a bath of acetone in an ultrasonic vibrator, dried, and placed in a vacuum until examined in the SEM. The samples broken in mercury were more difficult to clean because the fracture surface was completely covered with mercury. Three methods were used to clean these surfaces. The first method was to place plastic replicating material on the surface which, when removed, cleaned the surface. This method was cumbersome since several replicas were necessary for cleaning. Also, the surfaces were often irregular and good cleaning was not possible over large surface areas. The second method was to evaporate the mercury in a vacuum at about 150°C. This resulted in a thorough cleaning of the surface, but often required several hours to complete. The third method was to dissolve the mercury in hot (75°C) concentrated nitric acid. This removes the mercury and the copper very quickly and does not attack the aluminum. This was verified by examining surfaces broken under identical conditions for 6061-T651 cleaned by either replication or the nitric acid method. The cleaned portions of the replicated surface showed the same features as the surface cleaned with hot nitric acid. The nitric acid method was used to prepare all of the surfaces shown in the later sections.

4. RESULTS

4.1 The Effects of Alloy (Strength) on Crack Growth Behavior at Room Temperature

4.1.1 Commercially Pure Aluminum 1100-0

The results of the cyclic fatigue tests of 1100-0 are shown in Figure 4.1. The results of the static fatigue K tests for the same alloy are shown in Figure 4.2. The cyclic fatigue results in air indicate that the material follows the Paris power law;[40] there is a linear relationship between log da/dN and log ΔK. Also, the data for both 5 Hz and 30 Hz fall on the same line for the tests conducted in laboratory air. This indicates that air is relatively inert to cyclic fatigue crack growth for this alloy.

The crack growth tests conducted in mercury under cyclic fatigue conditions (Figure 4.1) show that mercury has an accelerating effect on crack growth. There seems to be no effect of loading frequency on crack growth in mercury. These data deviate from the air results at a ΔK value of about 5 $\text{MPa}\sqrt{\text{m}}$. The data for both 5 Hz and 30 Hz frequencies then follow what appears to be a straight line with a much higher slope than was observed in air. Unfortunately, after about 15 mm of crack growth, the uncracked ligament of the samples collapsed from gross plastic deformation, and ΔK values of greater than about 10 $\text{MPa}\sqrt{\text{m}}$ were not obtained. Substantially faster crack growth was measured at 5 Hz than at 30 Hz before the collapse occurred, but sufficient data were not obtained to determine if this was due to a frequency effect. Nonetheless, it is apparent that crack growth is perhaps two orders of magnitude faster in mercury than in air.

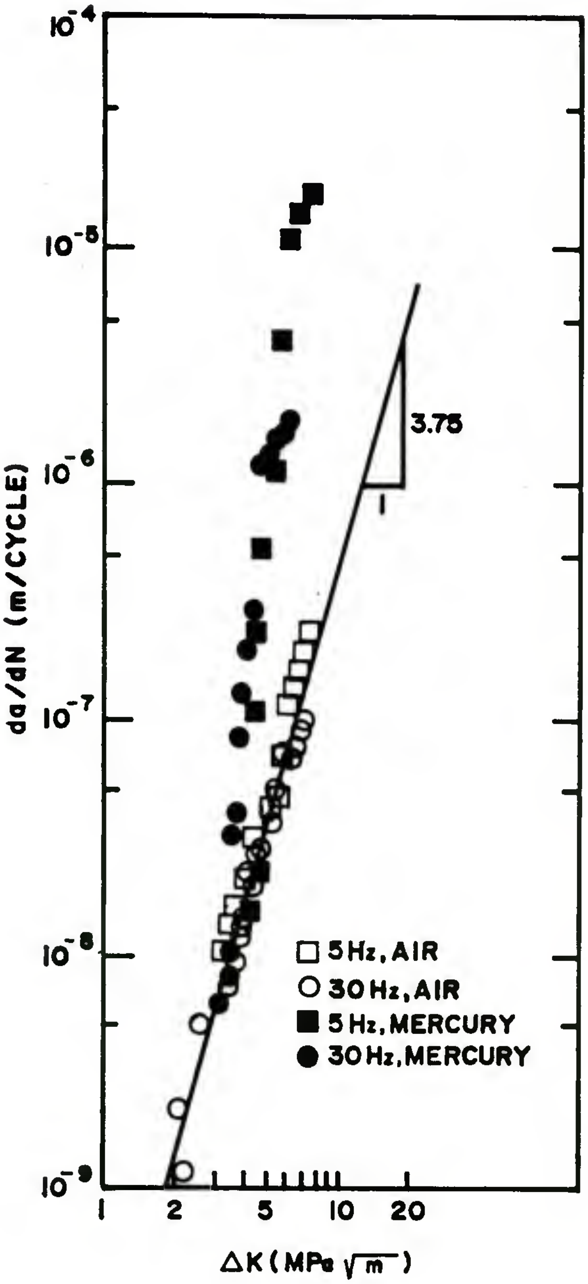

Figure 4.1. Cyclic fatigue results for 1100-0.

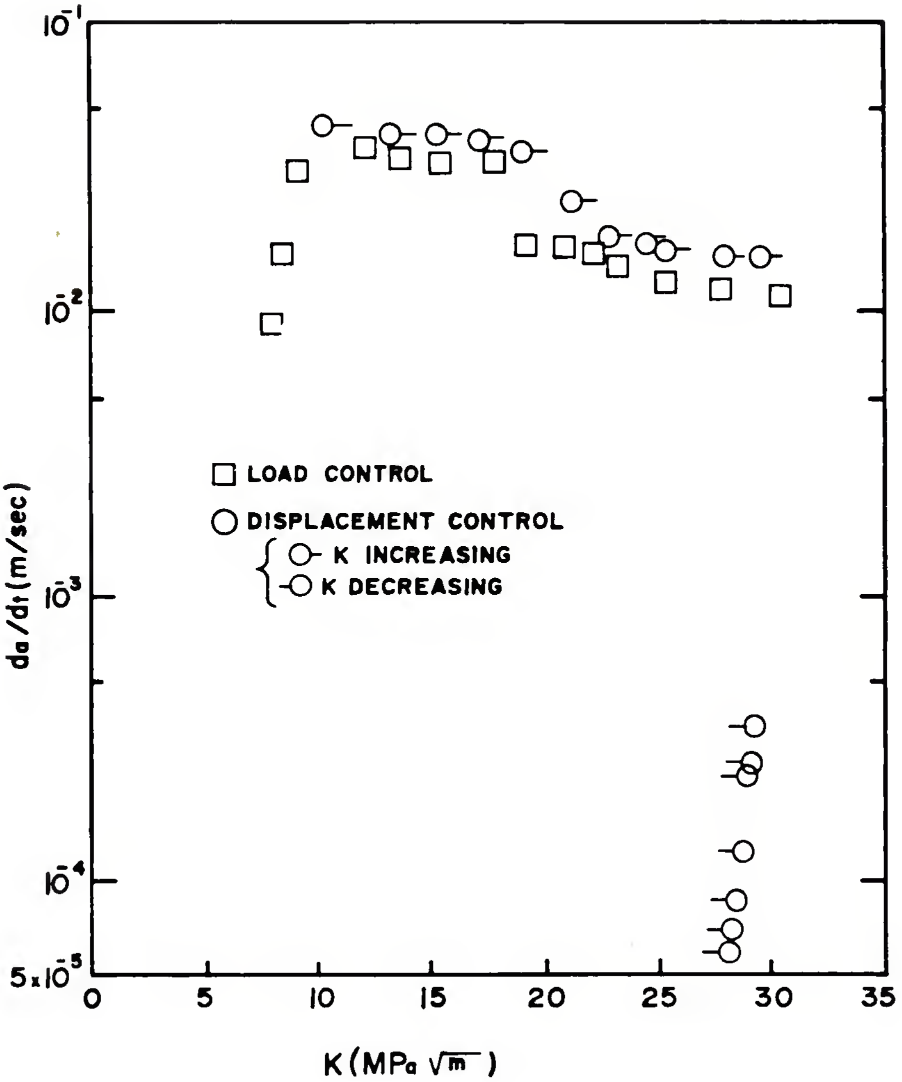

Figure 4.2. Static fatigue results for 1100-0.

Another important finding is that below a certain value of ΔK, there is apparently no effect of the mercury on crack growth rate. Above this value of ΔK the crack growth rate increases very quickly with increasing ΔK over a small range of ΔK. This is similar to the behavior observed when testing steels in hydrogen gas under cyclic fatigue conditions (see Figure 2.3b).

The crack growth behavior under static fatigue conditions is shown in Figure 4.2. Under load control conditions, there was little or no crack growth until K reached a critical value (~ 7 MPa$\sqrt{m}$). Once this threshold K value was obtained, the crack accelerated to a very high crack velocity of about 3-4 cm/s. As K increased further, the crack velocity remained constant, then decreased to a somewhat slower velocity of about 1-2 cm/s until K became very large, and gross fracture of the sample occurred. In the displacement control test, the specimen was loaded to a large fixed displacement which resulted in a high K. Upon loading, the crack began to grow at approximately the same velocity as observed in the load control test. These crack growth data are plotted in the figure as displacement control, K increasing. The difference between the load control test and the displacement control test is that under load control K increased from crack growth, while in displacement control, K was increased by increasing the displacement. Once the maximum displacement and thus the maximum K were achieved, the crack velocity immediately fell several orders of magnitude to about 3×10^{-4} m/sec. For this alloy the crack grows very quickly only when K increases, and arrests when K decreases, even when the applied K is very high.

Two features of this crack growth behavior are unusual. Under rising K conditions, the crack apparently grows faster at lower K values than at higher K values. Previous observations in other environments have shown little or no effect on crack velocity with K in the region above the threshold K value (see Figure 2.4). Second, the crack velocity behavior under decreasing K conditions had previously been observed to be approximately the same as the rising K crack velocity behavior.[42-45]

The fracture surfaces observed in the SEM for the 1100-0 alloy are shown in Figures 4.3a through f. It is well known that in inert environments, the fracture topography is a function of ΔK, but not frequency under cyclic fatigue conditions. Since these ΔK effects have been discussed elsewhere,[61] only one representative SEM fractograph of fracture surfaces created under cyclic fatigue conditions in air will be presented for each alloy. Figure 4.3a shows the fracture surface created in air at ΔK of about 7 $\mathrm{MPa}\sqrt{\mathrm{m}}$ for 1100-0. The features shown in this fractograph have a generally rough appearance, accented by what appear to be sharp irregular ridges. No indication of microstructure is apparent. This topography is typical of ductile transgranular fatigue fracture.[61]

There is a distinct change in fracture appearance under cyclic loading in mercury, Figure 4.3b. The fracture mode is predominantly brittle intergranular with some secondary cracking at the grain boundaries. The intergranular nature of the fracture is also shown by the clear outline of the grain in the center of the micrograph (position A). There is also some indication of the topography that occurred in the air testing (position B).

Figure 4.3a. Fracture surface in air under cyclic fatigue conditions for 1100-0, $\Delta K \sim 7$ MPa$\sqrt{m}$, crack growth in the LS plane. The surface indicates a ductile transgranular fracture mode.

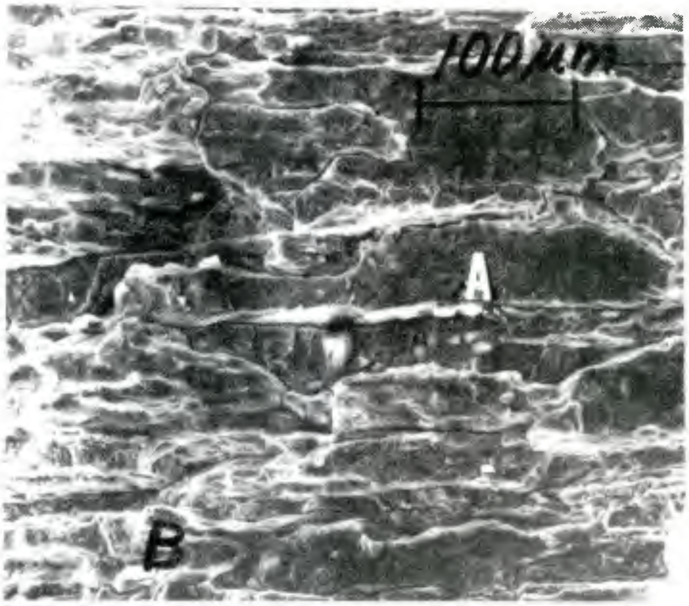

Figure 4.3b. Fracture surface in mercury under cyclic fatigue conditions for 1100-0, $\Delta K > 5$ MPa$\sqrt{m}$, crack growth in the LS plane. The fracture path is predominantly brittle intergranular.

The fracture surface created under load control static fatigue conditions is shown in Figures 4.3c and 4.3d. The surface topography shown in these two fractographs occurred at all locations along the surface where embrittlement occurred ($K > \sim 8$ MPa$\sqrt{m}$). The crack path seems to be intergranular, but the fracture mode is different than in the cyclic fatigue case. The fracture surface in Figure 4.3c is not smooth and the secondary cracks are opened very wide. An enlargement of one of the secondary cracks (Figure 4.3d) shows that the secondary cracks were created in a ductile fashion. Dimples are clearly visible in the crevices in Figure 4.3d. Also, there is a large density of small dimples on the surface created by the primary crack, many of which are centered around the insoluble particles.

Fracture surfaces in displacement control, static fatigue are shown in Figures 4.3e and 4.3f. This surface is somewhat similar to the cyclic fatigue fracture surface of Figure 4.3b, but there is some evidence of transgranular fracture, as indicated by the apparently cleaved grain in the center of Figure 4.3e (note the river patterns). At higher magnification, Figure 4.3f, some very fine secondary cracks are seen. There appear to be some elongated dimples scattered along the cleaved surface. Also, some elongated dimples similar to those in Figures 4.3c and 4.3d can be seen, but at a much lower density. These dimples also seem to have a relationship to the insoluble particles.

Figure 4.3c. Fracture surface in mercury for 1100-0 under static fatigue, load control conditions, $\Delta K > \sim 8$ MPa$\sqrt{m}$ with either K increasing or K decreasing. Crack growth in the LS plane. The fracture mode is dimpled intergranular.

Figure 4.3d. Higher magnification of Figure 4.3c, showing dimples.

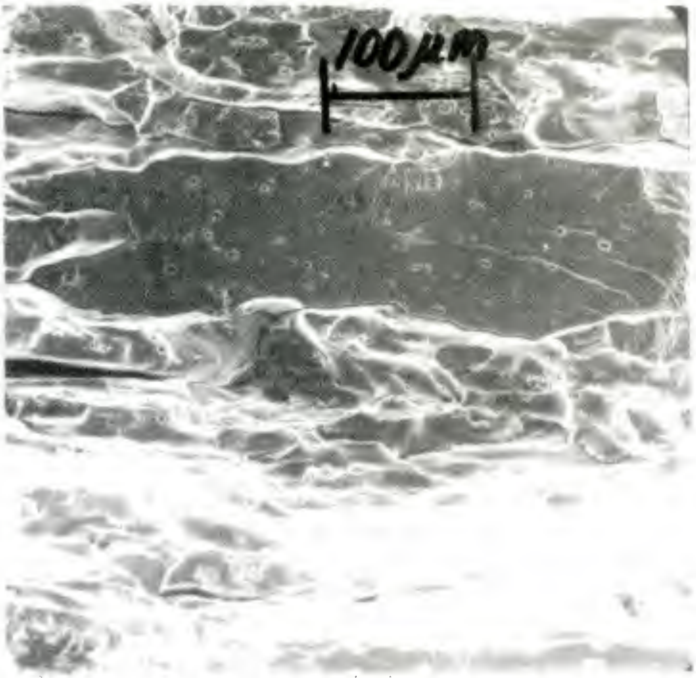

Figure 4.3e. Fracture appearance in mercury under static fatigue load control conditions for 1100-0, $\Delta K > \sim 8$ MPa$\sqrt{m}$. Crack growth in the LS plane. The fracture mode is predominantly brittle intergranular with some cleavage.

Figure 4.3f. Higher magnification of Figure 4.3e showing the apparently cleaved grain and small dimples.

4.1.2 Mg-Si Aluminum Alloy 6061-T651

The results of tests on 6061-T651 under cyclic fatigue conditions are shown in Figure 4.4. Again it is seen that the crack growth behavior in air follows the Paris power law relationship, and is in good agreement with the crack growth behavior previously observed in this alloy.[54] In mercury, the crack growth behavior is similar to the 1100-0 results at low ΔK values. Below a certain value of ΔK, approximately 7 or 8 MPa$\sqrt{m}$, there is no effect of the mercury on the crack growth behavior. Above this apparent threshold value, the crack growth in mercury is much faster and the general shape of the crack growth curve as a function of ΔK is approximately the same as the response of steel to hydrogen in cyclic fatigue.[47] The crack growth rate increases very quickly to a high value of da/dN over a very short range of ΔK. This is followed by a more gradual increase with increasing ΔK. Also, it is apparent that crack growth rates are one to two orders of magnitude faster when tests are conducted in mercury.

One aspect of the crack growth behavior in this alloy seems to be different than in the 1100-0 results. There is clearly an effect of loading frequency shown by the data. At about 20 MPa$\sqrt{m}$, da/dN at 30 Hz was about 2-3 x 10^{-5} m/cycle. At the same ΔK, but at 5 Hz, da/dN was about 3-4 x 10^{-4} m/cycle. In the initial stages of embrittlement, ($\Delta K \sim$ 8-10 MPa$\sqrt{m}$), the data at both frequencies showed the same response as the 1100-0 results. The crack growth rate is related to ΔK in a linear fashion, but with a much larger slope than occurs in air.

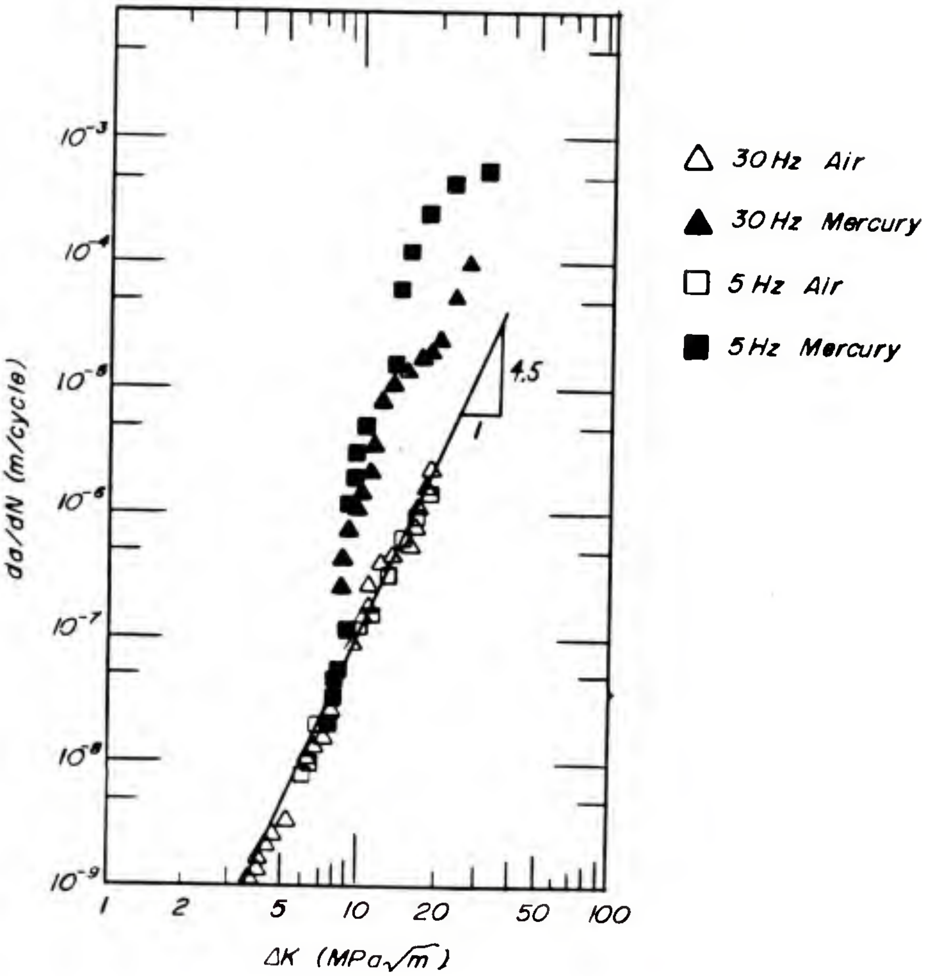

Figure 4.4. Cyclic fatigue results for 6061-T651.

The results from the static fatigue tests are shown in Figure 4.5. These results are quite unlike any other crack growth behavior previously observed in the literature. First consider the load control data. As K increased by increasing the load, no crack growth was apparent until K reached a very high value, approximately 13 $MPa\sqrt{m}$. Crack growth then began at about 5 mm/s and remained constant until K reached about 15 $MPa\sqrt{m}$. At this value of K, the crack velocity increased to about 4 cm/s and remained constant at this level until gross specimen fracture occurred. When tested under displacement control conditions, a different response occurred. The specimen was loaded to a very high K level, about 16 $MPa\sqrt{m}$, and crack growth proceeded at a velocity which was approximately the same as observed in the load control test. Similar to the tests on the 1100-0 alloy under the same conditions, crack growth occurred before the maximum displacement was attained, resulting in the data that fell on the upper plateau. Later in the test, the conditions were such that K decreased. As K decreased, there was a large and very fast change in the crack velocity from about 5 cm/s to about 5 mm/s at the same K level, about 19 $MPa\sqrt{m}$. As K further decreased, the crack velocity of about 5 mm/s continued until K was about 15 $MPa\sqrt{m}$, at which time the crack velocity began to decrease gradually to about 10^{-4} m/s at K of about 9 $MPa\sqrt{m}$.

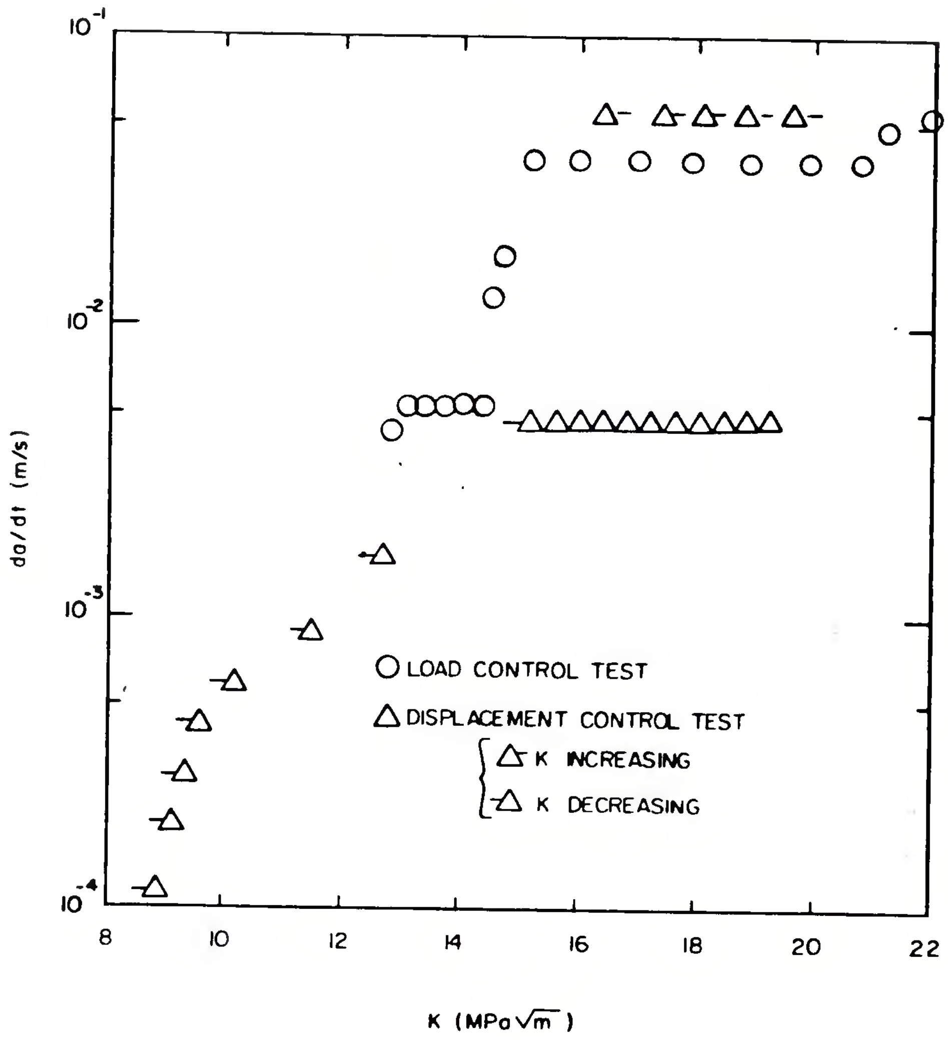

Figure 4.5. Static fatigue results for 6061-T651.

The fractographic features of this alloy are shown in Figures 4.6a through c. The fracture surface produced in air under cyclic fatigue conditions, Figure 4.6a, is similar to that observed in the 1100-0 cyclic fatigue air test. There are many ridges and no features which are related to microstructure, indicating a ductile fracture mode. The fracture surface of the sample broken under cyclic fatigue conditions in the mercury environment, Figure 4.6b, shows a much different appearance than the surface created in air for this alloy. This surface has fewer features than the surface produced in air and is predominantly smooth where the crack grew intergranularly. The degree of secondary cracking is not quite as extensive in this alloy as observed in the 1100-0. In general the fracture appearance is much more brittle than the surface broken in air. The fracture surface of the samples broken in mercury under static fatigue K conditions is shown in Figure 4.6c. There is no difference between the features created during either the displacement or load control tests. The surface indicates a predominantly intergranular fracture mode, similar to that observed under cyclic fatigue conditions, Figure 4.6b. There are certain differences however. Some dimples on the surface are shown in Figure 4.6c. Also there are shallow ridges parallel to the direction of crack growth. The ridges may be related to the banding of the insoluble particles, some of which can be seen along the ridges.

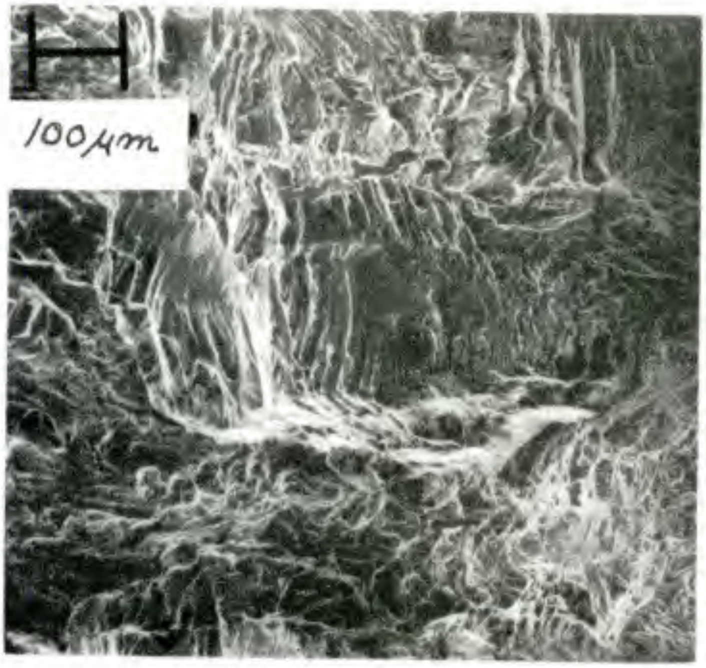

Figure 4.6a. Fracture appearance in air under cyclic fatigue conditions for 6061-T651. $\Delta K \sim 10 \mathrm{MPa}\sqrt{m}$, either 5 Hz or 30 Hz. Crack growth in the LS plane. The marker is 100 µm.

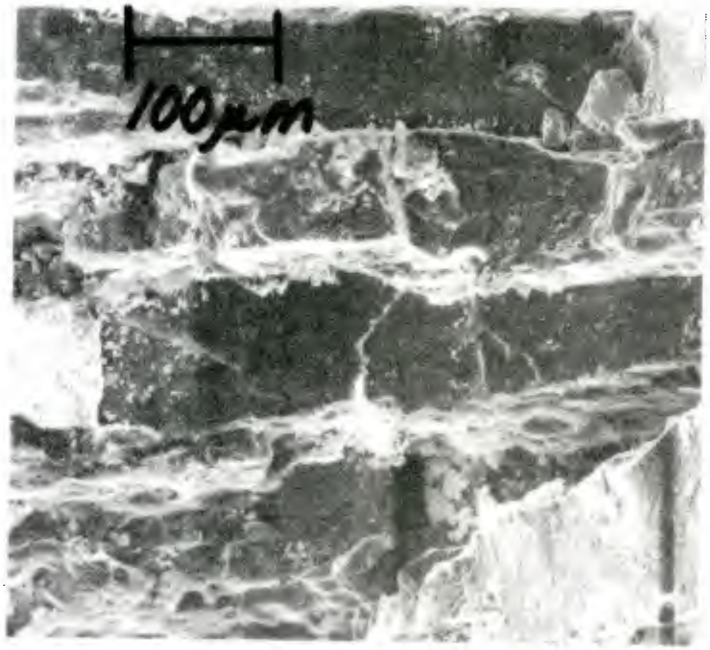

Figure 4.6b. Fracture appearance in mercury under cyclic fatigue conditions for 6061-T651. $\Delta K > \sim 8 \mathrm{MPa}\sqrt{m}$, either 5 Hz or 30 Hz. Crack growth in the LS plane. The fracture mode is brittle intergranular.

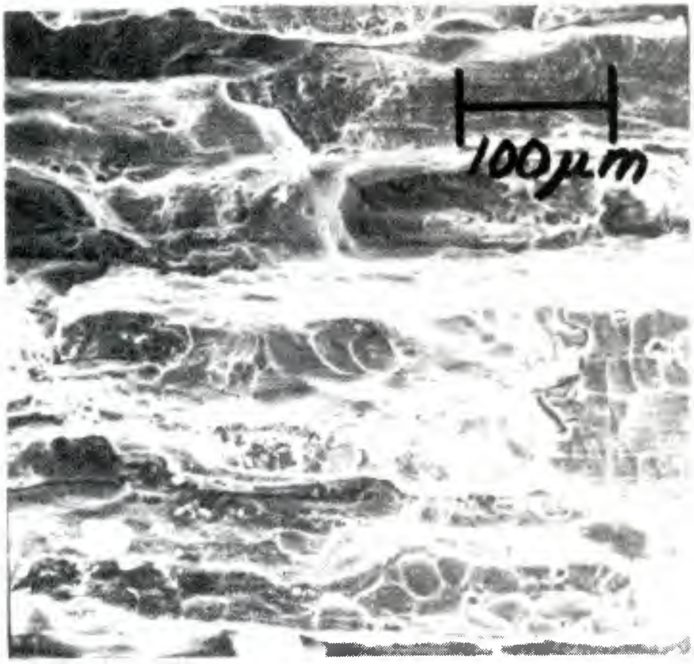

Figure 4.6c. Fracture appearance in mercury under static fatigue conditions for 6061-T651. $\Delta K > \sim 9 \text{ MPa}\sqrt{\text{m}}$. Crack growth in the LS plane. The fracture path is intergranular.

4.1.3 Zinc-Aluminum Alloy 7075-T651

The results for 7075-T651 under cyclic fatigue conditions are shown in Figure 4.7 and under static fatigue conditions in Figure 4.8. As with both other alloys tested, the crack growth rate behavior in air under alternating K conditions shows the linear relationship between log da/dN and log ΔK, and no frequency effect. The results in air are in good agreement with the previously observed behavior in this alloy.[54] The data obtained under alternating K conditions in mercury show that again the mercury accelerates crack growth by as much as four orders of magnitude for this alloy. As for the 6061 data, there is an effect of loading frequency on crack growth rate.

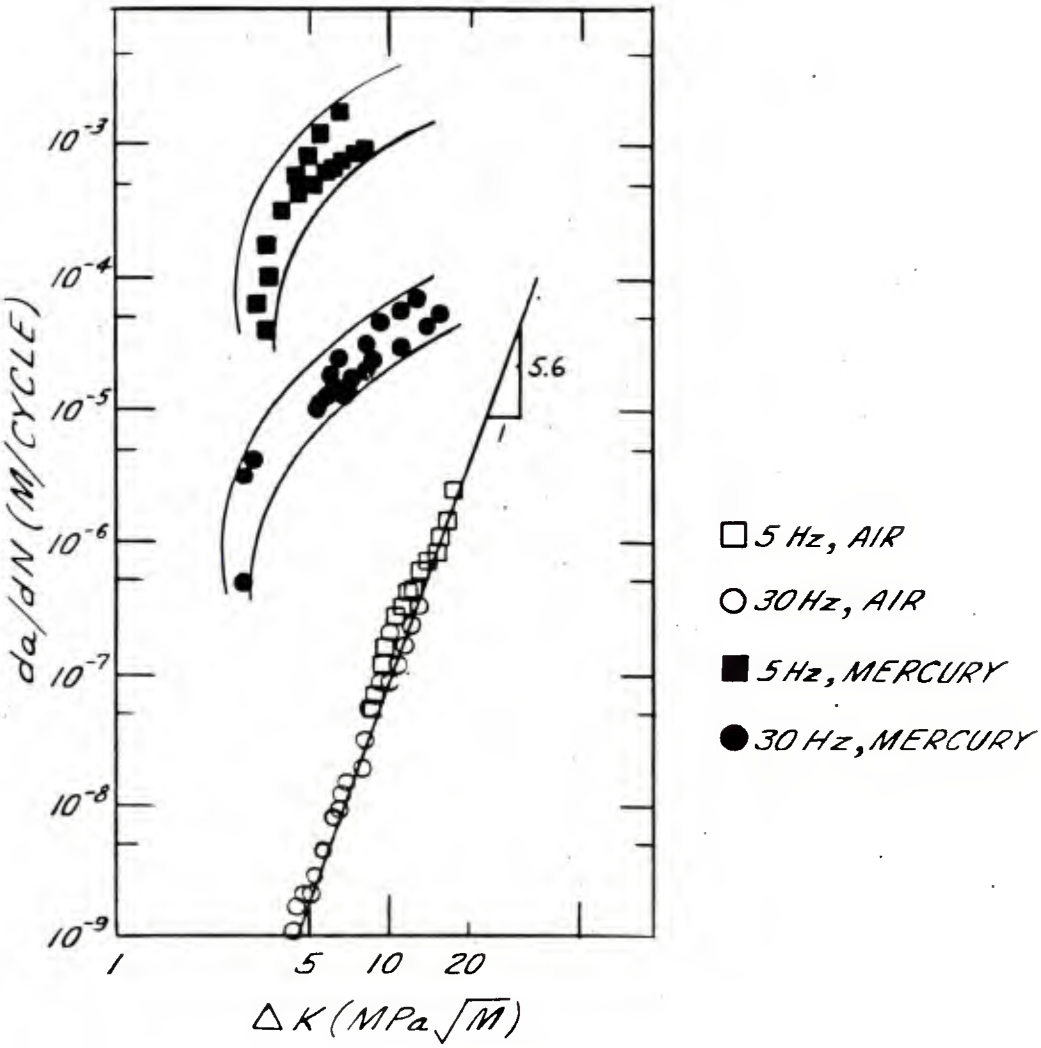

Figure 4.7. 7075-T651 cyclic fatigue results.

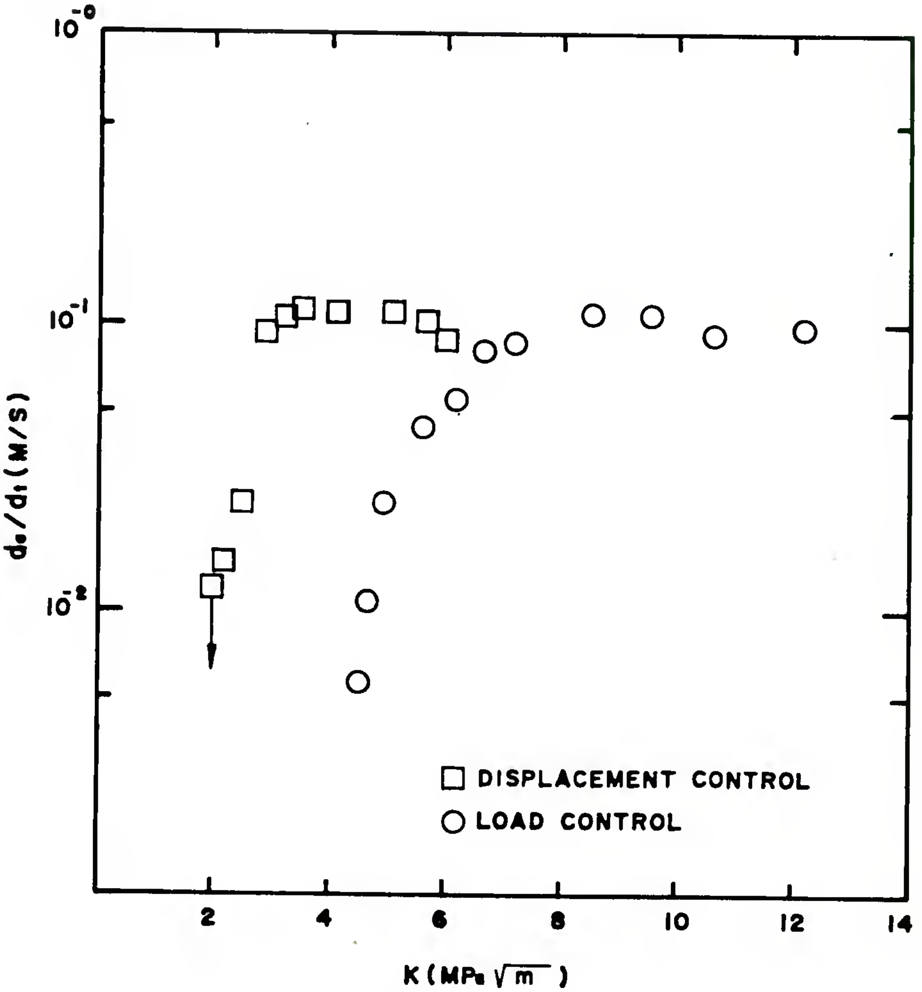

Figure 4.8. 7075-T651 static fatigue results.

The results do not show what type of crack growth behavior occurs prior to the very fast crack growth in mercury. Referring to the 5 Hz response in mercury, there seems to be a threshold at ΔK of about 3.5 MPa$\sqrt{m}$. If this is indeed a threshold and the behavior is the same as in the 1100 and 6061 alloys, then there should be no effect of the mercury at ΔK levels below about 3.5 MPa$\sqrt{m}$. Extrapolating the air data to this level, the crack growth rate is on the order of 10^{-10} m/cycle, or on the order of atomic spacings per cycle. A crack growth rate this slow was not measured in the air tests for this alloy.

The results for the static fatigue tests show that for this alloy, there is no difference in steady state crack velocity regardless of the controlling condition. There is, though, a difference in the apparent threshold of crack growth with controlling conditions. Little or no crack growth was evident until the applied K reached approximately 4 MPa$\sqrt{m}$ under load control conditions. In the displacement control test no crack growth was apparent below about 2 MPa$\sqrt{m}$. In the steady state region of crack growth, totally unlike either previous alloy discussed, the crack velocity under displacement and load control conditions was approximately the same, about 8 cm/s.

In examining the fractographic features on the surfaces created under the different loading conditions (Figures 4.9a through f) the same basic observations that were made for the other alloys can also be made for 7075. In air under cyclic fatigue conditions (Figure 4.9a) the fracture surface is highlighted by a rugged topography of ridges. The ridges, as in the air generated surfaces for the other alloys, are perpendicular to the direction of crack growth and generally indicate a rather ductile fracture mode. The surface created under cyclic fatigue conditions in the mercury environment

(Figure 4.9b) is smoother than that which was produced in air. There is also some evidence of fine, secondary intergranular cracks. The fracture mode is predominantly intergranular. The fracture surfaces created under load and displacement control static fatigue conditions are shown in Figures 4.9c and 4.9d respectively. The appearance is not a function of loading condition. The surfaces are not unlike those which occurred under cyclic fatigue conditions in mercury, predominantly intergranular with some evidence of secondary cracking. There is some indication of transgranular cleavage type fracture. This can be seen by the river patterns in the large grain in the center of Figure 4.9c. Unlike the other two alloys tested, there is no apparent relationship between the insoluble particles and the fracture appearance.

The mixed mode nature of crack growth in mercury embrittled 7075-T651 is further shown in Figure 4.9e. This polished and etched transverse section indicates that the fracture surface follows the outline of the microstructure in some places, and through the grains in others. There is secondary cracking along the grain boundaries as well. Closer examination of the surface (Figure 4.9f) suggests a brittle fracture mode. There is no indication of plastic deformation on any of the grains which intersect the fracture surface.

Figure 4.9a. Fracture appearance in air under cyclic fatigue conditions for 7075-T651, $\Delta K \sim 15$ MPa$\sqrt{m}$, 5 Hz or 30 Hz. Crack growth in the LS plane, ductile transgranular fracture.

Figure 4.9b. Fracture appearance in mercury under cyclic fatigue conditions for 7075-T651, $\Delta K \gtrsim 3$ MPa$\sqrt{m}$, 5 Hz or 30 Hz. Crack growth in the LS plane. The fracture path is intergranular.

50 µm

Figure 4.9c. Fracture appearance in mercury under load control static fatigue conditions. K > ~ 4 MPa$\sqrt{m}$. Crack growth in the LS plane, with mixed transgranular and intergranular fracture.

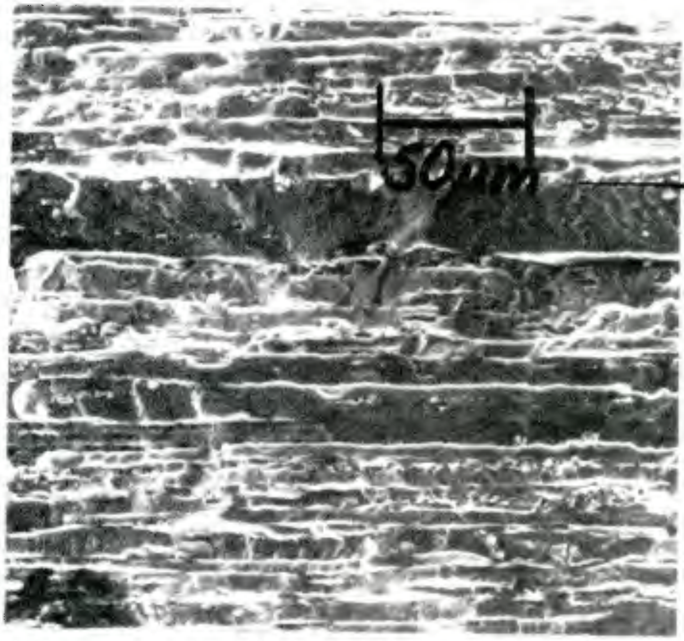

50 µm

Figure 4.9d. Fracture appearance in mercury under displacement control static fatigue conditions. K > ~ 2 MPa$\sqrt{m}$. Crack growth in the LS plane. The fracture is mixed mode, transgranular, and intergranular.

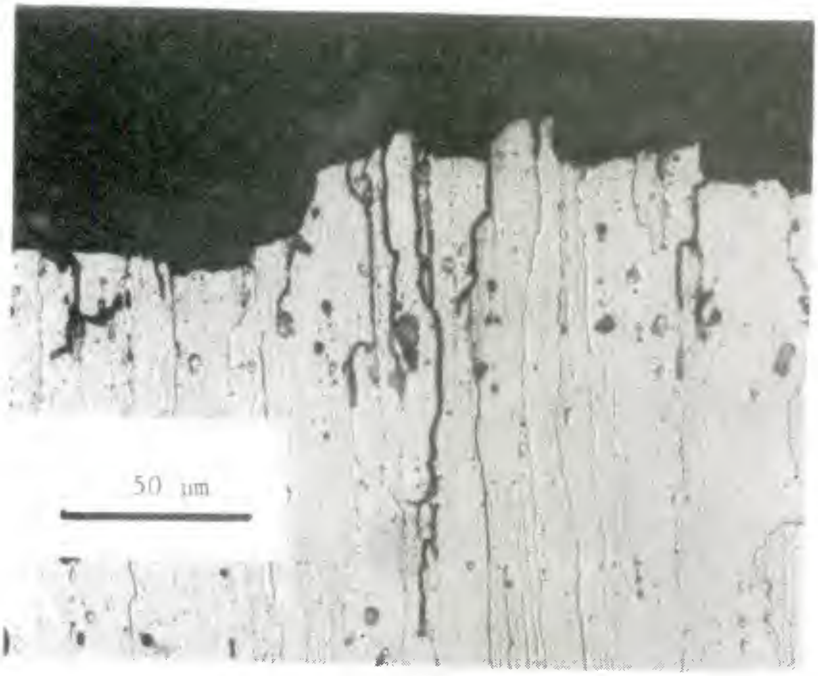

Figure 4.9e. Transverse section (LT plane) of 7075-T651, Keller's reagent, displacement control static fatigue specimen. K = 3 MPa$\sqrt{m}$, showing both intergranular and transgranular fracture.

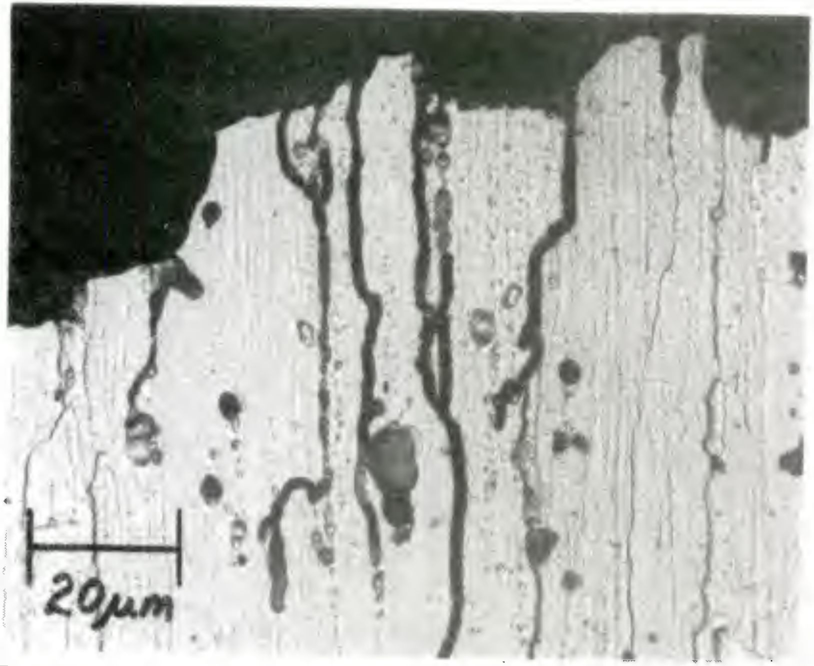

Figure 4.9f. Higher magnification of Figure 4.9e indicating brittle fracture mode.

4.2 The Effects of Temperature on Crack Growth Behavior for the Mg-Si Aluminum Alloy 6061-T651

4.2.1 Static Fatigue

Static fatigue tests under both controlling conditions were conducted in the 6061-T651 alloy at -25°C, 0°C, +25°C, and +45°C. The results at +25°C are reported in Section 4.1. The crack growth rate behavior at all the temperatures tested is plotted in Figure 4.10. There are several general comments which can be made about these results. At all temperatures, there is a distinct difference between the steady state crack growth behavior under load control and displacement control conditions. Under load control, the crack velocity is on the order of centimeters per second, while in displacement control, the crack velocity is on the order of only mm/s. In general, as the temperature decreases, the apparent threshold of crack growth decreases. At +45°C the threshold is approximately 12.5 $\text{MPa}\sqrt{\text{m}}$, at +25°C the threshold is approximately 8 $\text{MPa}\sqrt{\text{m}}$, and at 0°C and -25°C, the thresholds are approximately 7 $\text{MPa}\sqrt{\text{m}}$ and 4 $\text{MPa}\sqrt{\text{m}}$ respectively. The third and most interesting observation is that as the temperature decreases, the steady state crack velocity increases.

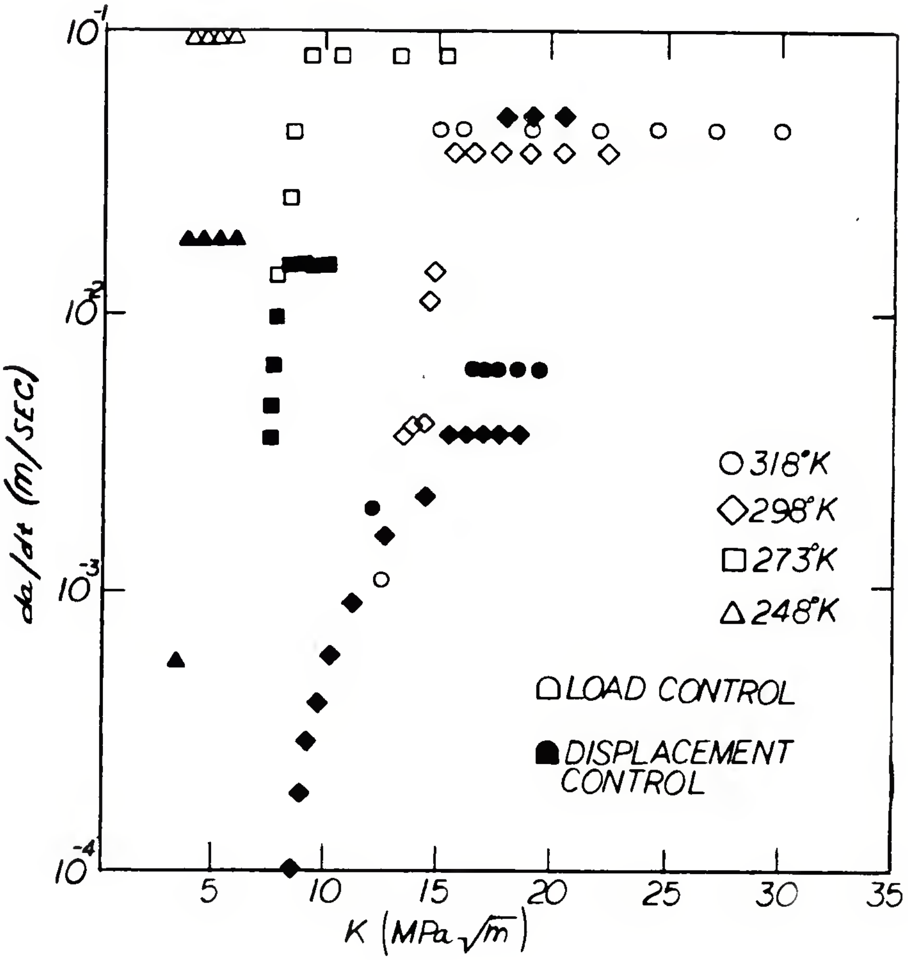

Figure 4.10. Static fatigue results for 6061-T651 at various temperatures.

The fracture surfaces created at the various temperatures are shown in Figures 4.11a through d. As above, the fracture appearance is the same regardless of the controlling condition. At 45°C (318°K), Figure 4.11a, the surface has areas of both smooth and rugged features. The smooth areas indicate a brittle intergranular fracture mode. The rugged areas are probably more ductile intergranular fracture with ridges that are approximately perpendicular to the direction of crack growth. There is some indication of secondary, intergranular fracture, but not as much as was observed above (see for example Figures 4.3e and 4.3f). There seems to be no relationship between the fracture appearance and the insoluble particles.

Figure 4.11b is the same as Figure 4.6b, and is discussed above. The most important features of the surface are a predominantly intergranular crack path with some evidence of secondary intergranular cracking. The surface topography is one of some dimples and ridges which are parallel to the direction of primary crack growth. The ridges may be related to the insoluble particles.

The surface created under static fatigue at 0°C (273°K) is shown in Figure 4.11c. In this figure, there is some evidence of transgranular fracture as indicated by the apparently cleaved grain in the center of the picture (note the river patterns). There is some suggestion of secondary intergranular cracking as well. The smooth areas of Figures 4.11a and 4.11b are also present, but the surface also has a small area which is covered with small elongated dimples. These dimples are similar to those seen in the 1100-0 static fatigue surfaces, and there are ridges parallel to the direction of primary crack growth. It is not clear whether these ridges have any relation to the insoluble particles.

Figure 4.11a. Fracture appearance in mercury at 45°C (318°K) under static fatigue conditions for 6061-T651. K > ~ 16 MPa$\sqrt{m}$. Crack growth in the LS plane, following an intergranular path.

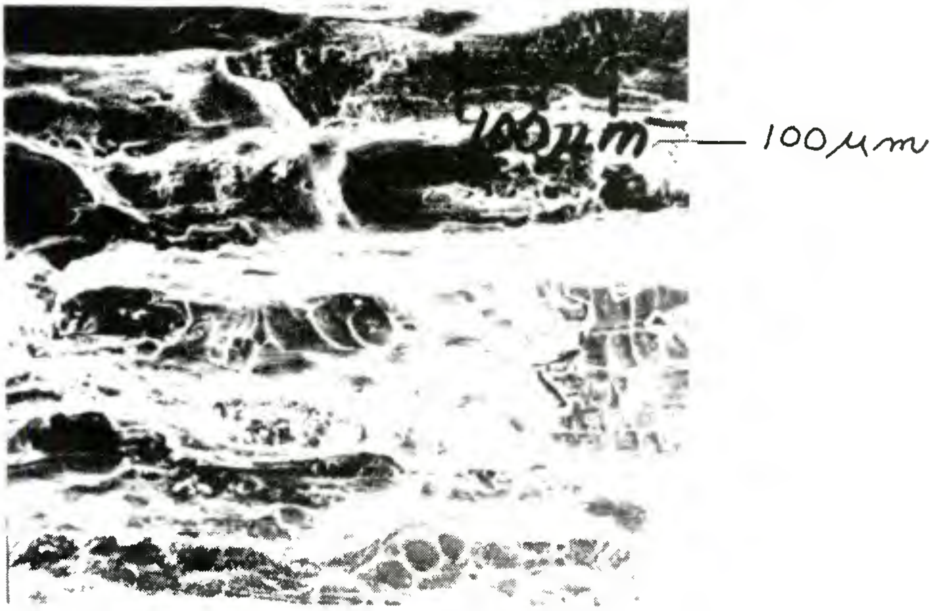

Figure 4.11b. Fracture appearance in mercury at 25°C (298°K) under static fatigue conditions for 6061-T651. K > ~ 14 MPa$\sqrt{m}$. Crack growth in LS plane. The fracture is predominantly intergranular.

Figure 4.11c. Fracture appearance at 0°C (273°K) under static fatigue conditions for 6061-T651. K > ~ 10 MPa$\sqrt{m}$. Crack growth in the LS plane, following a mixed intergranular and transgranular path.

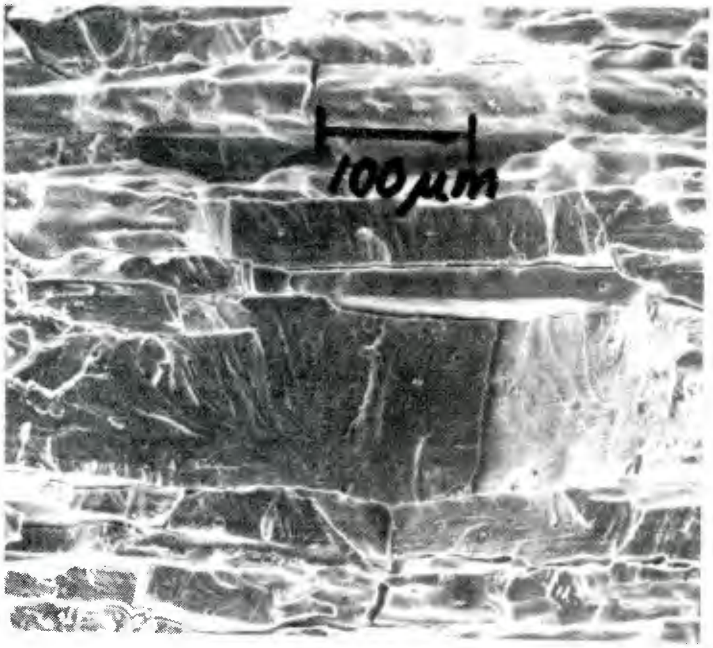

Figure 4.11d. Fracture appearance at -25°C (248°K) under static fatigue conditions for 6061-T651. K > ~ 5 MPa$\sqrt{m}$. Crack growth in the LS plane, in a mixed transgranular and intergranular mode.

At −25°C (248°K), the fracture surface (Figure 4.11d) shows a somewhat greater amount of cleaved grains than those fracture surfaces created at higher temperatures. In the cleaved grains, there are some dimples which could be related to the insoluble particles. Again, there is some intergranular secondary cracking. There is some of the smooth, apparently intergranular fracture, but there is no indication of small elongated dimples.

4.2.2 Cyclic Fatigue

Cyclic fatigue tests were conducted at +25°C, 0°C, and −25°C for 6061-T651 at 5 Hz. In reporting these data, one might plot the actually measured crack growth rate versus ΔK, which appears in Figures 4.1, 4.4, and 4.7. A better way of presenting the data is that proposed by Pao et al.[62] Environmentally assisted crack growth can be considered as having two components, an inert environment component, given by the Paris power law, and an aggressive environment component. To study the effects of temperature, one needs only to analyze the second component of fatigue crack growth. The environmental component cannot be measured directly, but is easily calculated from the measured crack growth rates by:

$$\frac{da}{dN}\Big)_{\text{environment}} = \frac{da}{dN}\Big)_{\text{measured}} - A\Delta K^{m} \qquad (4.1)$$

The environmental component of the embrittled crack growth was calculated using Eq. (4.1) and is plotted in Figure 4.12. By using this approach, it is apparent that the environmental component of fatigue crack growth follows a linear relationship between log da/dN and log ΔK. The slopes of the straight lines increase with decreasing temerature. Not apparent in the plot, but observed with statistical analysis,[67] is that the intercepts of all the straight lines are about the same.

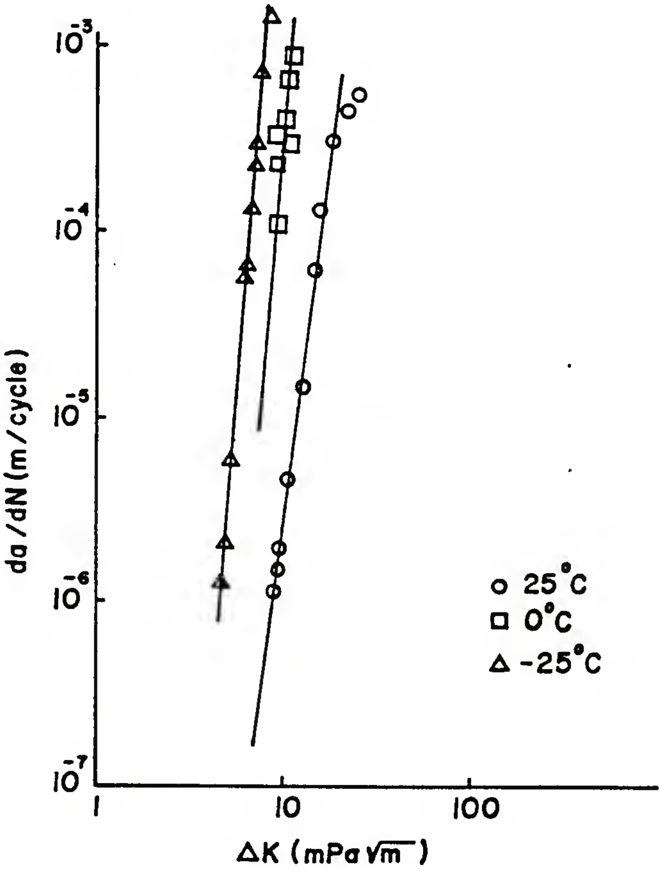

Figure 4.12. Environmental component of cyclic fatigue crack growth at various temperatures for 6061-T651. Loading frequency = 5 Hz, R = 0.1, waveform = sinusoidal.

The fractography of the surfaces created at the various temperatures under the cyclic fatigue conditions is shown in Figures 4.13a through c. At +25°C, Figure 4.13a is the same surface as shown in Figure 4.6b. The features of this surface were discussed above. Shown in Figure 4.13b is the fracture surface created at 0°C. This surface shows the smooth intergranular fracture mode which has been observed on several of the other fracture surfaces above. There is an amount of secondary intergranular penetration also, but the surface is predominantly what appears to be cleavage type transgranular fracture. In addition to the cleavage river patterns, there are holes or dimples which are probably related to the larger insoluble particles.

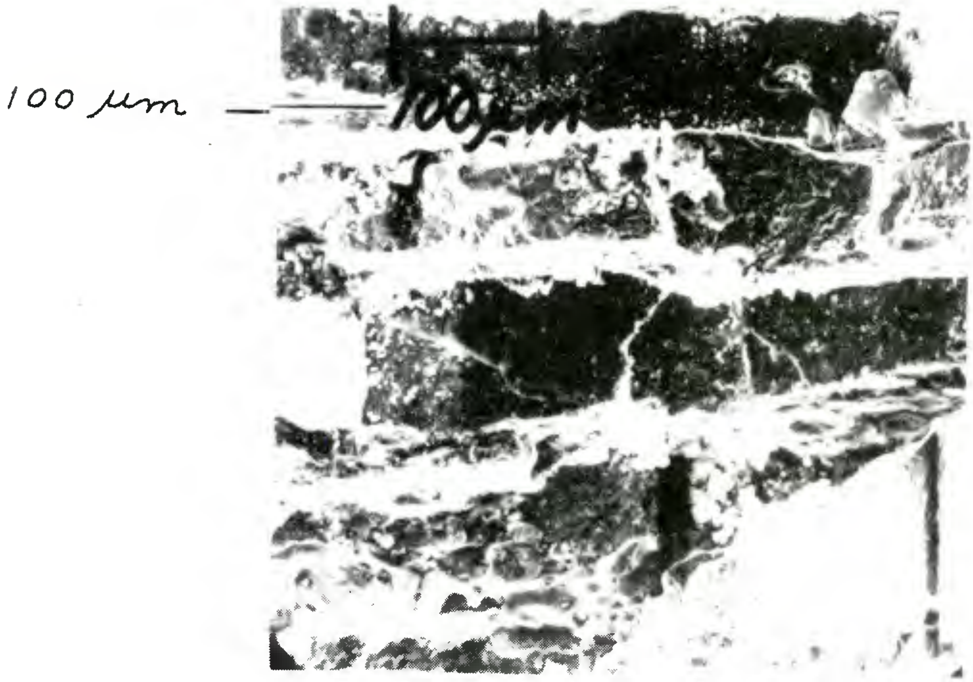

Figure 4.13a. Fracture surface of 6061-T651 at +25°C under cyclic fatigue conditions in mercury. $\Delta K > \sim 8$ MPa$\sqrt{m}$, frequency was 5 Hz. Crack growth in the LS plane, by an intergranular mode.

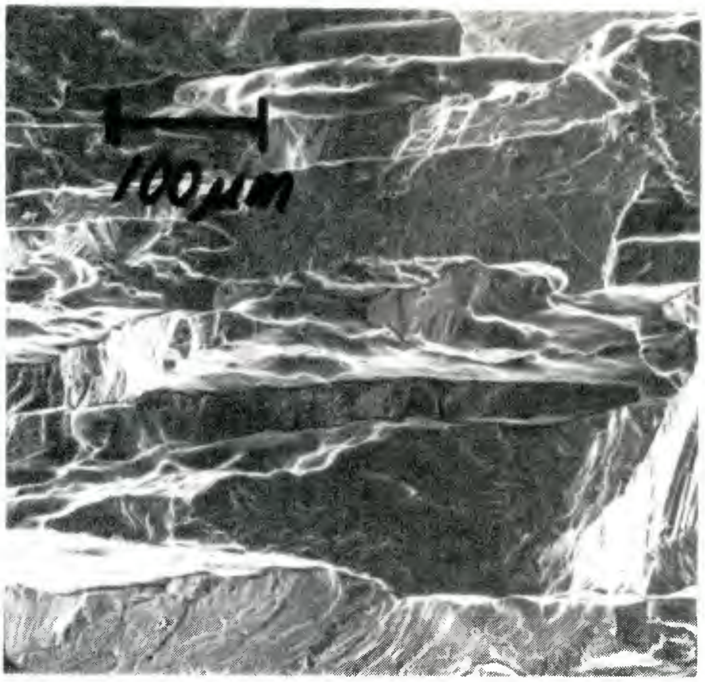

Figure 4.13b. Fracture appearance of 6061-T651 at 0°C under cyclic fatigue conditions in mercury. ΔK > ~ 9 MPa$\sqrt{m}$, frequency was 5 Hz. Crack growth in the LS plane, showing a mixed intergranular and transgranular fracture path.

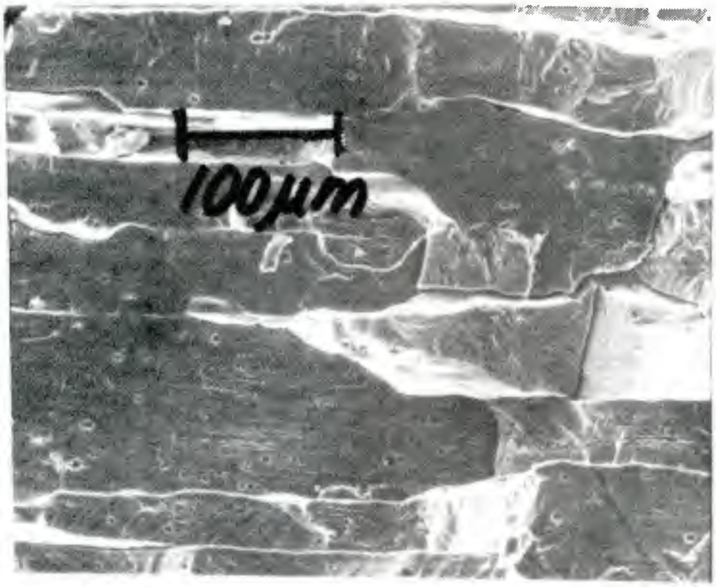

Figure 4.13c. Fracture surface of 6061-T651 under cyclic fatigue conditions at -25°C. ΔK > ~ 6 MPa$\sqrt{m}$, frequency was 5 Hz. Crack growth in the LS plane. The fracture path is predominantly intergranular.

Similar fracture appearance is shown in Figure 4.13c, which is from a surface created at -25°C. There is some intergranular penetration, but as with Figure 4.13b, this is not the dominant feature of the surface. There is some smooth intergranular fracture, but significantly less than that seen in Figure 4.13b. The dominant feature of this surface is the flat cleavage like fracture which is spotted with the holes or dimples associated with the insoluble particles.

5. ANALYSIS AND DISCUSSION

The data obtained herein can be discussed with respect to two of the main areas of previous work in the LME literature: metallurgical and experimental effects, and mechanisms. It is difficult to absolutely separate those parts of the experimental results that relate specifically to one area or another. There would be some overlapping in this section if it were broken up into two subsections. Although strict organization of this section is sacrificed, we will attempt to discuss first, the metallurgical and experimental effects, then possible mechanisms.

The primary metallurgical variable studied in the report is strength or toughness. There are two other metallurgical variables which may have influenced the results. These factors are grain size and the insoluble particles. Considering first the static fatigue results at 25°C, there are basically two quantitative measures of embrittlement obtained from the results. First is the apparent threshold K value for crack growth; the other is the magnitude of the crack velocity in the steady state region. Given in Table 5.1 are: the threshold K values (K_{ILME}, the term used by Speidel[48] in defining this property), K_{Ic} values, 0.1 percent offset yield strength values, steady state crack velocity under load control coditions v_{LC}, the approximate grain size in the plane of crack growth (the LS plane) along the L direction (the direction of crack growth) d_{LS-L}, a qualitative measure of the degree of influence of the insoluble particles on fracture appearance, and the fracture mode of cracking in mercury.

From Table 5.1, some observations can be made. The air results indicate that as strength increases, toughness decreases. This fact is well known. Interestingly there is no such relationship between strength and the degree of embrittlement as measured by K_{ILME} values. Referring to the columns showing the values K_{ILME} and K_{Ic}, it is apparent that 7075-T651 is embrittled the most, 6061-T651 the least, and the 1100-0 results fall in between. This means that a medium strength material is embrittled less than both a higher and a lower strength material. The fact that 6061 is embrittled the least, and is the intermediate strength material, enables us to propose no correlation between strength or toughness and the degree of embrittlement measured by K_{ILME}.

TABLE 5.1. RELATIONSHIP BETWEEN METALLURGICAL VARIABLES AND MEASURED DATA AT 25°C

Alloy	$.1\%\sigma_{ys}$ (MPa)	K_{Ic} ($MPa\sqrt{m}$)	K_{ILME} ($MPa\sqrt{m}$)	v_{LC} (cm/s)	d_{LS-S} (mm)	Influence of Particles	Fracture Mode in Mercury		
							C.F.	δ-S.F.	P-S.F.
1100-0	22.7	45.5	8	1-4	.6	Large	I.G.	D-I.G.	I.G.
6061-T651	282.0	31.5	9	5	.8	Some	I.G.	I.G.	I.G.
7075-T651	517.1	30.5	2	9	1.	Some	I.G.	M.M.	M.M.

Legend: C.F.= Cyclic fatigue; δ-S.F.= Displacement control static fatigue;
P-S.F.= Load control static fatigue; I.G.= Intergranular; D-I.G.= Dimpled intergranular;
M.M.= Mixed mode

There is, however, a correlation between strength and crack velocity. As strength increases, the crack velocity increases. Also, as the approximate grain size increases, the crack velocity increases. Between these two correlations, the grain size relationship would be expected. At 25°C the crack path under static fatigue conditions was predominantly intergranular for all the alloys tested. The smaller the grain size, the greater the distance the crack must grow when it follows an intergranular crack path, for a given macroscopically measured crack length. Extending this qualitative observation to a mathematical relationship between the two measured quantities indicates that crack velocity is relatively insensitive to grain size. For example, as grain size increased about 65 percent (from .6 mm to 1 mm, for 1100 and 7075, respectively), the crack velocity increased by nearly an order of magnitude. It is difficult to explain why crack velocity should be that sensitive to grain size. This leads one to believe that grain size does not govern the relative change in crack velocity magnitude observed in these experiments. There may indeed be an effect of grain size on crack velocity, as indicated by the data, but further experimentation on various grain sizes in the same alloy would be needed to determine the magnitude of such an effect.

The more interesting correlation is between yield strength and crack velocity. Using the minimum value of crack velocity for 1100-0 in Table 5.1 as a reference, the following calculations can be made. Comparing these measurements with the 6061-T651 results, the yield strength is increased by about a factor of ten, which results in an increase in crack velocity of about five. Furthermore, comparing the 1100-0 and the 7075-T651 results, the yield strength increases by a factor of about 20, with a corresponding increase in crack velocity of about a factor of 10. This means that crack velocity increases about one half as fast as the yield strength increases. This gives an indication that one important factor that governs the magnitude of crack velocity is yield strength.

Examining the yield strength correlation in terms of the mechanics at the crack tip, provides a mechanistic justification for a yield strength effect on crack velocity. Consider a crack which is initially very sharp. Upon loading, the material in the fracture process zone is subjected to a very high stress. If the stresses are sufficient to cause plastic deformation, the crack will be blunted, say to a radius ρ. With the crack having an initial length a, the stress at the crack tip was solved by Inglis[63] as:

$$\sigma = k \left(\frac{a}{\rho}\right)^{1/2} \tag{5.1}$$

where k is a constant. From Eq. (5.1), it is apparent that the crack tip stress is decreased by blunting, or by increasing ρ. Let us assume that the higher the crack tip stress, the easier it would be for embrittlement to occur. Then the less blunting there is, the more readily LME should occur. Since the extent of blunting decreases with increasing strength,[19] the stresses at the crack tip in a high yield strength material would always be greater than the stresses at the crack tip in a low yield strength material, all other factors being constant. From a totally mechanical viewpoint, therefore, it is quite reasonable to expect that the greater the yield strength, the greater the crack velocity. This agrees qualitatively with the observed data.

The influence of the insoluble particles is difficult to relate to the measured quantities. The alloy which showed the greatest apparent amount of influence of the insoluble particles on fractography was 1100-0; see Figures 4.3a through f. The only oddity in Table 5.1 that could be related to the particle influence is the large scatter in crack velocity for 1100-0 (1-4 cm/s). But since there is a trend to the scatter, such a correlation seems unlikely. The crack velocity is higher at low K values and lower at high K values, and the particle influence is the same regardless of loading condition. The relatively large effect of particles on 1100-0 is probably related to the strength of this alloy. Since particles, such as those in the alloys studied are natural stress risers, they are normally the sites of enhanced plastic deformation. Therefore, the relationship between particles and fracture appearance would be expected to be the greatest with the lowest yield strength material.

The difference in fractography of the 1100-0 alloy under the different controlling conditions in static fatigue is interesting. In the load control and displacement control tests, virtually the same crack velocity vs. K plots is observed (see Figure 4.2), but the fracture appearance is markedly different between the two cases. The displacement control test shows a brittle, predominantly intergranular fracture mode, Figures 4.3e and 4.3f. The fracture surface under load control conditons, Figures 4.3c and 4.3d, is also intergranular, but dimpled. This indicates substantially more plasticity under the load control conditions, especially around the insoluble particles. The primary difference between these two controlling conditions is the strain rate in the fracture process zone, as will be shown by the following derivation.

Equation (2.6) shows that the stresses at the crack tip are directly related to the applied K. Since strain and stress are linearly related, assuming elastic behavior, the strain is also directly related to the applied K. Since K is the variable changed in the static fatigue tests, it is interesting to examine how the time rate of change of K (dK/dt) and thus, the strain rate $\dot{\varepsilon}$, varies with the controlling conditions. From Section 2.2 and Appendix A, it is shown that K is a function of just three variables: the crack length a, the applied load P, and the specimen geometry. Only the first two variables, a and P, will be considered as contributing to the strain rate, since the same specimen geometry was used for both test conditions. Therefore, stated in general mathematical terms, K can be written as:

$$K = K(a,P) \tag{5.2}$$

Using the chain rule, and the realization that $\dot{\varepsilon}$ and dK/dt are linearly related:

$$\dot{\varepsilon} \; \alpha \; \frac{dK}{dt} = \left.\frac{\partial K}{\partial a}\right)_P \frac{da}{dt} + \left.\frac{\partial K}{\partial P}\right)_a \frac{dP}{dt} \tag{5.3}$$

With this equation we are able to make a qualitative comparison between the two controlling conditions. All of the factors on the right-hand side of Eq. (5.3) are either fixed by the specimen ($(\partial K/\partial a)_P$, $\partial K/\partial P)_a$), controlled in the experiment (dP/dt), or measured (da/dt). Consider first the specimen controlled properties. For most fracture mechanics specimens including those used in this study, at fixed load, an increase in the crack length increases

K, thus $\partial K/\partial a)_P$ is always positive. Similarly, at a constant crack length, as P increases, K also increases, or as P decreases, K decreases. The quantity $\partial K/\partial P)_a$ is also always positive.

Now we can determine the relative differences between the controlling conditions. In a load control test, dP/dt is zero. The strain rate under these conditions is:

$$\dot{\varepsilon}(\text{load control}) \;\alpha\; \frac{dK}{dt} = \frac{\partial K}{\partial a}\Big)_P \frac{da}{dt} + 0 \qquad (5.4)$$

Under displacement control conditions, when crack growth occurs before maximum displacement is attained, $dP/dt)_a$ is a positive quantity. The strain rate becomes:

$$\dot{\varepsilon}\left|\begin{array}{l}\text{displacement control, crack}\\ \text{growth before max displacement;}\\ \text{K increases}\end{array}\right| \;\alpha\; \frac{dK}{dt} = \frac{\partial K}{\partial a}\Big)_P \frac{da}{dt} + \begin{array}{l}\text{a positive}\\ \text{quantity}\end{array} \qquad (5.5)$$

After maximum displacement, the displacement is held constant. Crack growth requires that the load be decreased under these conditions. Thus the value of dP/dt is consequently a negative number, and the strain rate is given as:

$$\dot{\varepsilon}\;(\text{fixed displacement}) \;\alpha\; \frac{dK}{dt} = \frac{\partial K}{\partial a}\Big)_P \frac{da}{dt} + \text{a negative quantity} \qquad (5.6)$$

It is apparent from all these equations that $\dot{\varepsilon}$ is not a constant in any of the tests reported here. It varies with crack length because of both quantity $\partial K/\partial a)_P$, and controlling condition. Using Eqs. (5.4), (5.5), and (5.6) with the proviso for comparison that da/dt doesn't change, and the crack length is constant, some observations can be made. Three different strain rates are applied to the fracture process zone in the static fatigue tests. The lowest strain rate occurs under displacement control conditions when K decreases, Eq. (5.6). The greatest strain rate occurs in the displacement control test when K increases, Eq. (5.5). Under load control conditions, the strain rate falls somewhere in between the two maxima sited above.

Realizing this, the fractographic features observed in the 1100-0 static fatigue tests provide an interesting result. In the displacement control test, with increasing K, and in the load control test, the same crack velocity was measured (see Figure 4.2). Using the analysis above, it is clear that the strain rate was somewhat greater in the displacement control test than in the load control test. It is well known that increasing the strain rate increases the yield strength. Therefore, it would be predicted that the load control test would result in a more ductile appearing fracture surface than the displacement control test, although this change should be very small since several orders of magnitude are normally required to cause a significant change in yield strength. This trend is observed in the fractography of the 1100-0 alloy, although it may be argued that the fractographic changes observed were greater than one might expect.

This finding indicates that the enhanced shear model of Lynch[7-10] may have been operating to some degree in the testing of 1100-0. There was no evidence of a loading condition effect on fractographic features in any other static fatigue test performed using the other materials studied. One would expect that if the reduced yield strength mechanism is the primary operating mechanism, a significant reduction in yield strength would be more apparent in the higher yield strength materials, which is not observed. A possible explanation of the anomaly follows. Suppose the presence of the liquid mercury indeed reduces the yield strength of the material in the vicinity of the fracture process zone. Yet the magnitude of this reduction is small, say for example one or two MPa. Also assume that the strength decrease is not a strong function of the inert environment yield strength. Under these assumed conditions, the small decrease in yield strength could be significant in a low yield strength material, and small for a high yield strength material. This would explain the observations made herein, and will be discussed further later in this section.

Another observed phenomenon in the static fatigue tests can be related to the yield strength. This is the hysteresis in the load control and displacement control crack velocity measurements. Referring to Figures 4.2, 4.5, and 4.8, it is shown that embrittled crack growth occurs only when K is increasing for the 1100 alloy, at an order of magnitude slower in the 6061 alloy when K is decreasing, and at the same velocity regardless of whether K is increasing or decreasing in the 7075 alloy. One might try to explain this as a strain rate effect as above since that is the primary experimental variable that changes. However, such changes in crack velocity seem too large to be the result of strain rate changes that are, at best, subtle.

A better explanation is obtained by applying Gordon's work on transport mechanisms in LME.[35] The first prerequisite for classical LME is the presence of the liquid metal at the fracture process zone. When the crack grows, the liquid must keep up with the rapidly advancing crack tip. Treating this as a fluid flow problem, Gordon[35] derived the following equation to approximate the velocity of the molten metal, v:

$$v = \frac{h^2}{8\mu a}(\Delta p + \frac{2\gamma_{LV}}{h} \cos \phi) \qquad (5.7)$$

where h is the crack surfaces separation, μ is the kinematic viscosity of the liquid, a is the crack length, Δp is the applied pressure, γ_{LV} is the liquid-vapor surface energy, and ϕ is the dihedral angle of the meniscus. Figure 5.1 is a schematic of Gordon's idealized crack tip. Equation (5.6) shows that the crack velocity of the liquid metal flowing during crack growth is a strong function of the crack surface displacement. As shown in Figure 5.1, this displacement can be approximated by the crack tip opening displacement (CTOD).

It is interesting to note that if fluid flow is the only factor controlling the rate of crack growth, cracks would grow faster in lower yield strength materials than in higher yield strength materials because of the larger CTOD associated with greater amounts of blunting. Such behavior is not observed, in fact the opposite is measured. This suggests that the magnitude of crack velocity is determined by other factors, such as strength or the rate of the actual embrittling reaction, in addition to the crack surface displacement. The importance of Eq. (5.7), therefore is to explain what occurs when the loading conditions change.

When a crack is loaded such that K is ever increasing, it is clear that the CTOD is also ever increasing. Similarly, when K decreases, the CTOD should decrease. Decreasing CTOD or h in Eq. (5.7) restricts the molten metal flow. This alone suggests a change in crack velocity based on changing loading conditions, but probably not of the scale observed in the 1100-0 and the 6061-T651 results. This scenario also predicts an effect on the 7075-T651

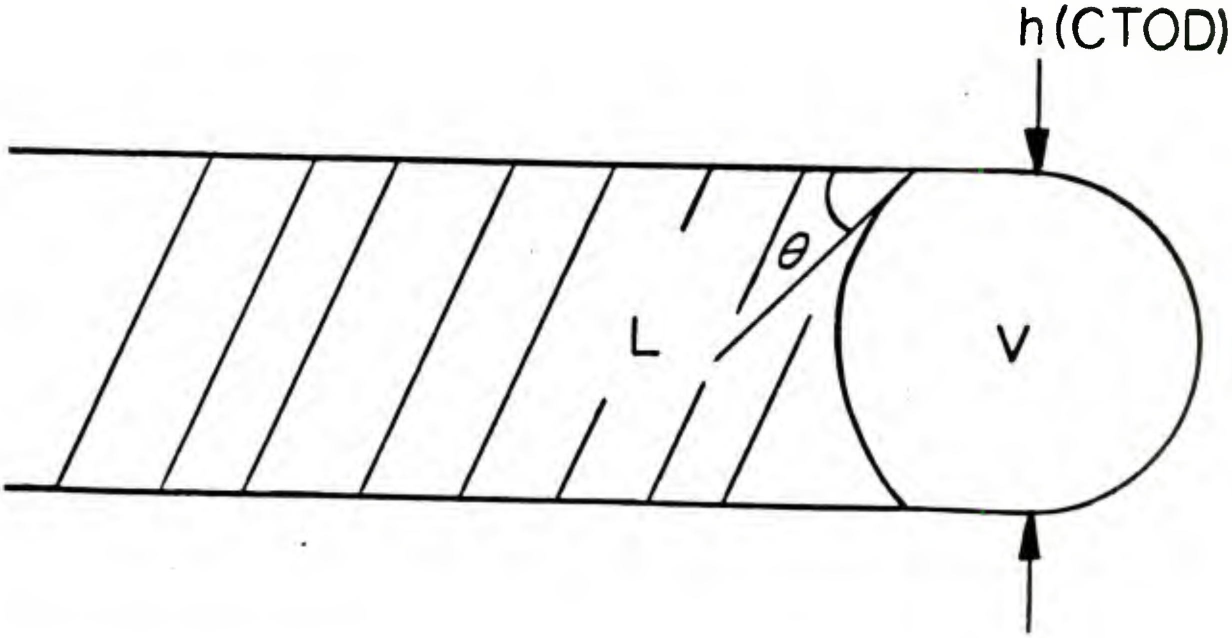

Figure 5.1. Embrittled crack tip filled with molten metal.

crack growth behavior, which is not observed. Expanding on this, let us assume that prior to a change in loading condition, we subject the crack to a relatively high K and allow a significant amount of crack growth prior to a change in loading conditions, such that K is then ever decreasing. When the crack grows under the increasing K conditions, it is safe to assume that some plastic deformation of the material in the vicinity of the crack tip occurs. After the crack tip grows beyond this point, the plastically deformed material is unloaded. It is possible that this previously deformed material contains residual stresses or strains. If the residual stresses are of sufficient magnitude, they could result in a substantial displacement of the crack surface, which is somewhat removed from the crack tip. The combination of high residual stress and low modulus material has been shown to cause actual closure of the crack surfaces in cyclic fatigue loading.[64] The same can be argued for static fatigue loading under the conditions described above. Although this has not been measured, recent theoretical predictions by Newman[65] indicate that this would be the case. Furthermore, the greater the amount of plastic deformation upon loading, the greater the amount of closure would be expected.

Returning to Eq. (5.7), it is clear that large amounts of crack surface closure could significantly reduce the rate of flow of the liquid metal. The greater the plastic deformation, the larger the relative change in crack surface displacement behind the crack tip, and thus the greater the restriction of liquid metal flow. Considering now the effect of yield strength on the fluid flow, it is clear that the lower the yield strength, the larger the change in fluid flow, and thus the crack velocity. This is observed in the experiments. For the 1100-0 case, the crack surfaces may have actually come together, totally restricting the flow of the embrittling liquid metal to the crack tip resulting in the crack arrest. In 7075-T651, crack growth may have occurred with such little plastic deformation to cause an insignificant change in the crack surface displacement, and no change in crack growth behavior. Finally, the intermediate strength alloy, 6061-T651, should fall somewhere in between.

Two other aspects of the static fatigue results warrant comment, first, the K dependence of the 1100-0 results, and second, the apparent difference of the K_{ILME} for 6061-T651 and 7075-T651 as a function of controlling condition. The 1100-0 data shows that cracks grow faster at low K than at high K values when K is ever increasing. If this is indeed true, it should be the result of some mechanical change in loading conditions, and not due to a metallurgical factor. Variations in static fatigue crack growth behavior have been observed, such as two plateaus in steady state crack growth[48] that were the result of a different rate controlling process limiting crack growth. There is little reason to expect that a different rate controlling process is operating at high K conditions, than at low K conditions in such a simple system as the 1100-0-mercury system.

A possible mechanical explanation could be the blunting argument presented above to explain the effect of yield strength on the magnitude of crack velocity. At high K values, more blunting is expected than at low K values. The greater the blunting, the lower the stress at the fracture process zone. If embrittlement occurs as a combination of stress and a solid-liquid reaction which has a finite rate of reaction, then the lower the stress, the more reaction time would be required to cause crack growth. This would result in the observed behavior. Also, such a response would be expected to be most prevalent in the lowest yield strength material. This effect could be eliminated if a larger specimen was used in the testing. Also greater constraint provided at the crack tip for the lower yield strength materials would restrict plastic flow and blunting. Caution should therefore be exercised in drawing definitive conclusions regarding the results obtained on low yield strength materials using small specimens.

The disagreement between K_{ILME} values as a function of loading condition is more difficult to address. This behavior has been observed many times in the past in other embrittlement studies, and a viable explanation has not yet been presented. Those who have studied this effect have been unable to develop a standard method of measuring threshold K values for use in design.[66] It can readily be seen that in using fracture mechanics specimens in load control, if the initial loading is too fast, slow crack growth may not be measured. On the other hand, the displacement control loading conditions have been used primarily for long term, slow crack growth tests.[66] The results obtained here were exactly the same as those in reference 66, namely higher K_{ILME} values for load control tests, and lower values for displacement control tests. Further discussion of this point would revolve around fracture mechanics specimen and test design philosophy, which are beyond the scope of this report. Thus, we will end the discussion of the static fatigue results stating that the discrepancy between the load control and displacement control K_{ILME} values is the consequence of a shortcoming of fracture mechanics testing techniques.

The results of the cyclic fatigue tests, Figures 4.1, 4.4, and 4.7 follow. The air results show that all three alloys tested follow the Paris power law.[40] The 7075-T651 alloy has the least tolerance to fatigue loading, 1100-0 the most, and the 6061-T651 falls somewhere in between. This is shown by the slopes of the log da/dN versus log ΔK plots. These values were 3.75, 4.5, and 5.6 for the 1100, 6061, and 7075 alloys respectively. Furthermore, the air environment may be considered as relatively inert, since the data for both loading frquencies tested fell on the same line for each of the alloys.

In mercury, below some critical value of ΔK, there seems to have been no effect on crack growth rate when compared to the air results for both 1100 and 6061. There was however, a threshold of embrittled crack growth. In 7075-T651 there was an indication of a threshold phenomenon, but the ΔK value at which this would occur corresponds to a cyclic fatigue crack growth rate on the order of 10^{-10} m/cycle in air. Crack growth rates of this magnitude were not measured in this study, and may even be below the threshold ΔK value for crack growth in air for this alloy.[54]

Once the apparent ΔK threshold for embrittled crack growth is exceeded, the crack growth rate again follows a linear relationship with ΔK in log-log space initially for the 1100 and 6061 alloys. It is not clear that this occurs in the 7075 alloy. After the initial linear portion, there is a more gradual increase in crack growth rate with increasing ΔK. In the 1100 results, there is no indication of the crack growth rate deviating from the initial linear behavior in mercury. This is due to the weakness of the specimen chosen for the tests when applied to this low strength alloy. The uncracked ligament of the specimens made of the 1100-0 alloy simply can not support the applied loads, and collapses from gross plastic deformation. Using a much larger specimen when testing this alloy, one which could support higher ΔK values, probably would have revealed similar behavior to the other two alloy results.

The 6061-T651 and the 7075-T651 results clearly indicate a frequency effect. Cracks grow significantly faster at 5 Hz than at 30 Hz. This is not clear in the 1100-0 results, although much faster crack growth rates are measured at 5 Hz than at 30 Hz in this alloy. The frequency effect in 6061 and 7075 is quite similar to the frequency effects which have previously been observed in other embrittling systems.[47] Also, this type of behavior, including the frequency effect, has been shown by Wei and Landes[45] to be related to the static fatigue behavior.

Considering the effect of alloy or strength on the degree of embrittlement, the same ordering of the alloys found in the static fatigue results also occurs in the cyclic fatigue results. Summarizing, the lowest threshold ΔK for embrittled crack growth occurs in the 7075-T651 alloy, the highest in the 6061-T651 alloy, and the 1100-0 value is in between. There is no reason to expect that the cause for this behavior is different under cyclic fatigue conditions than static fatigue conditions. The degree of embrittlement, using thresholds of embrittled crack growth as the measure, is most probably not related to strength.

There is some correlation between strength, and the maximum crack growth rate in cyclic fatigue loading, similar to the static fatigue results. But unlike the static fatigue data, there is no steady state crack growth rate to draw comparisons. Arbitrary comparisons of the maximum observed crack growth rate can be made. These fast crack growth rates occur at 5 Hz in all the alloys, but at different ΔK values. For 1100-0, the maximum da/dN is about 3 x 10^{-5} m/cycle at ΔK of about 10 $MPa\sqrt{m}$ (Figure 4.1). In 6061-T651, the fastest crack growth rate is about 6 x 10^{-4} m/cycle at ΔK of about 25 $MPa\sqrt{m}$ (Figure 4.4). The largest da/dN for the 7075-T651 alloy is about 2 x 10^{-3} m/cycle at ΔK of about 10 $MPa\sqrt{m}$ (Figure 4.7). The ordering of the maximum crack growth rate is exactly the same as was found in the static fatigue tests. The higher the yield strength, the greater the maximum crack growth rate.

If the 1100-0 results are chosen as a standard, the following comparisons can be made. By increasing the yield strength by about an order of magnitude to the strength level of the 6061-T651 alloy, the maximum crack growth rate increased by about a factor of 20. When the yield strength is increased by about a factor of 20, the 7075 results show a crack growth rate increase of about a factor of 200. This indicates that the mechanics of crack growth under cyclic fatigue conditions may be somewhat different than under static fatigue conditions. But the effect of yield strength is in trend agreement with the static fatigue conditions.

Returning now to a discussion of the frequency effects, some observations can be made about the application of some kind of superposition model. According to Wei and Landes,[45] the cyclic fatigue crack growth rate in the aggressive environment should be related to the time at which the crack is subjected to K values which exceed K_{ILME}. Whenever K is greater than K_{ILME}, the crack should grow an increment which could be predicted by integrating the static fatigue crack velocity over the time at which K indeed exceeds K_{ILME}.

This means that the crack growth rates measured as a function of fatigue cycles (da/dN) should vary with frequency. Furthermore, the relationship between the crack growth rates should be inversely proportional to frequency. For example, in one second, if the superposition model applies, regardless of frequency, the crack should grow roughly the amount, Δa. At 30 Hz, the crack would be subjected to thirty cycles, and the crack growth rate would be $\Delta a/30$. Similarly, cycling at 5 Hz, the increment would occur in only five cycles. The crack growth rate would be $\Delta a/5$. Comparing the two estimates, it is clear that cracks should grow six times faster at 5 Hz than at 30 Hz, with all other factors being constant.

Consider the fatigue crack growth data for 6061-T651, Figure 4.4, and for 7075-T651, Figure 4.7. At ΔK of 20 $\text{MPa}\sqrt{\text{m}}$ in 6061-T651, da/dN at 30 Hz is about 2×10^{-5} m/cycle. At 5 Hz, the crack growth rate is about 4×10^{-4} m/cycle. This means that at 5 Hz, the crack grows about 20 times faster than at 30 Hz in 6061-T651. Similarly in 7075-T651, for ΔK of about 5 $\text{MPa}\sqrt{\text{m}}$, da/dN is about 10^{-5} m/cycle at 30 Hz, and about 6×10^{-4} m/cycle at 5 Hz. Therefore in this alloy, cracks grew about 60 times faster at 5 Hz than at 30 Hz. The factor of six is therefore not measured in either of the two alloys which exhibit the strong frequency effect.

Although it is apparent that the superposition model does not totally explain the cyclic fatigue results, it is interesting to compare this predictive technique with the actually observed data. The procedure involves the simple superposition of the static fatigue results, on a cycle by cycle basis, to approximate the results under cyclic fatigue conditions. This assumes that during each fatigue cycle, the crack will have an instantaneous velocity which is the same as was measured during the static fatigue tests. Stated in empirical terms, the crack growth rate is:

$$\left.\frac{da}{dN}\right)_{env} = \left.\frac{da}{dN}\right)_{air} + \frac{1}{\nu'} \left.\Delta a\right)_{one\ cycle} \tag{5.8}$$

$$\Delta a = \int_0^1 f(K(t))dt$$

Where

$\left.\frac{da}{dN}\right)_{env}$ = the crack growth rate in mercury.

$\left.\frac{da}{dN}\right)_{air}$ = the crack growth rate measured in air.

Δa = that increment of crack growth that would occur if the da/dt data is integrated as a function of K assuming a loading frequency of one Hz.

$f(K)$ = the crack velocity measured as a function of K in the static K tests.

$K(t)$ = the sinusoidal variation in applied K during the static fatigue tests: $K(t) = K_{mean} + \Delta K/2 \sin 2\pi t$.

K_{mean} = mean K value during the cyclic fatigue tests.

ΔK = the range in K during the cyclic fatigue tests.

To make the calculation easier, the static fatigue results are idealized as shown in Figures 5.2, 5.4, and 5.6 for the 1100, 6061, and 7075 alloys respectively. The integration is performed numerically for various values of ΔK for each alloy using Simpson's rule.[67] The results of the superposition calculations are plotted in Figures 5.3, 5.5, and 5.7 for 1100, 6061, and 7075 respectively, and compared to the actual recorded data in these same figures.

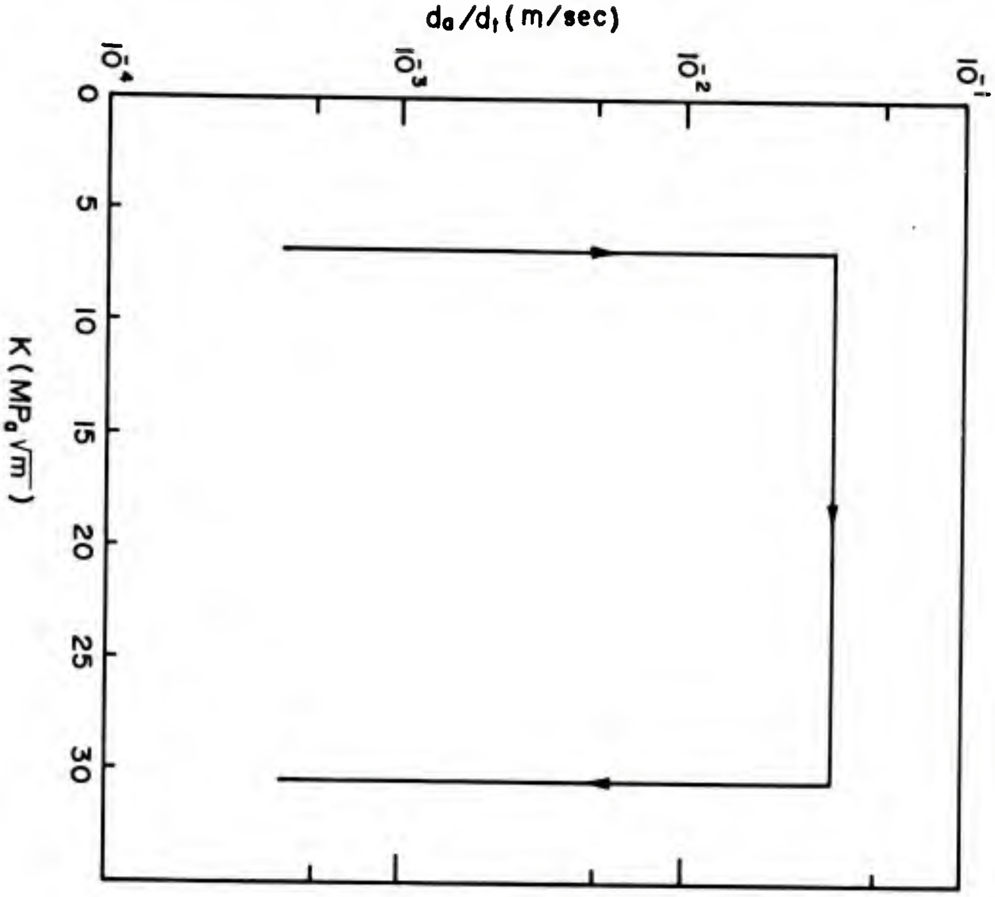

Figure 5.2. Idealized crack growth for 1100-0.

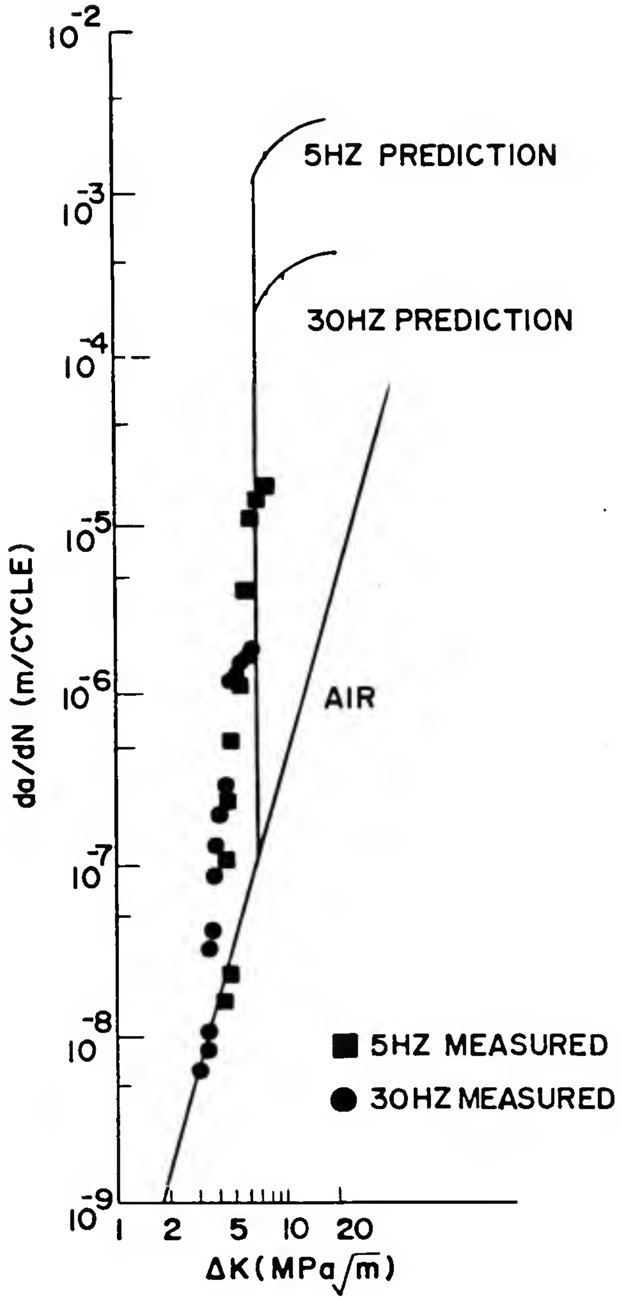

Figure 5.3. Superposition prediction for 1100-0.

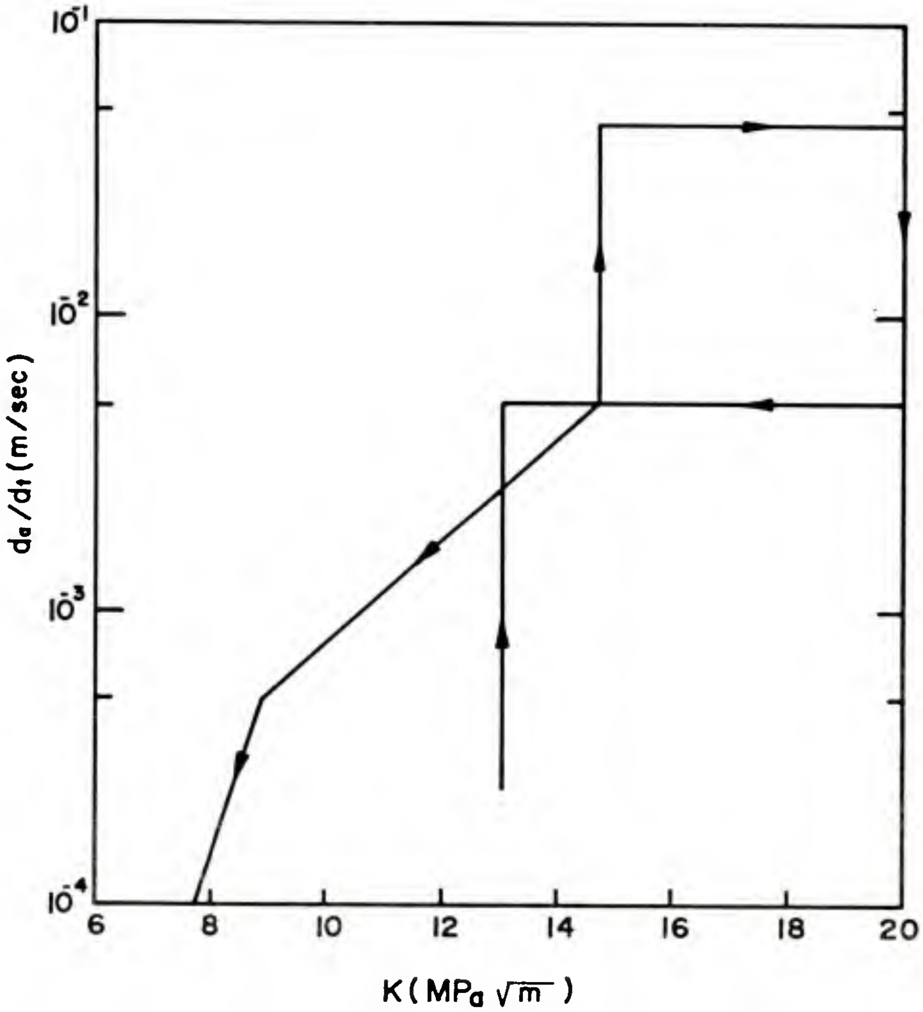

Figure 5.4. Idealized crack growth behavior for 6061-T651.

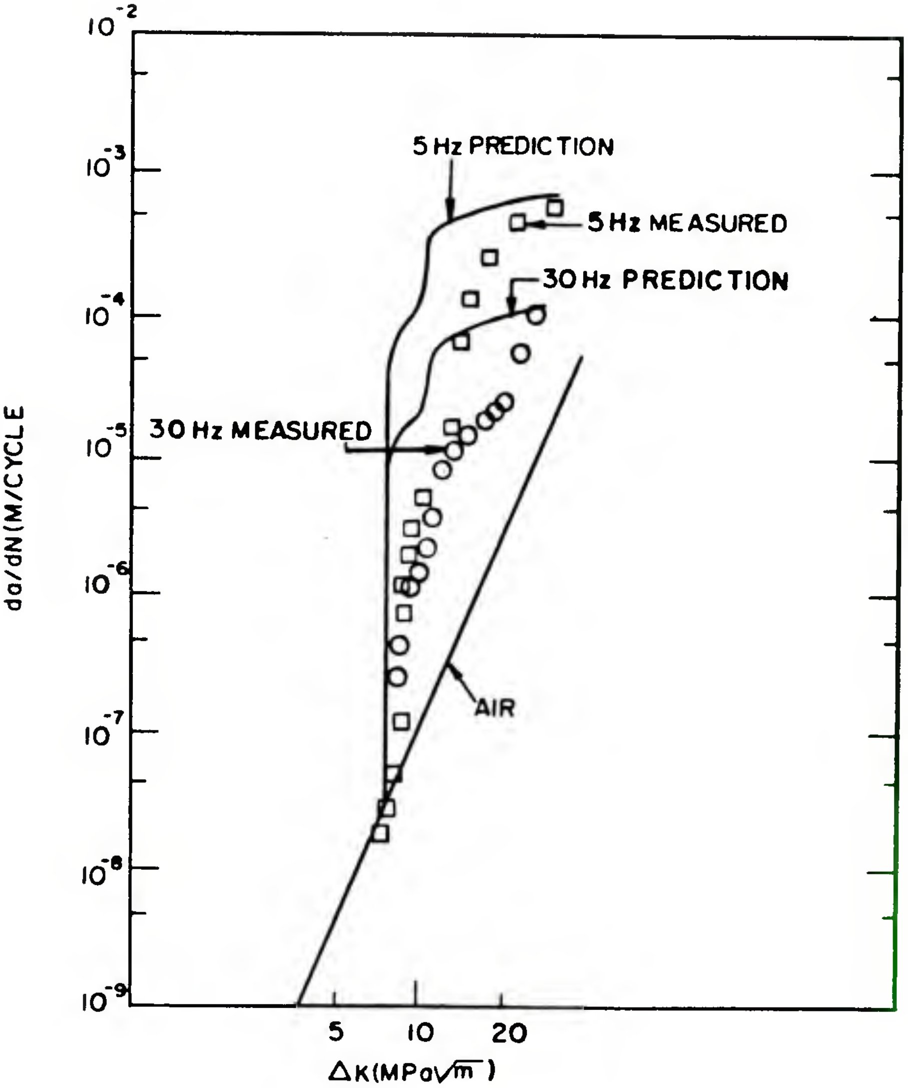

Figure 5.5. Superposition prediction for 6061-T651.

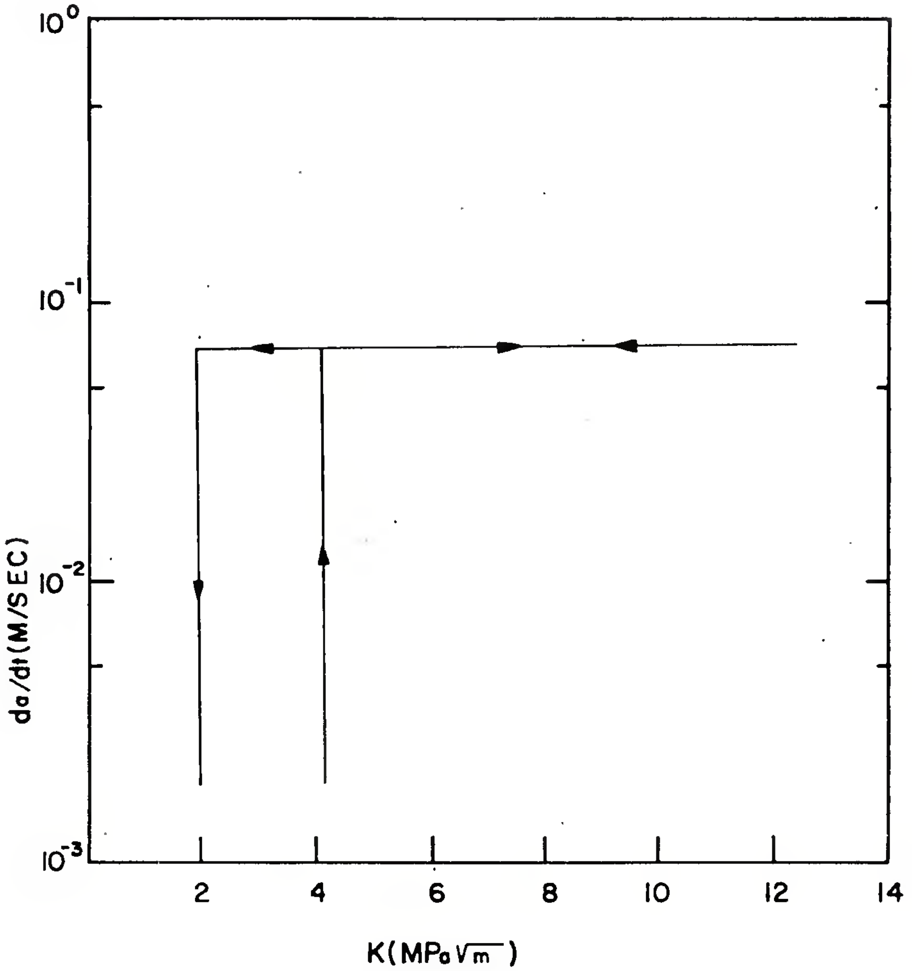

Figure 5.6 Idealized crack growth behavior for 7075-T651.

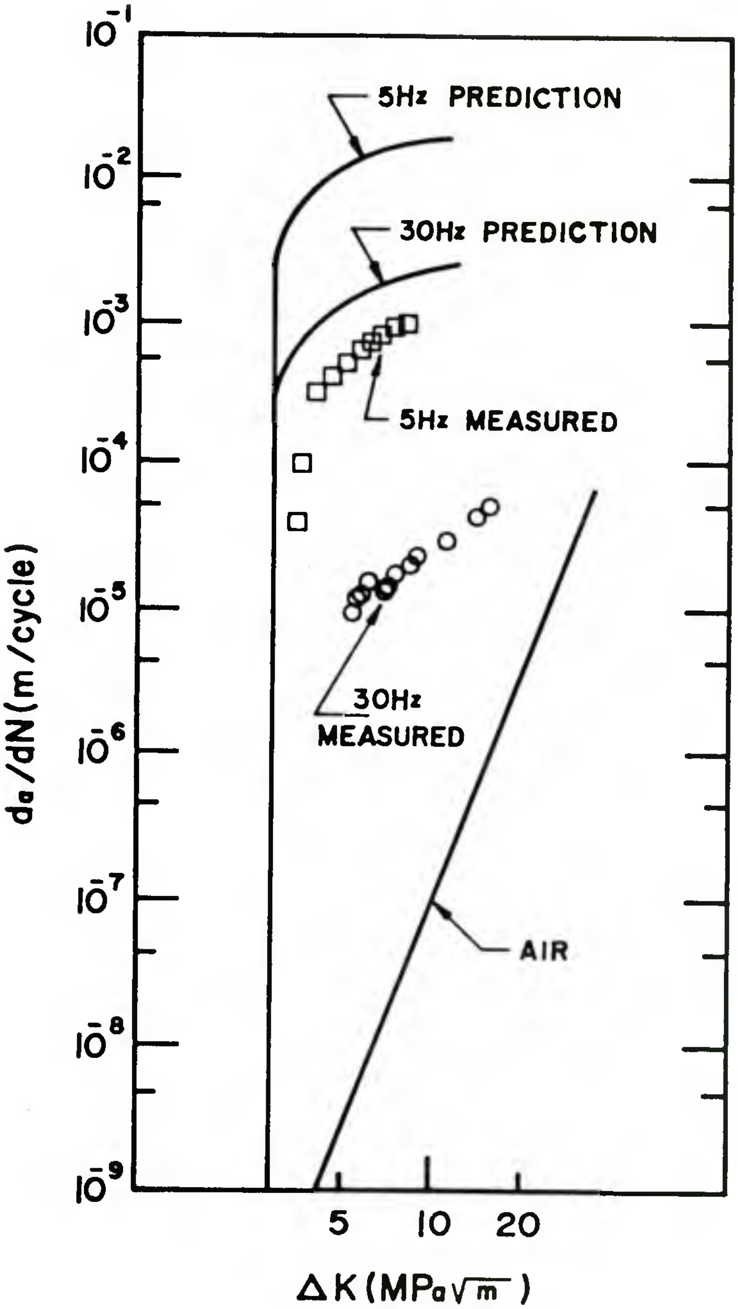

Figure 5.7. Superposition prediction for 7075-T651.

The comparison of the predicted crack growth rates in mercury and the actually measured crack growth rates in the various alloys does not yield very good agreement. In all cases, the general shape of the predicted curve is as observed. The predictions suggest a large increase in crack growth rate with a small increase in ΔK followed by a region of much more gradual increase in da/dN with increasing ΔK. The superposition gives a reasonable estimate of the apparent threshold in embrittled crack growth under cyclic fatigue conditions. Beyond this, the predictions are not very good.

The apparent inadequacy of the superposition model has been observed previously. The lack of agreement had been attributed to the fact that at high frequency, it is possible that the unembrittled crack growth can become competitive with the embrittled crack growth.[62] This observation is supported by fractographic evidence which indicated decreased embrittlement with increased frequency. In our study, no change in fractography with frequency was observed. The fracture surface at 5 Hz was exactly the same as at 30 Hz. Furthermore, the fractographic features in cyclic fatigue are similar to the fracture surface topography observed under static fatigue conditions (compare for example, Figures 4.5b and 4.5c). Probably the most conclusive argument against nonembrittled crack growth becoming competitive with embrittled crack growth is the magnitude of the differences between the crack growth rates in mercury and air. In both the 6061-T651 and 7075-T651 results, the embrittled crack was growing by as much as two orders of magnitude faster than nonembrittled crack growth. It is difficult to conceive how a process which occurs one hundred times slower, could become competitive with the extremely fast crack growth that occurs in mercury.

One possible explanation could be the restriction of flow of the liquid metal along the newly created crack surfaces. Recalling Eq. (5.7), we find that the fluid velocity is directly related to the crack surface separation, h. Since it has been shown in the literature that even high strength aluminum alloys can exhibit crack closure under cyclic fatigue conditions,[64] it can be assumed that closure is occurring during the tests reported. This suggests that the crack surfaces could prevent access of the liquid mercury to the crack tip, effectively retarding crack growth.

Perhaps the most interesting results reported in this report are those of the static and cyclic fatigue tests at various temperatures. These results are summarized in Table 5.2. The crack velocity and K_{ILME} for the static fatigue tests, and the slopes of the da/dN versus ΔK data for the environmental component of cyclic fatigue crack growth, are presented as a function of temperature. The following basic observations can be made from the data. The threshold K_{ILME} values decrease with decreasing temperature, while K_{Ic} remains essentially constant. Both the upper and lower steady state crack velocities increase with decreasing temperature for the static fatigue tests. The slopes of the da/dN versus ΔK curve of the environmental component of cyclic fatigue crack growth increase with decreasing temperature.

The temperature dependence of K_{ILME} may be related to a brittle-to-ductile transition property of 6061-T651. The K_{Ic} results show clearly that the threshold dependence on temperature is due to the mercury. This type of temperature dependance has been predicted theoretically.[49] In that paper, Rice[49] expands the Griffith theory[37] to consider environmental effects. Briefly, it is shown that the energy release rate, G, required to cause crack

TABLE 5.2. SUMMARY OF THE STATIC FATIGUE AND CYCLIC FATIGUE TESTS AT VARIOUS TEMPERATURES

Temperature		K_{ILME} $MPa\sqrt{m}$		K_{Ic} $MPa\sqrt{m}$	Crack Velocity (m/s)		Slope m
°C	°K	Load Control	Displacement Control		Upper	Lower	
-25	248	3.5	3.5	29	9.6×10^{-2}	1.7×10^{-2}	12.52
0	273	7.0	8.0	27	8.2×10^{-2}	9.8×10^{-3}	10.14
25	298	8.5	12.5	26	6.0×10^{-2}	6.0×10^{-3}	7.52
45	323	12.0	12.0	25	4.9×10^{-2}	6.5×10^{-3}	----

growth in an environment is strongly dependent upon the amount of adsorption of the environmental species on the fracture surface. Since the amount of adsorption increases with decreasing temperature (see Appendix B), it is expected that K_{ILME} should decrease with decreasing temperature. Therefore, it seems that surface adsorption plays a key role in the embrittlement of 6061-T651 by liquid mercury.

The importance of the adsorption can be further seen by examining the kinetic nature of the measured crack growth. If we consider the crack velocities and the measured slopes, m, as rate constants, the activation energy of crack growth, Q can be calculated using an Arrhenius equation:

$$\text{Rate Constant} = A \exp \left(\frac{-Q}{RT}\right) \tag{5.9}$$

The crack velocity values and m values are plotted against 1/T in Figure 5.8. In semi-log space, the slope of these curves has the value $-Q/R$, where R is the gas constant. From the plot, the values of activation energy are -1.9 kcal/mole, -2.9 kcal/mole, and -1.7 kcal/mole, for the load control crack velocity, displacement control crack velocity, and m values respectively. In Appendix B, a theoretical value of adsorption potential (the activation energy of absorption for mercury on aluminum) is calculated as 3.5 kcal/mole. The reasons why the reaction is faster at lower temperatures are also given in Appendix B. Therefore it seems that adsorption is the rate limiting process in the embrittlement of 6061-T651 by liquid mercury.

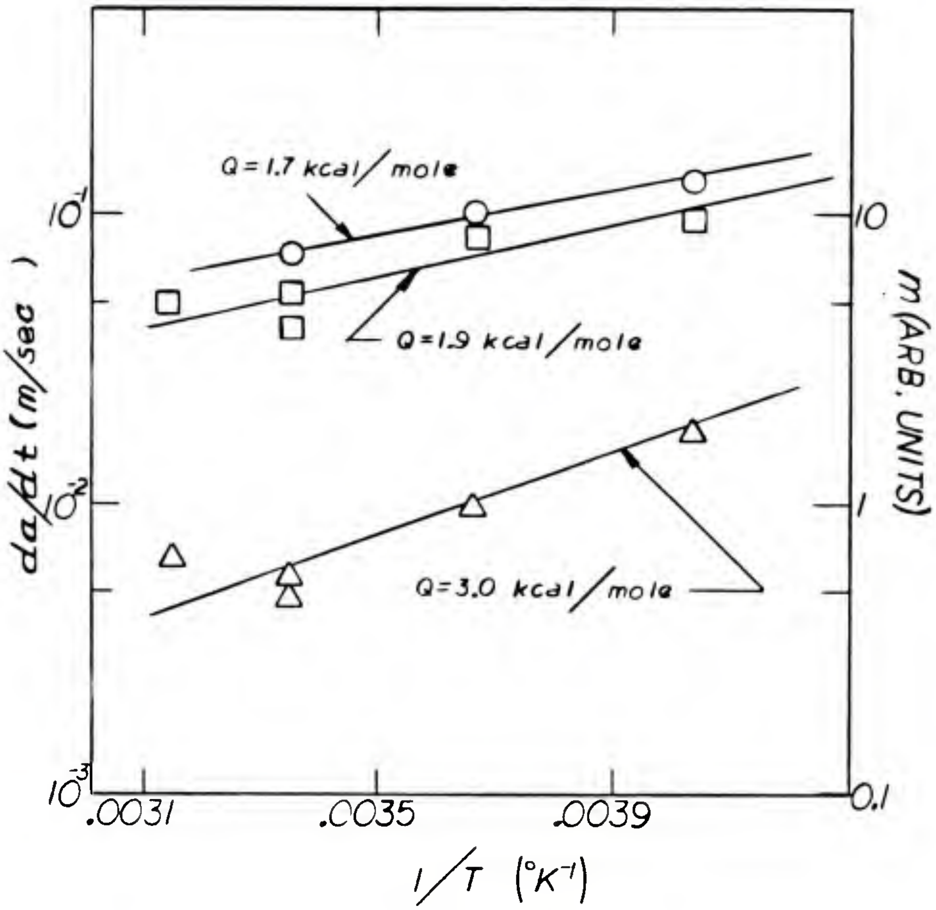

Figure 5.8. Plot of crack velocity and slope m versus 1/T for the results at various temperatures in 6061-T651.

These findings lead us to make some comments as to the mechanism of embrittlement of aluminum by liquid mercury. For embrittled crack growth to occur, the liquid metal fills the capillary which is formed in the wake of the advancing crack, until the liquid approaches close to the crack tip. Once in the vicinity of the crack tip, final transport of the liquid mercury to the crack tip occurs by sublimation and gas transport. Adsorption follows, which limits the rate of the embrittlement reaction. The actual magnitude of the rate of crack growth, on the order of cms/s, indicates that the micromechanism of embrittlement occurs very rapidly.

Comparing our data and analysis with the four previously presented micromechanisms of embrittlement, two could not be operating in this particular case. These are the rapid dissolution mechanism of Robertson[33] and the grain boundary penetration model.[34] For both of these mechanisms, the rate of embrittlement must increase with increasing temperature, which is opposite to what was measured. There was little evidence to formulate a new micromechanism based on the observations made here. Therefore we will limit the remaining discussion on mechanisms to the enhanced shear model of Lynch,[7-10] or the reduced cohesion mechanism of Stoloff and Johnston,[31] and Westwood and Kamdar.[32] If either of these two mechanisms were operating, the actual embrittlement reaction should occur instantaneously, and the actual rate of crack growth would be limited by a slower reaction, such as surface adsorption.

Let us first consider the enhanced shear model. To observe the enhanced shear model would require the use of high resolution transmission electron microscopy. This was not performed in this study. There was some evidence of enhanced plasticity in the 1100-0 load control static fatigue tests, observed with the scanning electron microscope (Figures 4.3e and 4.3f). Since the fractographic evidence of enhanced plasticity is minimal, it behooves us to theoretically examine the likelihood of enhanced plasticity at a sharp crack. Rice and Thompson[50] have studied this problem in inert environments. The criteria they develop for blunting of a sharp crack by dislocation emission are as follows:

1) There is some critical disdain, r_{crit}, that a dislocation must move in order to remain emitted and stable. In other words, there is a competition between the shearing stress driving the dislocation away from the crack tip and mirror forces driving it towards the crack tip.

2) If the calculated value of r_{crit} is greater than the core size of the dislocation, then emission of the dislocation from the crack tip is impossible.

3) If the calculated value of r_{crit} is less than the core size of the dislocation, emission of the dislocation is spontaneous.

The value of r_{crit} can be estimated closely by the simple equation:

$$r_{crit} = \frac{G'b}{10\gamma} \tag{5.10}$$

where G' is the shear modulus of the solid metal, γ is the surface energy of the fracture surface, and b is the magnitude of the Burgers vector of the dislocation.

To apply these criteria to environmentally assisted crack growth, we must examine the effect of the environment on the properties on the right-hand side of Eq. (5.10). Some experiments have been performed to determine such environmental effects. Lunarska et al[68] have measured, using a torsion pendulum, a decrease of about 80 percent in G' for iron saturated with hydrogen. Westwood and Kamdar,[32] have shown that the fracture surface energy of zinc in mercury or gallium, is only 50 percent of the cleavage fracture surface energy of zinc in air. If these results are considered as nominal for environmental systems, the effect of such changes on the value of r_{crit}, and thus the likelihood of dislocation emission from an atomistically sharp crack can be determined. Reducing the value of G' would decrease r_{crit} and increase the probability of dislocation emission. Reducing γ, would increase r_{crit}, and reduce the likelihood of dislocation emission. If G' is decreased more than γ is decreased, the net effect would be to enhance the possibility of dislocation emission. This is true if the core size of the emitted dislocation is unaffected by the environment. Furthermore, Eq. (5.10) indicates that r_{crit} should not be a strong function of yield strength. Therefore the magnitude of the reduction of the stress required to emit a dislocation from a crack tip, would be essentially constant for all the alloys tested. This suggests that the greatest relative reduction in the stress required to emit dislocations from crack tips would occur in the lower yield strength materials. The limited evidence of enhanced plasticity is observed in the lowest yield strength material.

The enhanced shear model cannot explain adequately the yield strength effects in crack velocity. Assuming that the reduced cohesion model was operating provides a superior explanation for the yield strength effects measured. Comparing the various yield strength materials under the same loading conditions, there would be more blunting of the crack tip in the lowest yield strength materials. Since the stress at the crack tip is reduced with increased blunting, it can safely be assumed that embrittlement should be easier with higher yield strength materials than with lower yield strength materials. The crack velocity then, should decrease with decreasing yield strength. This was observed in the data. Also, there was very little or no evidence of plasticity on the fracture surfaces of the alloys tested. The only exception was the 1100-0 load control static fatigue specimen, which suggests that a brittle mechanism was operating. Reduced cohesion was probably the mechanism which was operating in the aluminum-mercury systems studied.

6. CONCLUSIONS

It is clearly shown that crack velocities on the order of cms/s occur when cracks are grown under static fatigue conditions in the aluminum-mercury LME couple. Crack velocities of this magnitude are easily measured using fracture mechanics testing techniques. There is a relationship between yield strength and the magnitude of crack velocity when tested in mercury. As strength increases, the crack velocity also increases. This result is attributed to the influence of crack tip blunting in the lower yield strength materials, causing the embrittlement reaction to occur at a slower rate.

There is a hysteresis in the crack velocity with loading conditions. This is attributed to crack surface closure which restricts the flow of the liquid metal to the crack tip, retarding the rate of crack growth. There is no relationship between the threshold K value of embrittled crack growth and yield strength.

The cyclic fatigue results indicate the same conclusions for the effect of yield strength on embrittlement. Increasing yield strength increases the maximum crack growth rate. There is no relationship between yield strength and the threshold ΔK values for embrittled crack growth, and crack closure plays an important role in determining the magnitude of accelerated crack growth rate. In addition there is a significant effect of loading frequency on crack growth rate. Cracks grow much faster with decreasing frequency. An attempt to predict cyclic fatigue crack growth rates from the static fatigue crack velocity measurements does not result in a good correlation. In some cases, the prediction overestimates the actual behavior by as much as a factor of 200. Again, crack closure restricting the flow of the liquid metal to the crack tip is assumed to be the reason for the poor agreement.

Static fatigue and cyclic fatigue tests at various temperatures (-25°C to +45°C) showed that the rate of crack growth increases with decreasing temperature. The activation energy of crack growth shows that the rate limiting process of LME in the aluminum-mercury couple is surface adsorption at the crack tip by the mercury. This suggests that the transport mechanism is flow of the liquid metal to a location in the vicinity of the crack tip, followed by transport in the gas phase with adsorption as the final step.

The fractography shows that at ambient temperatures, the fracture was predominantly brittle intergranular. In one test of the 1100-0 alloy some evidence of plastic deformation was present. At lower temperatures in 6061-T651, there were increasing amounts of transgranular brittle fracture. These results indicate that the actual mechanism of LME, in the couples tested here, is probably reduced cohesion. The limited evidence of enhanced plastic deformation, combined with some theoretical discussion, indicates that the enhanced plasticity contribution to the aggregate embrittlement phenomena is probably small.

7. SUGGESTED FUTURE WORK

Some further theoretical work should be conducted using an analysis similar to that used by Rice and Thompson,[50] but including the effects of an adsorbed atom at the crack tip. This might change the criterion of dislocation emission from a crack tip (Eq. (5.10)). Without such work, any arguments of crack tip dislocation emission in the presence of an embrittling environment, either presented here or in the work of Lynch,[7-10] are only educated speculations.

More crack growth measurements under static fatigue conditions should be conducted in a material where there is no change in fracture mode with temperature. This would result in a determination of the kinetic nature of crack growth in liquid metal environments. Such a study using large single crystals, broken in a liquid metal environment, would result in totally transcrystalline fracture, regardless of temperature. Large single crystals of nickel, zinc, and iron-silicon can be grown. All three of these materials are embrittled by mercury, and the tests described herein could be easily performed on them.

The use of quantum mechanics to predict the surface adsorption kinetics could be useful in the prediction of such aspects of LME as susceptibility to embrittlement, new embrittlement couples, and temperature recovery from embrittlement. This could be accomplished by using the analysis in Appendix B and the work of Rice[49] to predict changes in K_{ILME} as a function of temperature and at what temperature the adsorption effects would be minimal.

Experimental studies on the same alloy treated to result in various yield strengths should be performed. The results reported here suggest there is a significant effect of yield strength on crack growth behavior. Using the same alloy to study this effect would eliminate the possibility that the observed effects, primarily the hysteresis with loading conditions in static fatigue, are indeed the result of yield strength changes, and not the result of alloy changes.

REFERENCES

1. Stoloff, N. S., "Solid and Liquid Metal Embrittlement," Presented at the the NATO Advanced Study Institute on Atomistics of Fracture, Corsica, May, 1981, to be published.
2. Nicholas, M. G. and Old, C. F., J. of Mat. Sci., Vol. 14, 1979, p. 1.
3. Stoloff, N. S., "Recent Developments in Liquid-Metal Embrittlement," Environment-Sensitive Fracture of Engineering Materials, Ed. Foroulis, Z. A., The Metallurgical Society of AIME, Warrendale, PA, 1979, p. 486.
4. Kamdar, M. H., "Embrittlement by Liquid Metals," Prog. Mat. Sci., Vol. 15, 1973, p. 289.
5. Rostoker, M. H., McCaughey, J. M., and Markus, M., Embrittlement by Liquid Metals, Reinhold, NY, 1960.
6. Corrosion by Liquid Metals, Plenum Press, NY, 1970.
7. Lynch, S. P., in Proceedings Fourth International Conference on Fracture, Waterloo, Canada, 1977, p. 859.
8. Lynch, S. P. and Ryan, N. E., Hydrogen Damage, ASM, Metals Park, OH, 1977, p. 369.
9. Lynch, S. P. Scripta Met., Vol. 13, 1979, p. 1051.
10. Lynch, S. P., Acta. Met., Vol. 29, 1981, p. 325.
11. Kapp, J. A., and Kamdar, M. H., In progress.
12. Ashok, S., Stoloff, N. S., Glicksman, M. E. and Slavin, T. P., Scripta Met., Vol. 15, 1981, p. 331.
13. Mostovoy, S. and Breyer, N. N., Trans. ASM, Vol. 61, 1968, p. 219.
14. Warke, W. R., Johnson, K. L. and Breyer, N. N., in Reference 6.

15. Warke, W. R., and Breyer, N. N., J. Iron and Steel Inst., Vol. 209, 1971, p. 779.

16. Breyer, N. N. and Johnson, K. L., J. Testing and Evaluation, Vol. 2, 1981, p.50.

17. Lynn, J. C., Warke, W. R., and Gordon, P., Mat. Sci. and Eng., Vol. 18, 1975, p. 51.

18. Landow, M., Harsola, A. and Breyer, N. N., J. of Materials for Energy Systems, Vol. 2., 1981, p. 50.

19. Tetelman, A. S. and McEvily, A. J.,Jr., Fracture of Structural Materials, Wiley, NY, 1967.

20. Petch, N. J., J. Iron Steel Inst., Vol. 173, 1954, p. 25.

21. Cortrell, A. H., Trans AIME, Vol. 212, 1958, p. 19.

22. Johnson, K. L., Breyer, N. N. and Dally, J. W., Proc. Conf. on Environmental Degradation of Engineering Materials, Blacksburg, VA., 1977, p. 91.

23. Stoloff, N. S., in Surfaces and Interfaces II: Physical and Mechanical Properties, 14th Sagamore Army Res. Conf., 1968, p. 158.

24. Rinnovatore, J. V., Corrie, J. D. and Markus, H., Trans ASM, Vol. 58, 1967, p. 155.

25. Iwata, Y., Asayama, Y. and Sakamoto, J., J. Japan Inst. Met., Vol. 37, 1967, p. 77.

26. Bedlow, J. K., Ph.D. Thesis, Cambridge University.

27. Regan, T. M. and Stoloff, N. S., Met Trans A, Vol. 7A, 1977, p. 885.

28. Chaevskii, M. I., Sov. Mat. Sci., Vol 1., 1965, p. 433.

29. Kelley, M. J. and Stoloff, N. S., Met Trans A, Vol 6A, 1975, p. 159.

30. Old, C. F., in Fracture 1977, Proc. ICF 4, Vol.2, Waterloo, Canada, 1977, p. 331.

31. Stoloff, N. S. and Johnston, T. L., Acta. Met., Vol. 11, 1963, p. 251.

32. Westwood, A. R. C., and Kamdar, M. H., Phil. Mag. Vol. 8, 1963, p. 787.

33. Robertson, W. M., Met. Trans., 1970, p. 2607.

34. Krishtal, M. A., Sov. Phys. Dolk., Vol. 15, 1970, p. 61.

35. Gordon, P. Met. Trans. A, Vol. 9A, 1978, p. 267.

36. Irwin, G. R. and Kies, J. A., Welding Journal Research Supplement, Vol. 33, 1954, p. 193.

37. Griffith, A. A., Phil. Trans. Roy. Soc. Series A, Vol. 221, 1920, p. 163.

38. Irwin, G. R., J. of Appl. Mech., Trans ASME, Vol. 24, 1957, p. 361.

39. Westergaard, H. M., J. of Appl. Mech., Trans ASME, 1939.

40. Paris, P. C. and Erdogan, F., J. of Basic Eng., Trans ASME, Series D., Vol. 85, 1963, p. 4.

41. Novak, S. R. and Rolfe, S. T., J. of Materials, Vol. 4, No. 3, 1969.

42. Wei, R. P., Novak, S. R., and Williams, D. P., Matls. Res. Stand., 1972, Vol. 12, p. 25.

43. Clark, W., J. of Materials for Energy Systems, Vol. 1, 1980, p. 35.

44. Landes, J. D. and Wei, R. P., Int. J. Fract., Vol. 9, 1973, p. 277.

45. Wei, R. P. and Landes, J. D., Matls. Res. Stand., Vol. 9, No. 7, 1969, p. 9.

46. Simmons, G. W., Pao, P. S., and Wei, R. P., Met. Trans. A, Vol. 9A, 1978, p. 1147.

47. Wei, R. P., Fatigue Mechanisms, Ed. Fong, J. T., ASTM STP 675, ASTM, Philadelphia, PA, 1979, p. 816.

48. Speidel, M., in The Theory of Stress Corrosion Cracking in Alloys, NATO, Brussels, 1971, p. 289.

49. Rice, J. R., J. Mech. Phys. Solids, Vol. 26, 1978, p. 61.

50. Rice, J. R. and Thompson, R., Phil. Mag., Vol. 15, 1974, p. 19.

51. Underwood, J. H., Kendall, D. P., and Winters, D., in The Detection and Measurement of Cracks, The Welding Institute, England, 1976, p. 31.

52. Yoder, G. R. and Crooker, T. W., "The Procedure for Precision Measurement and Analyzing Fatigue Crack Growth Using Crack Opening for Corrosion Fatigue," Presented at ASTM E-9 Symposium, Pittsburgh, PA, Nov. 1979.

53. Clark, W. G., Jr. and Hudak, S. J., Jr., J. of Test. & Eval., Vol. 3, No. 6, 1975, p. 454.

54. Damage Tolerant Design Handbook, Part 2, Metals and Ceramics Information Center, Columbus, OH, Jan. 1975.

55. Underwood, J. H. and Kapp, J. A., "Benefits of Overload for Fatigue Cracking at a Notch," Presented at the 13th ASTM National Symposium on Fracture Mechanics, Philadelphia, PA, June 1980.

56. Alcoa Aluminum Handbook, Aluminum Company of America, Pittsburgh, PA, 1962.

57. 1981 Annual Book of ASTM Standards, Part 10, Metals - Mechanical, Fracture, and Corrosion Testing; Fatigue; Erosion and Wear; Effects of Temperature, ASTM, Philadelphia, PA, 1981.

58. Logsdon, W. A., Mechanisms of Crack Growth, ASTM STP 590, ASTM, Philadelphia, PA, 1976, p. 43.

59. Martin, J. W., Precipitation Hardening, Pergamon Press, N. Y., 1968.

60. ASM Handbook, Atlas of Microstructure, Vol. 7, ASM, Metals Park, OH, 1979.

61. Gerbrich, W. W. and Moody, N. R., Fatigue Mechanisms, ASTM STP 675, ASTM, Philadelphia, PA, 1979, p. 292.

62. Pao, P. S., Wei, W. and Wei, R. P., Environment Sensitive Fracture of Materials, The Metallurgical Society of AIME, Warrendale, PA., 1979, p. 565.

63. Inglis C., Trans. Inst. Naval Archit., Vol. 55, 1913, p. 219.

64. Elber, W., Tolerance of Aircraft Structures, ASTM STP 486, ASTM, Philadelphia, PA, 1971, p. 230.

65. Newman, J. C., Jr., Private Communication on unpublished results, May 1981.

66. Report to ASTM Committe E-24 on Fracture Testing of Task Group E-14.04.03 on Subcritical Crack Growth in Aggressive Environments, Nov. 1979, Pittsburgh, PA.

67. Carnahan, Bruce, Luther, H. A., and Wilkes, James, O., Applied Numerical Methods, Wiley, NY, 1969.

68. Lunarska, E., Zielinski, Z. and Smialowski, M., Acta Met, Vol. 25, 1977, p. 305.

APPENDIX A

FRACTURE MECHANICS SPECIMENS USED TO MEASURE CRACK GROWTH RATES

In this section the fracture mechanics parameters of the specimens used in this study are presented. There are two parameters which must be known for the specimens, the stress intensity factor (K) and the crack mouth opening displacement (CMOD). The stress intensity factor must be known since it is the parameter which governs the severity of the stress gradient near the tip of the crack and the relationship between this parameter and crack growth rates has been studied extensively.[A-1,A-2] The CMOD must be known since it was used extensively in the crack growth studies. If CMOD is known as a function of crack length and applied load, then by measuring CMOD and applied load simultaneously, the crack length can be measured as a function of time from which the crack growth rates da/dN or da/dt are derived.

Two specimens were used to develop the data contained in this report. The specimens are shown in Figure A-1 and designated as the long double cantilevered beam (LDCB) specimen and the short double cantilevered beam (SDCB) specimen. The LDCB was initially chosen as the only specimen for this study because crack growth rates in mercury embrittled specimens were expected to be very fast. Therefore a long specimen would enable one to gather embrittled crack growth rates more accurately, simply because the crack would have greater quantities of material to travel through. Most of the cyclic fatigue data for the 6061-T651 alloy was generated using this specimen, but when using this specimen under static fatigue conditions, problems with crack branching arose. Figure A-2 shows an LDCB specimen which was cycled to

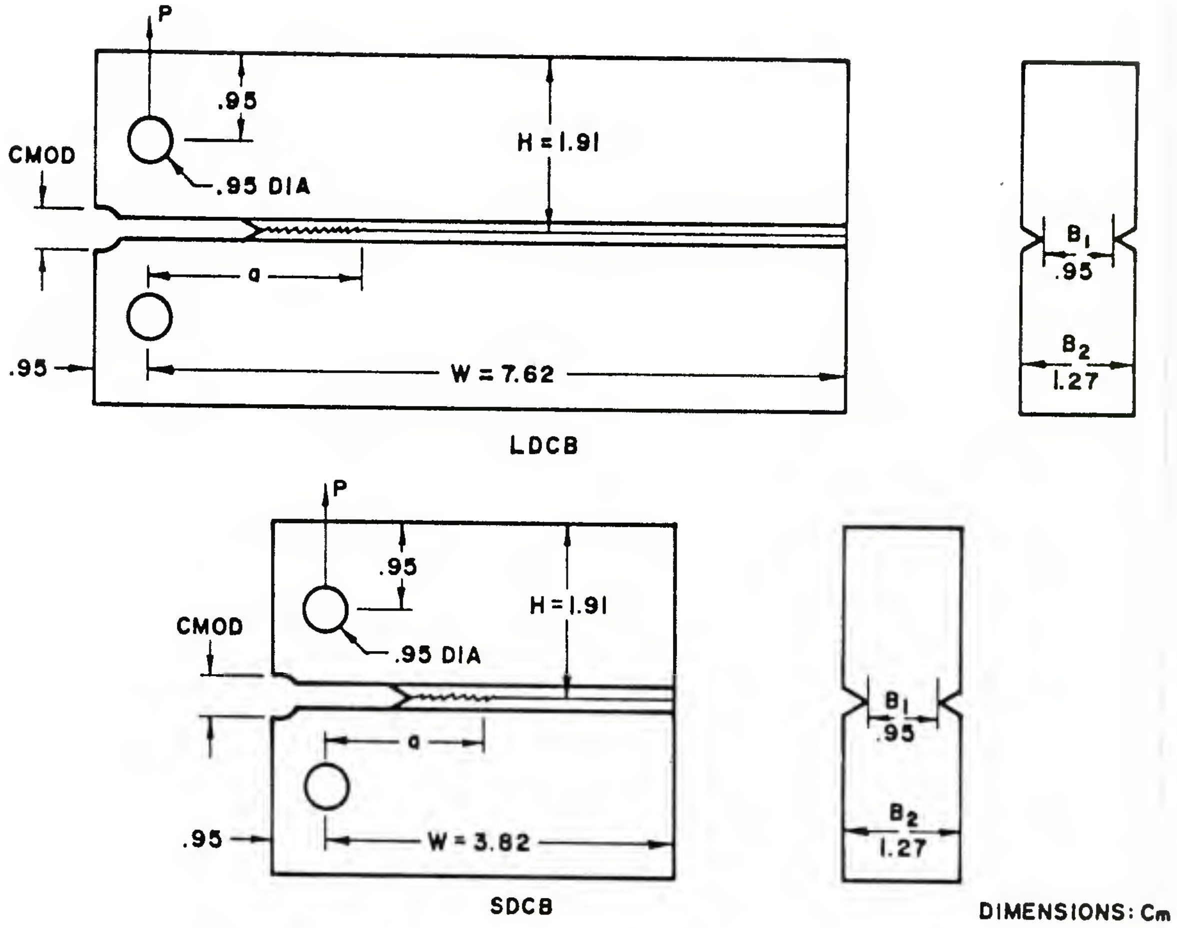

Figure A-1. The Specimens Used.

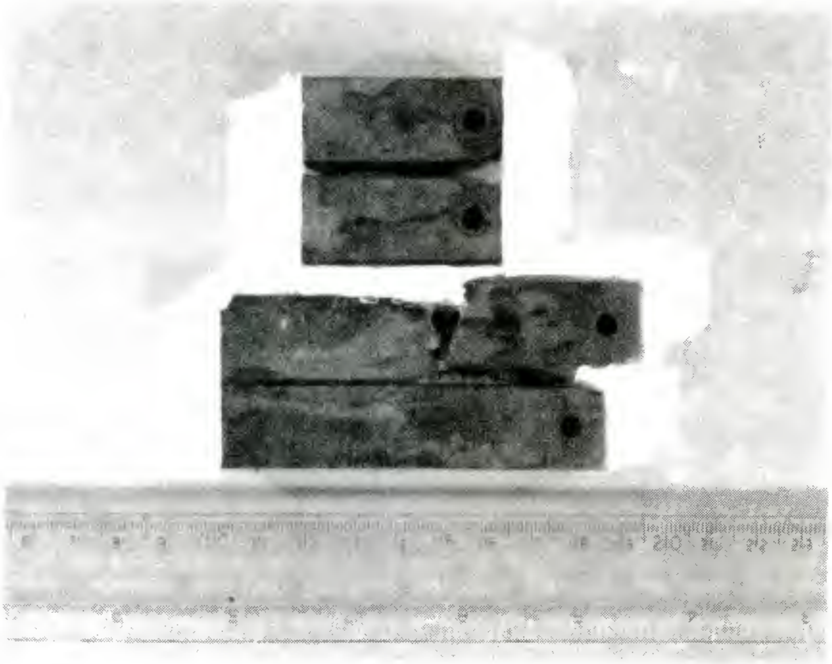

Figure A-2. Branching of the LDCB and SDCB samples.

failure. The branch crack is apparent. Branching is a phenomenon which will always occur to some extent when studying embrittlement and may result in serious experimental problems if its effects are ignored. Since crack length is measured in the rising and decreasing K studies by measuring CMOD, severe branching as shown in Figure A-2 is unacceptable. The presence of the branch cracks will certainly make the specimen more compliant and thus significantly influence the CMOD of the specimen. Therefore, the occurrence of severe branching should be minimized. The SDCB specimen reduces the likelihood of severe branching by maintaining a state of stress on the uncracked ligament which is always greater than the tensile stress which acts perpendicular to the uncracked ligament. These stresses can be calculated easily with the aid of the free body diagrams shown in Figure A-3.

The stresses that dominate crack growth in a brittle manner are usually those tensile stresses which act perpendicular to the direction of crack growth. On the uncracked ligament this stress has both a normal component due to force N and a bending component due to the moment M_W. On the plane perpendicular to the uncracked ligament, the stress has only the bending component from M_H. The shearing force S will result in a shear stress which is assumed to have a negligible effect on the growth of branch cracks as compared to the bending stress.

The stress on the uncracked ligament is given by:A-3

$$\sigma_W = \frac{N}{A} + \frac{M_W C}{I} \qquad \text{(A-1)}$$

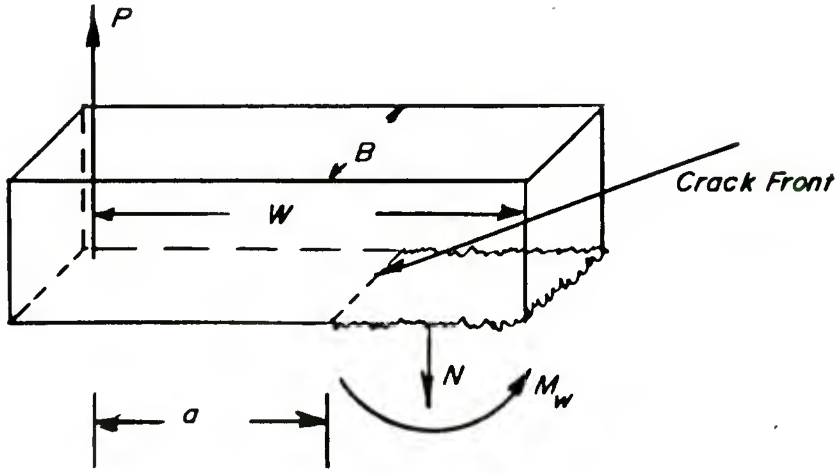

Fig A-3a Free Body Diagram for Stresses Ahead of the Crack

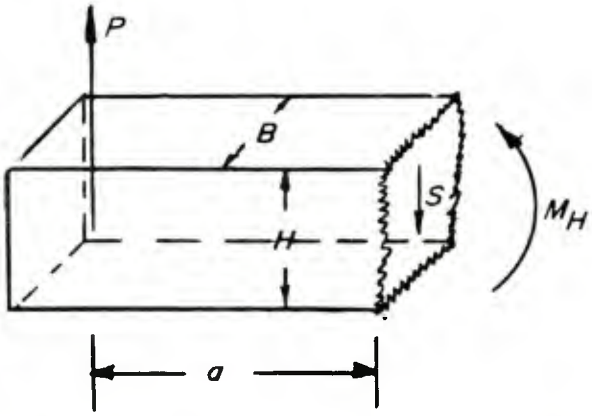

Fig A-3b Free Body Diagram for Stresses on the Plane of a Branched Crack

Figure A-3. Free Body Diagrams.

where A is the area over which the force N acts and is equal to the thickness B times the length of the uncracked ligament (W-a), I is the moment of inertia of the uncracked ligament given by $B(W-a)^3/12$ and C is $(W-a)/2$. Using these values and the values of N and M_W determined in Figure A-3, Eq. (A-1) can be written as:

$$\sigma_W = \frac{P}{B(W-a)} + \frac{3P(W+a)}{B(W-a)^2}$$

$$= \frac{P}{B(W-a)} (1 + \frac{3W+a}{(W-a)})$$

$$= \frac{P}{BW(1-a/W)} (1 + \frac{3(1+a/W)}{(1-a/W)}) \qquad \text{(A-2)}$$

The stress on the plane perpendicular to the uncracked ligament is simply:

$$\sigma_H = \frac{M_H C}{I} \qquad \text{(A-3)}$$

In this case I is $BH^3/96$ and C is $H/4$. Equation (A-3) then reduces to

$$\sigma_H = \frac{24Pa}{BH^2}$$

$$\sigma_H = \frac{24P(a/W)}{WB(H/W)^2} \qquad \text{(A-4)}$$

For comparison purposes, it is convenient to normalize the stresses σ_W and σ_H by the factor P/WB. Numerical values of the normalized stresses are then determined and presented in Table A-I. From this table it is apparent that severe branching is a strong possibility in the LDCB samples for a/W up to about .6, while for the SDCB, since σ_W is always less than σ_H, the likelihood of severe branching is reduced. No severe branching was encountered in the testing of embrittled SDCD specimens.

TABLE A-I. COMPARISON OF STRESSES FOR BRANCHING FOR THE LDCB AND THE SDCB SPECIMENS

	LDCB		SDCB	
a/W	$\sigma_H/(P/BW)$	$\sigma_W/(P/BW)$	$\sigma_H/(P/BW)$	$\sigma_W/(P/W)$
.2	19.2	6.9	4.8	6.9
.3	28.8	9.4	7.2	9.4
.4	38.4	13.3	9.6	13.3
.5	48.0	20.0	12.0	20.0
.6	57.6	32.5	14.4	32.5
.7	67.2	60.0	16.8	60.0

It is important to note at this time that the stress analysis above for σ_W would be just as valid if the free body diagram in Figure A-3b contained a branch crack at some location removed from the tip of the main crack. In other words, from simple mechanics of materials concepts there is no reason to assume that the presence of stable branch cracks removed from the tip of the main crack would substantially affect the stress state ahead of the main crack. Since K is a function of the stresses which act along the uncracked ligament ahead of the crack and the crack length, the presence of branch cracks should have little affect on K of the main crack. Therefore, if the length of the main crack can be measured by some means other than the CMOD technique, an embrittled LDCB specimen containing branched cracks should result in valid crack growth rate versus applied K results.

Another method often used to prevent severe branching is the utilization of shallow side grooves along the intended path of crack growth.[A-4,A-5] Such side grooves were utilized for this study. For liquid mercury assisted cracking studies, the side grooves serve an additional purpose in that they serve as reservoirs for the liquid metal. This enables a sufficient amount of liquid metal to be coated on the walls of the side grooves to cause embrittlement which eliminates the necessity of conducting the crack growth experiments in a mercury bath.

Although side grooves serve practical experimental purposes, their affect on the fracture mechanics parameters K and CMOD must be determined. Since an analytical solution of CMOD for either the LDCB or the SDCB is not available from the literature, it was decided to develop such a solution using the finite element method of analysis, and then to experimentally determine the effects of the side grooves.

The finite element solutions were developed by modeling the two specimens with the meshes shown in Figure A-4. The elements used were eight node quadratic isoparametric elements which have been used successfully to study other fracture mechanics specimens.[A-6,A-7] Since the specimens are symmetric about the plane of the crack, only one half of either specimen, as shown, was required for the analysis. The crack was modeled by successively releasing nodes along the plane of the crack, effectively simulating cracks of different length. CMOD was calculated at the nodes shown in the figure. An approximate solution for K may also be determined from the finite element solutions by calculating the load line displacement v_{LL} as a function of crack length and

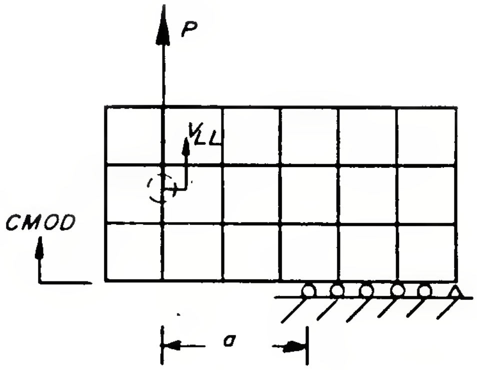

Fig A-4a Finite Element Mesh SDCB

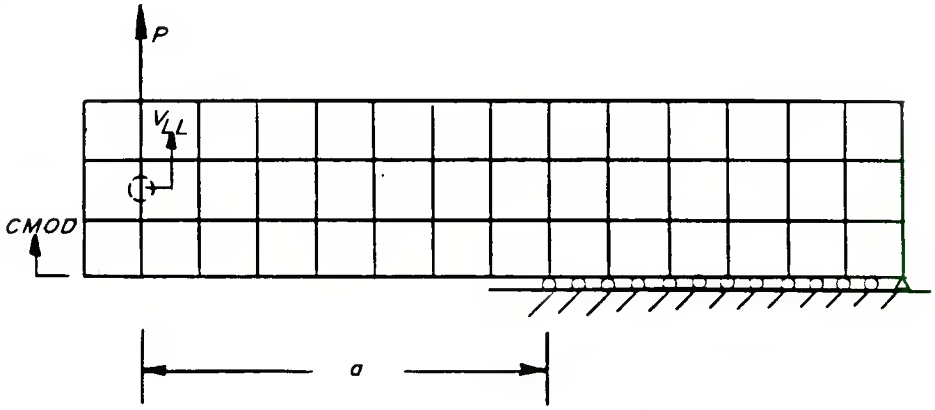

Fig A4b Finite Element Mesh LDCB

Figure A-4. Finite Element Meshes.

using the Irwin equation:[A-8]

$$G = \frac{\partial C}{\partial a} \tag{A-5}$$

where G is the energy release rate and C is the compliance of the specimen, which under elastic conditions is

$$2v_{LL} = CP \tag{A-6}$$

G is related to K under plane-strain conditions by

$$K^2 = \frac{GE}{(1-\nu^2)} \tag{A-7}$$

where E and ν are Young's modulus and Poisson's ratio respectively. The approximate K solution developed from the finite element results and Eqs. (A-5), (A-6), and (A-7) gives a quantitative measure of the accuracy of the finite element results, by comparing the approximate K solution with that which appears in the open literature.[A-9] The K solution in the literature was developed using very accurate numerical techniques designed specifically to determine K. The close agreement between the approximate solution developed here and the more accurate solution in reference A-9, as shown in Table A-II, indicates a very good solution for specimen displacements v_{LL} or CMOD from the finite element analysis. The numerical values of CMOD from the finite element analysis are shown in Table A-II.

TABLE A-II.

$$f = \frac{KB\sqrt{W}\ (1-a/W)^{3/2}}{p\ \ (1.7+a/W)}$$

Specimen	a/W	f(Ref. A-9)	f(Finite Element)	f(Eq. (A-13) or (A-14))
LDCB	.2	3.841	3.84	3.845
	.3	3.807	3.63	3.793
	.4	3.488	3.21	3.494
	.5	2.985	2.94	3.007
	.6	2.459	2.27	2.424
	.7	1.835	1.88	1.847
	1.0	1.464	-	1.461
SDCB	.2	2.004	2.15	2.003
	.3	1.900	1.96	1.905
	.4	1.773	1.72	1.769
	.5	1.639	1.58	1.637
	.6	1.531	1.51	1.537
	.7	1.484	1.49	1.481
	1.0	1.464	-	1.464

The effects of the side grooves can be determined by growing a crack in a specimen containing the side grooves and measuring CMOD. This was done for both specimens and is most conveniently compared with the finite element results in Figure A-5. From the curves it is apparent that the side grooves have the effect of reducing the thickness B of the sample. The same effect has been observed in other side grooved samples.[A-4, A-5] In both of these previous studies, the side grooves were found to give the specimens an effective thickness (B_{eff}), which is the geometric mean of the maximum thickness B_1 and the minimum thickness B_2

$$B_{eff} = \sqrt{B_1 B_2} \qquad \text{(A-8)}$$

Using this value for thickness, the experimental CMOD measurements are in excellent agreement with those developed with the finite element analysis. This shows that side grooves affect only the specimen thickness B. Since K is also linearly related to thickness, using the effective thickness calculated by Eq. (A-8) and the solution from reference A-9, K for side grooved specimens can be calculated.

Since both K and CMOD were determined many times in the study, it was convenient to develop expressions to accomplish this. First the K solution is considered. Wide range expressions for K have been developed for several specimens.[A-10,A-11] The procedure is to find a normalized form of K which has finite, non-zero limits as a/W approaches both zero and one. This is normally not possible for a/W approaching zero for specimens similar to the SDCB and LDCB, because of interaction between the crack and the loading holes. A limit for K as a/W approaches one is easily obtained for these samples. The solution for a semi-infinite crack in a semi-infinite plate subjected to both a moment

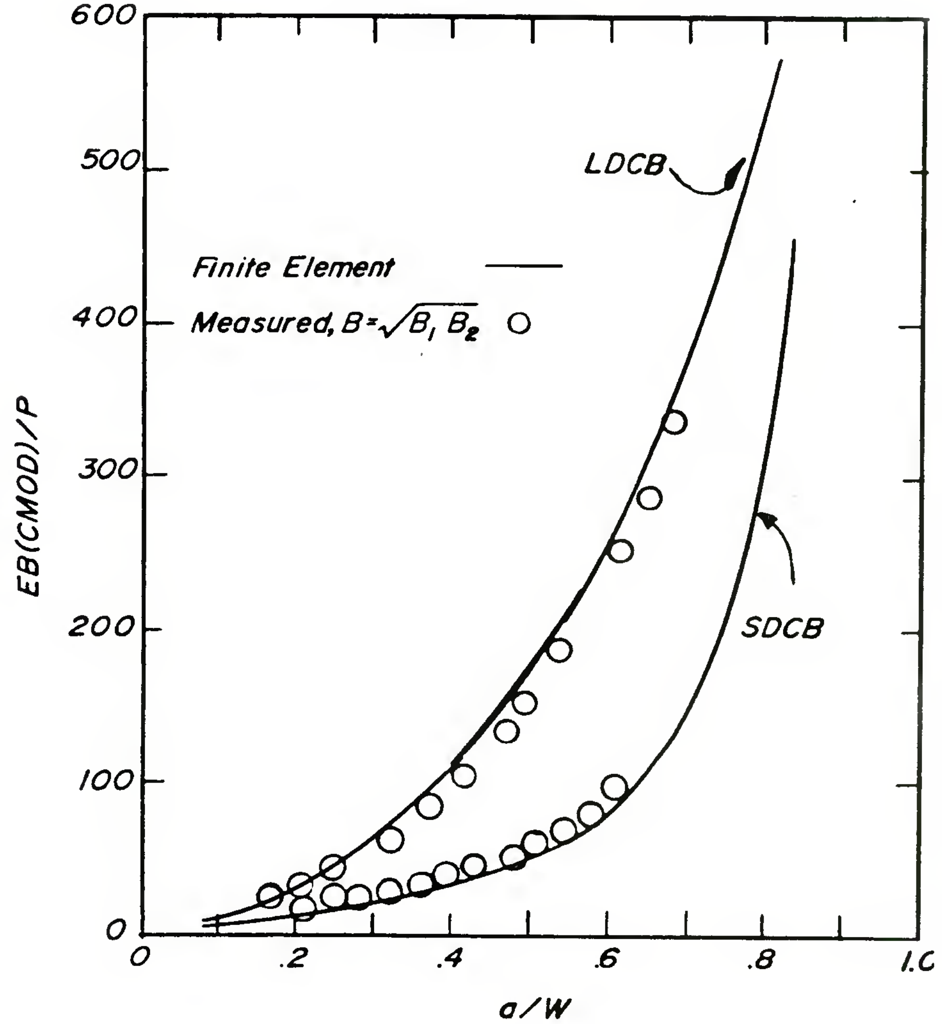

Figure A-5. CMOD Solutions.

and a normal force[A-12] is appropriate. For an applied moment M, K is

$$K = \frac{3.975\,M}{BW^{3/2}(1-a/W)^{3/2}} \qquad \text{(A-9)}$$

For applied force P, acting at the centroid of the uncracked ligament, K is

$$K = \frac{0.928\,P}{BW^{1/2}(\pi\, a/W)^{1/2}} \qquad \text{(A-10)}$$

Combining Eqs. (A-9) and (A-10) and realizing that $M = P((W+a)/2)$, a finite limit for the nondimensional form for K is given as

$$\lim_{a/W\to 1} \frac{KBW^{1/2}(1-a/W)^{3/2}}{P(1.7+a/W)} = 1.464 \qquad \text{(A-11)}$$

Now the numerical K results for the SDCB and the LDCB can be fit to an equation of the form

$$\frac{KBW^{1/2}(1-a/W)^{3/2}}{P(1.7+a/W)} = f(a/W) \qquad \text{(A-12)}$$

Using the multivariable linear regression, f(a/W) was found to fit the polynomials for the LDCB and the SDCB respectively:

$$f(a/W) = 3.02 + 7.74\,a/W - 17.13(a/W)^2 + .451(a/W)^3 + 7.65(a/W)^4 \qquad \text{(A-13)}$$

$$f(a/W) = 1.84 + 2.41(a/W) - 12.9(a/W)^2 + 16.1(a/W)^3 - 6.41(a/W)^4 \qquad \text{(A-14)}$$

Equations (A-13) and (A-14) are compared to the numerical solutions in Table A-II and show excellent agreement over the the wide range of $.2 < a/W < 1$, and are accurate to ± .5 percent for the SDCB and ± 1.4 percent for the LDCB.

To fit an expression to predict (a/W) from CMOD measurements is somewhat more difficult since there has been no formal procedure published in the open literature as has been done for K expressions. Recently, Newman[A-13] has developed an expression for the round compact specimen which has given good results for determining a/W. In that deviation, a/W was assumed to be a function of a nondimensional form of CMOD:

$$a/W = f(\delta') \tag{A-15}$$

where

$$\delta' = \ln\left(\frac{EB(CMOD)}{P}\right) \tag{A-16}$$

Using the finite element solutions for CMOD for the SDCB an expression which is valid for $.0833 < a/W < .833$ and accurate to ± 3.5 percent was developed as

$$a/W = .1351 - .1874\,\delta' + .1117(\delta')^2 - .0102(\delta')^3 \tag{A-17}$$

where δ' is defined by Eq. (A-16). An expression of this type for the LDCB was not developed since that specimen was not used in the static fatigue tests.

APPENDIX REFERENCES

A-1. Paris, P. C., in Fatigue An Interdisciplinary Approach, Syracuse University Press, Syracuse, NY, 1964, p. 107.

A-2. Wei, R. P., Novak, S. R., and Williams, D. P., Matls. Res. Stand., Vol. 12, 1972, p. 25.

A-3. Timoshenko, S. P., Strength of Materials, Part II, Third Edition, D. Van Nostrand, Princeton, NJ, 1956.

A-4. Crosley, P. B. and Ripling, E. J., in Fast Fracture and Crack Arrest, ASTM STP 627, ASTM, Philadelphia, PA, 1977, p. 372.

A-5. Novak, S. R. and Rolfe, S. T., J. of Materials, Vol. 4, No. 3, 1969.

A-6. Hussain, M. A., Lorensen, W. E., and Pflegl, G. A., "The Quarter-Point Quadratic Isoparametric Element as a Singular Element for Crack Problems," NASA Technical Memorandum, NASTRAN: Users' Experience, 1976.

A-7. Kapp, J. A., Pflegl, G. A., and Underwood, J. H., Int. J. Fracture, Vol. 13, 1977, p. 721.

A-8. Irwin, G. R. and Kies, J. A., Welding Journal, Research Supplement, Vol. 33, 1954, p. 193.

A-9. Gross, B. and Srawley, J. E., "Stress Intensity Factors for Boundary Collocations for Single-Edge-Notch Specimens Subject to Splitting Forces," NASA TN D-3295, NASA-Lewis Research Center, Cleveland, OH, 1966.

A-10. Srawley, J. E., Int. J. Fracture, Vol. 12, No. 3, June 1976, p. 475.

A-11. Kapp, J. A., Newman, J. C. Jr, and Underwood, J. H., J. Testing and Evaluation, Vol. 8, No. 6, Nov. 1980, p. 314.

A-12. Tada, H., Paris, P. and Irwin, G., The Stress Analysis of Cracks Handbook, Del Research Corporation, Hellertown, PA, 1973.

A-13. Newman, J. C. Jr, "Stress Intensity Factors and Crack Opening Displacements for Round Compact Specimens," NASA TM 80174, NASA-Langley Research Center, Hampton, VA, 1979.

APPENDIX B

SURFACE ADSORPTION AND ITS APPLICATION TO ENVIRONMENTALLY ASSISTED FRACTURE

Surface adsorption of an embrittling liquid metal has traditionally been considered a prerequisite of liquid metal embrittlement (LME).[B-1] Little qualitative work has been performed to relate physical adsorption to LME, or to any other forms of environmentally assisted fracture. One could argue that adsorption is the first step in the mechanism of any embrittlement phenomenon, since the environment must react with the surface of a specimen before any effect in the bulk material. If such surface interactions do not take place, then the environment would not have access to the material, and no effect on the fracture behavior of the material would be observed. It seems that adsorption of the embrittling species should be an important prerequisite, not only to LME, but also to hydrogen embrittlement and stress corrosion cracking. In fact, Rice[B-2] has recently developed a theory making it possible to calculate the strain energy release rate (G), required to grow a crack in the presence of an aggressive environment from a knowledge of the adsorption properties of the environment and the solid metal which it embrittles. Performing such calculations for the aluminum-mercury system studied in this report was not attempted. However, the study of the adsorption kinetics of mercury on solid aluminum below shows that, in the case of aluminum alloys embrittled by liquid mercury, adsorption plays a crucial role.

First we must discuss the phenomenon of physical adsorption. The adsorption of a fluid by the surface of a solid has been studied for at least seventy years. During that time, a substantial literature has evolved, including papers, conference proceedings, and books. Borrowing the first few sentences from the introduction of the book by Ross and Olivier,$^{B-3}$ physical adsorption can be defined as:

> "The adsorption of a gas or vapor by a solid surface must be thought of as an incipient condensation that can take place to some extent, at any pressure, no matter how low. The adsorbed film, like the condensed phase into which it passes as the pressure is raised beyond the saturation vapor pressure may be regarded as a thermodynamically separate phase - a two dimensional phase; but a curious distinction appears: the adsorbed film has a close analogy to a solution, since the quantity adsorbed per unit area (i.e. the surface concentration) varies with the superimposed pressure. A true condensed phase which is a one-component system, cannot, of course, be described in these terms."

Thus it seems that an adsorbed film is an entirely different phase than either the fluid phase (adsorbent), or the solid phase (adsorbate), with totally different properties than either parent phase. To characterize this system of phases, we must use a modified form of the phase rule:

$$P + F = C + 2 + i \tag{B-1}$$

where P is the number of phases, F is the number of degrees of freedom, C is the number of components, and i is the number of interfaces considered. The simplest system to consider is a two-component system, made up of one fluid phase and one solid phase, one adsorbed phase and one interface. In such a system, Eq. (B-1) becomes:

$$3 + F = 2 + 2 + 1$$

$$\text{or } F = 2$$

Therefore, there are two degrees of freedom. In this system, there are four stated variables: pressure, p; temperature, T; the concentration of the fluid phase; and the concentration of the adsorbed phase, Θ. If any two of these variables are fixed, the other two are known. Thus, adsorption properties are measured as "adsorption isotherms", where Θ is plotted as a function of p at constant T. The surface concentration is not measured directly, but is inferred from measuring the fluid concentration as the pressure is increased. Figure B-1 is a schematic of some simple adsorption isotherms.

To mathematically describe adsorption isotherms, one must first envision the adsorbed film in a state of dynamic equilibrium. Consider the adsorbent as a gas and the adsorbate as a solid. The gas atoms are constantly striking the surface of the solid of which a certain fraction, f_i, will adsorb onto the available sites $(1-\Theta)$. An expression for the rate of adsorption, u, is given by Langmuir:[B-4]

$$u = \left(\frac{pN}{\sqrt{2\pi MRT}}\right) f_i \,(1-\Theta) \qquad \text{(B-2)}$$

where N is Avogadro's number, M is the molecular weight of the adsorbate, and R is the gas constant. Also in the Langmuir paper, the expression for the rate of desorption, v, from the adsorbed film is given as:

$$v = k_o \,\Theta \exp\left(\frac{-U_o}{RT}\right) \qquad \text{(B-3)}$$

where k_o is a constant, and U_o is the adsorptive potential.

At equilibrium, the rate of adsorption must equal the rate of desorption. Considering Eqs. (B-2) and (B-3) with temperature constant, the equation

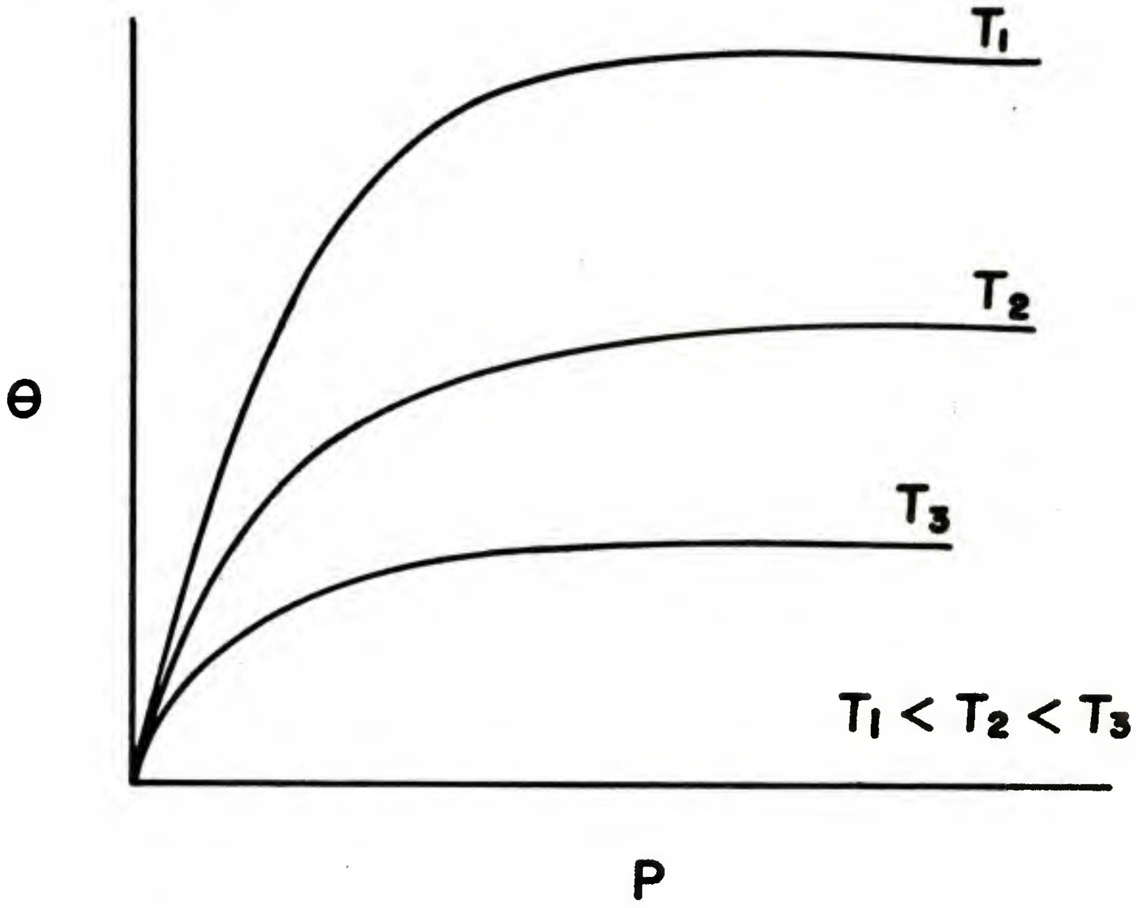

Figure B-1. The Temperature Variation in Adsorption Isotherms.

for Langmuir's adsorption isotherm is:

$$p = \frac{K'\Theta}{(1-\Theta)} \qquad (B-4)$$

where

$$K' = \left(\frac{k_o\sqrt{2\pi MRT}}{N}\right) \exp\left(\frac{-U_o}{RT}\right) \qquad (B-5)$$

Other mathematical expressions for adsorption isotherms can be derived in a similar manner. All the derivations, including Eqs. (B-4) and (B-5) can be summarized in the general mathematical form:

$$p = K' \; fn\,(\Theta) \qquad (B-6)$$

where

$$K' = A(T) \exp\left(\frac{-U_o}{RT}\right) \qquad (B-7)$$

Another interesting derivation can be made regarding the rate of the adsorption-desorption reaction, w. This rate is simply the rate of adsorption, u, minus the rate of desorption, v. Using Eqs. (B-2) and (B-3), an expression for w may be derived:

$$w = \left(\frac{pN}{\sqrt{2\pi MRT}}\right) f_i\,(1-\Theta) - k_o\,\Theta \exp\left(\frac{-U_o}{RT}\right) \qquad (B-8)$$

In more general terms, w may be expressed as:

$$w = \frac{B(p,\Theta)}{\sqrt{T}} - C(\Theta) \exp\left(\frac{-U_o}{RT}\right) \qquad (B-9)$$

The result of this derivation Eq. (B-9), shows that the rate of the adsorption-desorption reaction results from the competition between two processes; one which is not thermally activated, the first term, and another process which is thermally activated, the second term. This means that as the temperature increases, the first term in Eq. (B-9) contributes a smaller amount to the aggregate reaction rate. Concurrently, the second, activated term, contributes a greater negative amount to the reaction rate. The total effect of temperature increases is to reduce the rate of the adsorption-desorption reaction. Conversely, a decrease in the temperature results in a faster rate of reaction. Therefore, if another event, such as the rate of crack growth, is limited by the adsorption-desorption reaction, then one would expect the rate of the secondary, limited process to be increased with decreasing temperatures. This is opposite from what would be measured if the secondary process was limited by a noncompetitive, thermally activated process. The prior case, increasing rates of crack growth with decreasing temperatures, was measured in the experiments reported in the main body of this report. This suggests that one possible explanation for the observed behavior was adsorption limited crack growth.

There is one parameter which is involved in the above discussions of both the thermodynamics and kinetics of surface adsorption, the adsorptive potential U_o. This potential is the energy lost by a molecule when it passes from the gaseous phase to the adsorbed phase. The magnitude of U_o can be estimated with the aid of Figure B-2, which shows the potential energy of a fluid molecule as a function of distance (x) from the surface. If a molecule were to approach the surface of a solid, the potential energy of the molecule

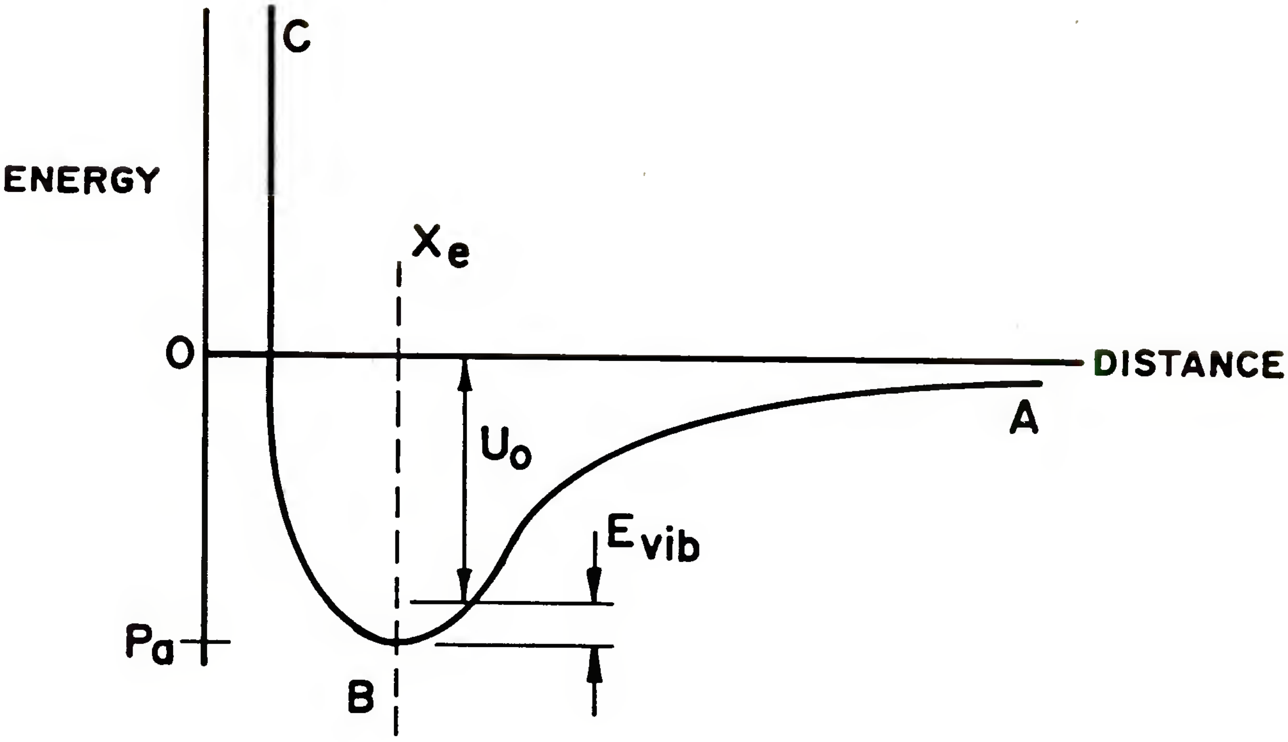

Figure B-2. Idealized Potential Energy of a Gas Molecule Approaching a Solid Surface.

would follow the path ABC in Figure B-2. Since at position B, the potential energy is at a minimum, the molecule will approach the surface to the distance x_e and remain there, in the process losing an amount of energy P_a. In the two-dimensional adsorbed phase, the molecule is free to vibrate and will have a vibrational energy, E_{vib}. Therefore, the total energy lost by the molecule is the adsorptive potential U_o, which is estimated as:

$$U_o = P_a - E_{vib} \tag{B-10}$$

The potential energy of the interaction of the adsorbate molecule with the adsorbent solid, P_a, is made up of three components: the potential due to dispersive forces, P_{disp}, or the Lennard-Jones[B-5] potential; the potential of interaction with the surface electrical field, P_{el}; and the potential of interaction of the gradient of the surface field with the quadrupole moment of the adsorbate molecule, P_{quad}. As shown in Figure B-2, E_{vib} is often small in comparison to P_a. Also, P_{el} and P_{quad} are often small in comparison to P_{disp}. Therefore, as a first approximation to the adsorptive potential, one may write:

$$U_o = P_{disp} + \text{H.O.T.} \tag{B-11}$$

where the higher order terms are:

$$\text{H.O.T.} = P_{el} + P_{quad} - E_{vib} \tag{B-12}$$

Using Eq. (B-11), it is possible to caculate the adsorptive potential for simple interaction systems. If the adsorbent is a perfect crystal of a pure element, i.e. pure aluminum, and the adsorbate is an atom, such as mercury, U_o can be estimated from calculating P_{disp} using the methods of Avgul et al.[B-6]

The potential function between two atoms approaching each other from infinity can be represented in terms of their internuclear separation x. There are four components of the potential function: that due to the interaction of the induced dipoles in the two atoms which is proportional to x^{-6}, that due to the interaction of the induced quadrupole of one atom with the dipole of another which is proportional to x^{-8}, the quadrupole-quadrupole interaction proportional to x^{-10}, and a repulsive component which is proportional to x^{-12}. Stated mathematically, the potential between two atoms, P, is:

$$P = C_1\, x^{-6} + C_2\, x^{-8} + C_3\, x^{-10} - C_R\, x^{-12} \qquad \text{(B-12)}$$

If one adsorbate atom is approaching a crystal containing i atoms, the total potential lost by the adsorbate atom, P_{disp}, is the sum of Eq. (B-12) over all i atoms, or:

$$P_{disp} = C_1 \sum_i x_i^{-6} + C_2 \sum_i x_i^{-8} + C_3 \sum_i x_i^{-10} - C_R \sum_i x_i^{-12} \qquad \text{(B-13)}$$

The constants C_1, C_2, and C_3 can be calculated from quantum mechanics and the properties of the atoms. The required properties are polarizability of the atom, α, and the diamagnetic susceptibility of the atom, χ.[B-5,B-6]

$$C_1 = \frac{6mc^2 \alpha_i \alpha_j}{R_i + R_j}$$

$$C_2 = \frac{45h^2}{32\pi^2 m}\alpha_i \alpha_j \left\{ \frac{1}{2\left(\frac{R_j}{R_i} + 1\right)} + \frac{1}{2\left(\frac{R_i}{R_j} + 1\right)} \right\}$$

$$C_3 = \frac{105h^4}{256\pi^4 m^3 c^2} \alpha_i \alpha_j \left\{ \frac{R_i}{3\frac{R_j}{R_i} + 1} + \frac{3}{4\left(\frac{1}{R_i} + \frac{1}{R_j}\right)} + \frac{R_j}{3\frac{R_i}{R_j}+1} \right\} \qquad \text{(B-14)}$$

where

$$R = \frac{\alpha}{\chi}$$

In Eqs. (B-14), the subscript i denotes the adsorbate and j denotes the adsorbent, m is the mass of an electron (9.11×10^{-28} g), c is the speed of light (2.998×10^{10} cm/s), and h is Planck's constant (6.63×10^{-27} erg-s).

There is no analytical expression that has been developed for the constant on the repulsive term, C_R. One is able to calculate this though, with the aid of Figure B-2. At the separation x_e, P is at a minimum; therefore $dP/dx)_{x=xe} = 0$. Using this, the constant C_R can be calulated by differentiating Eq. (B-13) and solving for C_R.

$$C_R = \frac{C_1\frac{d}{dx}(\sum x_i^{-6})_{x=xe} + C_2\frac{d}{dx}(\sum x_i^{-8})_{x=xe} + C_3\frac{d}{dx}(\sum x_i^{-10})_{x=xe}}{\frac{d}{dx}(\sum x_i^{-12})_{x=xe}} \qquad \text{(B-15)}$$

which can be solved by empirically fitting a function to the curve in Figure B-2 and analytically solving for C_R.[B-6]

Crowell[B-7] has shown that the lattice sums can be expressed analytically as:

$$\sum x_i^{-n} = \frac{2\pi\rho(-1)^n}{(n-2)d^{n-2}(n-3)!} \zeta^{n-3}(z) \qquad \text{(B-16)}$$

where ρ is the number of atoms per unit area of the crystal plane onto which the adsorbate atom is adsorbed, d is the interplanar spacing of the crystal plane, z is the ratio x/d, and ζ is the Riemann zeta function of z and n-3 which is calculated by:

$$\zeta^k(x) = (-1)^{k+1}k! \sum_{n=0}^{\infty} (x+n)^{-k-1} \qquad \text{(B-17)}$$

Using Eq. (B-17) and certain properties of the zeta function, Avgul et al[B-6] were able to solve for C_R. This enables Eq. (B-13) to be rewritten in closed form as:

$$P_{disp} = \frac{C_1\pi\rho}{12d^4}\left\{\zeta^3(z_e) + \frac{z_e}{10}\zeta^4(z_e)\right\} + \frac{2}{15}\frac{C_2\pi\rho}{x_e{}^6} + \frac{1}{20}\frac{C_3\pi\rho}{x_e{}^8} \qquad \text{(B-18)}$$

Avgul et al[B-6] have used Eq. (B-18) to predict the dispersive potential for several inert gases on graphite with remarkable precision. The same procedure is used here to estimate the adsorptive potential for the mercury on pure aluminum system.

In order to use Eq. (B-18), several properties of both the solid aluminum and the liquid mercury must be known. The atomic density, ρ, and interplanar spacing, d, are readily available from crystallography data.[B-8] The equilibrium spacing, x_e, and thus z_e, can be estimated by assuming that the atoms are hard incompressible spheres. The equilibrium internuclear spacing, x_e, then is simply the sum of the atomic radii of mercury and aluminum. This data is also available from the crystallography literature. This leaves the calculation of the constants C_1, C_2, and C_3.

Equations (B-14) are the calculations which must be made. Most of the data needed is available in basic physics textbooks,[B-9] but the quantities of polarizability of an atom, α, and diamagnetic susceptibility of an atom, χ, are elusive properties that are not often reported in the literature. There are means, though, by which reasonable estimates of these quantities can be calculated.

Polarizability is the extent to which any array of electrostatic charges are displaced in the presence of an electric field, $\bar{E}$, inducing a dipole moment, $\bar{\mu}$. Stated mathematically, α is defined as[B-10]

$$\bar{\mu} = \alpha \bar{E}$$

If the array of charges is not oriented in a symmetric pattern, the polarizability is a tensor, but if the array is a sphere, α is a scalar. For a conducting sphere of radius r, it can be shown that:

$$\alpha = r^3 \tag{B-19}$$

Since both aluminum and mercury are conducting metals, and their atoms already assumed to be hard spheres, Eq. (B-19) is used to calculate α for both aluminum and mercury.

The diamagnetic susceptibility of an atom is the ratio of the intensity of magnetization produced in the atom, to the intensity of the magnetic field to which the atom is subjected. Data for various substances has been reported in the physics literature. Ross and Olivier[B-3] have shown that the use of the experimentally measured diamagnetic susceptibilty data, which is measured using very large samples compared to atoms, does not result in calculated dispersion potentials which agree well with experiment. Thus, χ should be determined by some other method. One such method is discussed in reference

B-10 where χ was determined using "screening constants" for atoms calculated from the electronic structure of an atom.

The equation used to calculate χ is in reference B-10

$$\chi = \frac{-1.315 \times 10^{-30}}{a_o^2} \sum \bar{r}_i^2 \qquad \text{(B-20)}$$

where a_o is the Bohr radius (.5292 Å) and $\bar{r}_i^2$ is the square of the orbit of the i^{th} electron which can be represented by:

$$\bar{r}_i^2 = \left(\frac{n^*_i}{2(Z-S_i)}\right)^2 (2n^*_i + 1)\ (2n^*_i + 2)\ a_o^2 \qquad \text{(B-21)}$$

where n^*_i is the effective principal quantum number of an electron given in Table B-I, Z is the atomic number, and S_i is the screening constant for the groups of electrons organized according to Table B-II.

The screening constant S for any group of electrons is formed according to the following scheme:

TABLE B-I. EFFECTIVE QUANTUM NUMBERS USED TO CALCULATE DIAMAGNETIC SUSCEPTIBILITY OF AN ATOM

Principal Quantum Number	1	2	3	4	5	6
Effective Quantum Number n^*	1	2	3	3.7	4.0	4.2

TABLE B-II. GROUPING OF ELECTRONS USED TO FORM SCREENING CONSTANTS

Group	1	2	3	4	5	6	7	8	9	10	11
Shell	1s	2s 2p	3s 3p	3d	4s 4p	4d	4f	5s 5p	5d	5f	6s 6p

i) An amount of 0.35 is contributed from the total number of electrons in the group minus one, except for the 1s group where 0.3 is used. For example if group 1 in Table B-II has two electrons, then the contribution of this group to the screening constant:

$$S_1 = (2 \text{ electrons} - 1) \times 0.3 = 0.3$$

ii) If the shell is an s or a p shell, an amount of 0.85 is contributed from each electron with a principal quantum number which is less by one, and an amount of 1.0 from each electron further in. For example, if groups 1, 2, and 3 in Table B-II are all full, then there are eight electrons in group 3, eight electrons in group 2, and two electrons in group 1. The screening constant for this group is formed by:

$$S_3 = \underbrace{(8 \text{ electrons} - 1) \times 0.35}_{\text{contribution from } 3s + 3p} + \underbrace{(8 \text{ electrons}) \times 0.85}_{\text{from } 2s + 2p} + \underbrace{(2 \text{ electrons}) \times 1.0}_{\text{from } 1s} = 11.25$$

iii) If the shell is a d or f shell, then each electron in groups further in contributes an amount 1.0 to the screening constant. For example, if groups 1, 2, 3, and 4 are all full, the screening constant is:

$$S_4 = \underbrace{(10 \text{ electrons} - 1) \times 0.35}_{3d} + \underbrace{(18 \text{ electrons} - 1) \times 1.0}_{1s, 2s, 2p, 3s, 3p} = 21.15$$

For aluminum, Z=13, the electronic arrangement is $1s^2$, $2s^2$, $2p^6$, $3s^2$, $3p^1$. There are three sceening constants to calculate, one each from groups 1, 2, and 3:

$$S_1 = (2 - 1) \times 0.3 = 0.3$$

$$S_2 = (8 - 1) \times 0.35 + (2) \times 0.85 = 4.15$$

$$S_3 = (3 - 1) \times 0.35 + (8) \times 0.85 + (2) \times 1.0 = 9.5$$

For mercury, Z=80, the electronic configuration is $1s^2$, $2s^2$, $2p^6$, $3s^1$, $3p^6$, $3d^{10}$, $4s^2$, $4p^6$, $4d^{11}$, $4f^{14}$, $5s^2$, $5p^6$, $5d^{10}$, $6s^2$. There are ten screening constants to be formed, one each from groups 1 thru 9, and one from group 11. These constants are:

$$S_1 = (2 - 1) \times 0.3 = 0.3$$

$$S_2 = (8 - 1) \times 0.35 + (2) \times 0.85 = 4.15$$

$$S_3 = (8 - 1) \times 0.35 + (8) \times 0.85 + (2) \times 1.0 = 11.25$$

$$S_4 = (10 - 1) \times 0.35 + (8) \times 0.85 + (2) \times 1.0 = 21.15$$

$$S_5 = (8 - 1) \times 0.35 + (18) \times 0.85 + (10) \times 1.0 = 27.75$$

$$S_6 = (10 - 1) \times 0.35 + (36) \times 1.0 = 39.15$$

$$S_7 = (14 - 1) \times 0.35 + (46) \times 1.0 = 50.55$$

$$S_8 = (8 - 1) \times 0.35 + (30) \times 0.85 + (28) \times 1.0 = 55.95$$

$$S_9 = (10 - 1) \times 0.35 + (68) \times 1.0 = 71.15$$

$$S_{11} = (2 - 1) \times 0.35 + (18) \times 0.85 + (60) \times 1.0 = 75.65$$

The screening constants for aluminum and mercury, calculated above, can now be used in conjunction with Eqs. (B-20) and (B-21) to calculate the diamagnetic susceptibility of these two elements. These calculations are summarized for aluminum in Table B-III, and for mercury in Table B-IV.

TABLE B-III. CALCULATION OF DIAMAGNETIC SUSCEPTIBILITY FOR ALUMINUM (Z = 13).

Group	n^*	S	Z-S	r^2/a_o^2	XAl
1	1	0.3	12.7	0.0186	-1.41 x 10^{-29} (cm^3)
2	2	4.15	8.85	0.3830	
3	3	9.5	3.5	10.286	

TABLE B-IV. CALCULATION OF DIAMAGNETIC SUSCEPTIBILITY FOR MERCURY (Z=80).

Group	n^*	S	Z-S	r^2/a_o^2	XHg
1	1	0.3	79.7	4.7 x 10^{-4}	-3.79 x 10^{-29} (cm^3)
2	2	4.15	75.85	5.2 x 10^{-3}	
3	3	11.25	68.75	2.7 x 10^{-2}	
4	3	21.15	58.85	3.6 x 10^{-2}	
5	3.7	27.75	52.25	.10	
6	3.7	39.15	40.85	.161	
7	3.7	50.55	29.45	.312	
8	4	55.95	24.05	.721	
9	4	71.15	8.85	4.60	
11	4.2	75.65	4.35	22.8	

Now we have all the information necessary to estimate the adsorptive potential. It is assumed that adsorption was occurring on a $\{100\}$ plane. For aluminum, $\{100\}$ planes have a planar density, ρ, of 1.22×10^{15} atoms/cm^2, and have an interplanar spacing, d, of 4.05×10^{-8} cm. All of the parameters used in the calculation of U_o are given in Table B-V. The negative sign means that the adsorbent atom loses energy upon adsorption, which is shown schematically in Figure B-2. By convention, an energy loss is positive. Therefore, the estimated adsorptive potential is + 3.49 kcal/mole.

TABLE B-V. SUMMARY OF THE CALCULATION OF THE ESTIMATED ADSORPTIVE POTENTIAL, U_o, FOR MERCURY ON ALUMINUM.

	Mercury	Adsorbed Phase	Aluminum
Atomic Radius (cm)	1.503×10^{-8}		1.431×10^{-8}
Polarizability, α, (cm^3)	3.4×10^{-24}		2.93×10^{-24}
Diamagnetic Susceptibility. χ, (cm^3)	-3.78×10^{-29}		-1.41×10^{-29}
R	-8.98×10^{4}		-2.08×10^{5}
C_1 (kcal cm^6 mole^{-1})		-2.35×10^{-45}	
C_2 (kcal cm^8 mole^{-1})		$+4.84 \times 10^{-61}$	
C_3 (kcal cm^{10} mole^{-1})		-2.51×10^{-76}	
x_e (cm)		2.934×10^{-8}	
Z_e		.725	
ζ^3 (Z_e)		22.608	
ζ^4 (Z_e)		-121.93	
d (cm)		4.05×10^{-8}	
ρ (atoms/cm^2)		1.22×10^{15}	

Estimated Adsorptive Potential $U_o = -3.49$ kcal/mole

Based on the arguments that led to Eq. (B-9), a plot of the rate of adsorption of mercury on aluminum versus inverse temperature would give a positive slope of about 3.5 kcal/mole. Similarly, if a process is rate limited by surface adsorption, then a plot of the rate of the process versus inverse temperature should also result in a positive slope of about 3.5 kcal/mole. This is very nearly what was measured in the crack growth experiments performed at different temperatures described in this report. Therefore, it is quite likely that the growth of mercury embrittled cracks in aluminum is rate limited by the rate of adsorption of mercury on the surface of the solid aluminum.

APPENDIX REFERENCES

B-1. Stoloff, N. S., "Solid and Liquid Metal Embrittlement," Presented at the NATO Advanced Study Institute on Atomistics of Fracture, Corsica, May, 1981, to be published.

B-2. Rice, J. R., J. Mech. Phys. Solids, Vol. 26, 1978, p. 61.

B-3. Ross, S. and Olivier, J. P., On Physical Adsorption, Wiley, NY, 1964.

B-4. Langmuir, I., J. Amer. Chem. Soc., Vol. 39, 1917, p. 1848.

B-5. Lennard-Jones, J. E. and Dent, B. M., Trans. of the Farady Soc., Vol. 24, 1928, p. 92.

B-6. Avgul, N. N., Kiselev, A. V., Lygina, I. A. and Poschus I., Bull. Acad. Sci. USSR, Div. Chem. Sci., 1959, p. 1155.

B-7. Crowell, A. D., J. Chem. Phys., Vol. 26, 1957, p. 1407.

B-8. Cullity, B. D., Elements of X-Ray Diffraction, Addison-Wesley, Reading, MA, 1967.

B-9. Shortley, George and Williams, Dudly, Elements of Physics, Prentice - Hall, NY, 1955.

B-10. Hirshfelder, Joseph O., Curtis, Charles F., and Bird, R. Byron, Molecular Theory of Gases and Liquids, Wiley, NY, 1954.

TECHNICAL REPORT INTERNAL DISTRIBUTION LIST

	NO. OF COPIES
CHIEF, DEVELOPMENT ENGINEERING BRANCH	
ATTN: DRDAR-LCB-D	1
-DP	1
-DR	1
-DS (SYSTEMS)	1
-DS (ICAS GROUP)	1
-DC	1
CHIEF, ENGINEERING SUPPORT BRANCH	
ATTN: DRDAR-LCB-S	1
-SE	1
CHIEF, RESEARCH BRANCH	
ATTN: DRDAR-LCB-R	2
-R (ELLEN FOGARTY)	1
-RA	1
-RM	1
-RP	1
-RT	1
TECHNICAL LIBRARY	5
ATTN: DRDAR-LCB-TL	
TECHNICAL PUBLICATIONS & EDITING UNIT	2
ATTN: DRDAR-LCB-TL	
DIRECTOR, OPERATIONS DIRECTORATE	1
DIRECTOR, PROCUREMENT DIRECTORATE	1
DIRECTOR, PRODUCT ASSURANCE DIRECTORATE	1

NOTE: PLEASE NOTIFY DIRECTOR, BENET WEAPONS LABORATORY, ATTN: DRDAR-LCB-TL, OF ANY REQUIRED CHANGES.

TECHNICAL REPORT EXTERNAL DISTRIBUTION LIST

	NO. OF COPIES
ASST SEC OF THE ARMY RESEARCH & DEVELOPMENT ATTN: DEP FOR SCI & TECH THE PENTAGON WASHINGTON, D.C. 20315	1
COMMANDER DEFENSE TECHNICAL INFO CENTER ATTN: DTIC-DDA CAMERON STATION ALEXANDRIA, VA 22314	12
COMMANDER US ARMY MAT DEV & READ COMD ATTN: DRCDE-SG 5001 EISENHOWER AVE ALEXANDRIA, VA 22333	1
COMMANDER US ARMY ARRADCOM ATTN: DRDAR-LC	1
DRDAR-LCA (PLASTICS TECH EVAL CEN)	1
DRDAR-LCE	1
DRDAR-LCM (BLDG 321)	1
DRDAR-LCS	1
DRDAR-LCU	1
DRDAR-LCW	1
DRDAR-TSS (STINFO)	2
DOVER, NJ 07801	
DIRECTOR US ARMY BALLISTIC RESEARCH LABORATORY ATTN: DRDAR-TSB-S (STINFO) ABERDEEN PROVING GROUND, MD 21005	1
COMMANDER US ARMY ARRCOM ATTN: DRSAR-LEP-L ROCK ISLAND ARSENAL ROCK ISLAND, IL 61299	1

	NO. OF COPIES
COMMANDER ROCK ISLAND ARSENAL ATTN: SARRI-ENM (MAT SCI DIV) ROCK ISLAND, IL 61299	1
DIRECTOR US ARMY INDUSTRIAL BASE ENG ACT ATTN: DRXIB-M ROCK ISLAND, IL 61299	1
COMMANDER US ARMY TANK-AUTMV R&D COMD ATTN: TECH LIB - DRSTA-TSL WARREN, MI 48090	1
COMMANDER US ARMY TANK-AUTMV COMD ATTN: DRSTA-RC WARREN, MI 48090	1
COMMANDER US MILITARY ACADEMY ATTN: CHM, MECH ENGR DEPT WEST POINT, NY 10996	1
US ARMY MISSILE COMD REDSTONE SCIENTIFIC INFO CEN ATTN: DOCUMENTS SECT, BLDG 4484 REDSTONE ARSENAL, AL 35898	2
COMMANDER US ARMY FGN SCIENCE & TECH CEN ATTN: DRXST-SD 220 7TH STREET, N.E. CHARLOTTESVILLE, VA 22901	1
COMMANDER US ARMY MATERIALS & MECHANICS RESEARCH CENTER ATTN: TECH LIB - DRXMR-PL WATERTOWN, MA 02172	2

NOTE: PLEASE NOTIFY COMMANDER, ARRADCOM, ATTN: BENET WEAPONS LABORATORY, DRDAR-LCB-TL, WATERVLIET ARSENAL, WATERVLIET, NY 12189, OF ANY REQUIRED CHANGES.

TECHNICAL REPORT EXTERNAL DISTRIBUTION LIST (CONT'D)

	NO. OF COPIES
COMMANDER US ARMY RESEARCH OFFICE ATTN: CHIEF, IPO P.O. BOX 12211 RESEARCH TRIANGLE PARK, NC 27709	1
COMMANDER US ARMY HARRY DIAMOND LAB ATTN: TECH LIB 2800 POWDER MILL ROAD ADELPHIA, MD 20783	1
COMMANDER NAVAL SURFACE WEAPONS CEN ATTN: TECHNICAL LIBRARY CODE X212 DAHLGREN, VA 22448	1

	NO. OF COPIES
DIRECTOR US NAVAL RESEARCH LAB ATTN: DIR, MECH DIV	1
CODE 26-27 (DOC LIB) WASHINGTON, D.C. 20375	1
METALS & CERAMICS INFO CEN BATTELLE COLUMBUS LAB 505 KING AVE COLUMBUS, OH 43201	1
MATERIEL SYSTEMS ANALYSIS ACTV ATTN: DRXSY-MP ABERDEEN PROVING GROUND MARYLAND 21005	1

NOTE: PLEASE NOTIFY COMMANDER, ARRADCOM, ATTN: BENET WEAPONS LABORATORY, DRDAR-LCB-TL, WATERVLIET ARSENAL, WATERVLIET, NY 12189, OF ANY REQUIRED CHANGES.